UNIVERSITY OF CALIFORNIA,
IRVINE

Investigating the Structural and Metal Binding Properties of an Ancestral Eye Lens Crystallin

DISSERTATION

submitted in partial satisfaction of the requirements
for the degree of

DOCTOR OF PHILOSOPHY

in Chemistry

by

Natalia Kozlyuk

Dissertation Committee:
Associate Professor Rachel W. Martin, Chair
Associate Professor Andrej Lupták
Professor James Nowick

2017

DEDICATION

I would like to dedicate this thesis dissertation work to my family who have consistently been supporting me throughout my scientific journey.

TABLE OF CONTENTS

Page

LIST OF FIGURES **vi**

LIST OF TABLES **xi**

ACKNOWLEDGMENTS **xiii**

CURRICULUM VITAE **xv**

ABSTRACT OF THE DISSERTATION **xviii**

1 Calcium binding dramatically stabilizes an ancestral crystallin fold in tunicate $\beta\gamma$-crystallin. **1**

1.1 Background 1

1.2 Materials and Methods 4

1.2.1 Gene construction, protein expression and purification 4

1.2.2 Circular dichroism spectroscopy 5

1.2.3 Fluorescence spectroscopy 5

1.2.4 Isothermal titration calorimetry 6

1.3 Results 7

1.3.1 Unlike human γS-crystallin, *Ci*-$\beta\gamma$ binds Ca^{2+} with strong affinity. . . . 7

1.3.2 Ca^{2+} binding does not change the secondary structure of *Ci*-$\beta\gamma$-crystallin 9

1.3.3 The resistance of *Ci*-$\beta\gamma$-crystallin to both thermal and chemical denaturation dramatically increases upon binding Ca^{2+} 9

1.4 Discussion 13

2 Effects of divalent cations on the structure of tunicate $\beta\gamma$-crystallin. **18**

2.1 Background 18

2.2 Materials and methods 20

2.2.1 Thermal denaturation 20

2.2.2 Dynamic light scattering 21

2.2.3 Isothermal titration calorimetry 21

2.2.4 NMR experiments 21

2.3 Results and Discussion 22

3 Solution-state NMR structure determination of tunicate $\beta\gamma$-crystallin in the apo and holo form. 32
3.1 Background . . . 32
3.2 Materials and Methods . . . 34
3.2.1 Sample preparation . . . 34
3.2.2 NMR experiments . . . 35
3.2.3 Data processing . . . 35
3.3 Results and Discussion . . . 35
3.4 Backbone Resonance Assignments . . . 38
3.4.1 HNCO . . . 38
3.4.2 HN(CO)CA . . . 41
3.4.3 HNCA . . . 44
3.4.4 HN(CA)CO . . . 47
3.4.5 CBCA(CO)NH . . . 50
3.4.6 HNCACB . . . 53
3.5 Side-chain Resonance Assignments . . . 56
3.5.1 CC(CO)NH . . . 56
3.5.2 H(CCO)NH . . . 58
3.5.3 HCCH-COSY . . . 60
3.5.4 HCCH-TOCSY . . . 63
3.5.5 ^{15}N-TOCSY-HSQC . . . 67
3.6 Distance Restraints . . . 70
3.6.1 NOESY-^{15}N-HSQC . . . 70
3.6.2 ^{13}C-NOESY HSQC . . . 72
3.6.3 ^{15}N-HSQC IPAP . . . 74
3.7 Hydrogen Bonds . . . 76

4 Low temperature alignment media for measuring residual dipolar couplings during biomolecular NMR structure determination. 81
4.1 Background . . . 81
4.2 Materials and Methods . . . 84
4.2.1 Sample preparation . . . 84
4.2.2 NMR experiments . . . 85
4.3 Results and Discussion . . . 86
4.4 Conclusions and Future Directions . . . 95

5 *In Situ* NMR Measurement of Macromolecule-Bound Metal Ion Concentrations. 97
5.1 Background . . . 97
5.2 Materials and Methods . . . 99
5.2.1 Sample preparation . . . 99
5.2.2 NMR experiments . . . 100
5.2.3 Construction of titration curves and error analysis . . . 101
5.3 Results and Discussion . . . 102

Bibliography **110**

A 1: Supplementary material for calcium binding dramatically stabilizes an ancestral crystallin fold in tunicate $\beta\gamma$-crystallin. **119**
A.1 ITC data analysis for sequential binding 126

B 2:Supplementary material for effects of divalent cations on the structure of tunicate $\beta\gamma$-crystallin. **129**

C 3:Supplementary material for solution-state NMR structure determination of tunicate $\beta\gamma$-crystallin in the apo and holo form. **136**

D 4:Supplementary material for low temperature alignment media for measuring residual dipolar couplings during biomolecular NMR structure determination. **140**
D.1 Expression and purification of Droserasin 1, plant specific insert 145

E 5:Supplementary material for *In Situ* NMR Measurement of Macromolecule-Bound Metal Ion Concentrations. **147**

LIST OF FIGURES

Page

1.1 Thermogram demonstrating the binding of Ca^{2+} to tunicate $\beta\gamma$-crystallin. Ca^{2+} (5 mM) was titrated into 386 μM protein sample in 10 mM Tris-HCl (pH 7.1) and the curve was best fit to a sequential binding model. 8

1.2 (a) The CD spectra of both the apo (blue dashed line) and holo (red solid line) forms of tunicate $\beta\gamma$-crystallin display strong minima at 218 nm, indicating primarily β-sheet secondary structure that does not significantly change upon the addition of Ca^{2+}. (b) Similarly, the intrinsic tryptophan fluorescence signal displays only a slight increase in intensity as a result of Ca^{2+} binding. The wavelength of the emission maximum does not shift, indicating that the environment of the Trp residues remains mostly unchanged. 10

1.3 Thermal denaturation curves showing the thermal stability of the protein measured over a range of 17-100 °C. The holo form of the protein shows an increase in thermal stability compared with the apo form. The T_m increases from 45.8 °C to 94.2 °C upon addition of Ca^{2+}. Open circles indicate reversibility of the experiment. 11

1.4 The *Ci*-$\beta\gamma$-crystallin is resistant to chemical denaturation with (a) GndHCl and (b) urea upon addition of Ca^{2+}. Open circles indicate the reversibility of the experiment. Denaturation of the apo form is fully reversible in both denaturing conditions, while the holo form refolds to the intermediate state in the GndHCl denaturing conditions. 12

1.5 (Top) Sequence alignment of $\beta\gamma$-crystalllins from *C. intestinalis*, *C. beijerinckii*, *M. acetivorans*, *G. cydonium*, *B. taurus*, and *H. sapiens*. Residues highlighted in green are strictly conserved, while residues highlighted in cyan are functionally conserved. Boxes enclose residues involved in calcium binding as determined by polar contacts made in the structure. Arrows indicate the calcium binding residues of sites 1 and 2. (Bottom) View of calcium binding site 2 in *C. intestinalis* $\beta\gamma$, *M. acetivorans* $\beta\gamma$, *B. taurus* γ-crystallin and human γS-crystallin. 15

2.1 Thermal denaturation of *Ci*-$\beta\gamma$ crystallin in the presence of 1 mM EDTA, $MgCl_2$, $NiCl_2$, $ZnCl_2$, $SrCl_2$, $CoCl_2$, $CaCl_2$ and $MnCl_2$. The presence of all divalent cations tested thermally stabilized the protein relative to the apo form; however the degree of stabilization varied from an increase in T_m of 7 °C (Zn^{2+}) to 48 °C (Ca^{2+}). 23

2.2 DLS measurements of tunicate crystallin in the presence of 1 mM EDTA, $MgCl_2$, $NiCl_2$, $ZnCl_2$, $SrCl_2$, $CoCl_2$, $CaCl_2$ and $MnCl_2$. Data were plotted up to the temperature when the majority of the protein crashed out and caused a reduction in signal intensity. The presence of Zn^{2+} and Ni^{2+} caused the protein to form aggregates at lower temperatures but the presence of Ca^{2+} and Sr^{2+} did not cause protein aggregation until 80-90 °C. 24
2.3 ITC binding isotherm of tunicate crystallin titrated with 10 mM $SrCl_2$ showed a similar binding mechanism to that with $CaCl_2$ (chapter 1). 27
2.4 ITC binding isotherm of tunicate crystallin titrated with 10 mM $SrCl_2$ was fit to a sequential binding model with Mathematica similar to chapter 1. Molar ratio was cut off at 2 to obtain a better fit of the data. 28
2.5 Chemical shift perturbation for tunicate $\beta\gamma$-crystallin with increasing Sr^{2+} (a), Mg^{2+} (c), Ni^{2+} (e), and Zn^{2+} (g) calculated from ^{15}N HSQC experiments. The residues that shift the most fall above the 0.2 cut off and they are represented in the X-ray crystal structure (PDBID 2BV2) in purple, residues that minimally shift are between 0.06 and 0.2 and are represented in teal, and residues that do not shift or were unassigned are represented in grey (b, d, f, g). 30

3.1 Residues involved in the calcium binding sites of the tunicate $\beta\gamma$-crystallin, observed in the X-ray crystal structure PDBID 2BV2 [3]. 36
3.2 a. ^{15}N-^{1}H HSQC spectra of the tunicate $\beta\gamma$-crystallin in the absence (green) and presence (magenta) of 10 mM $CaCl_2$. Residues that have the same chemical shift under both conditions are labeled in black. b. Average chemical shift perturbation plot as a function of residue number, with thresholds for large (> 0.2 ppm) and moderate (0.06-0.2 ppm). Residues for which the shift is < 0.06 ppm upon addition of $CaCl_2$ are classified as unperturbed. c. The same CSP data represented on the X-ray crystal structure. The backbone corresponding to amide NHs for which the chemical shift perturbation is large are shown in purple, while amides that are slightly perturbed are in cyan and those of unperturbed residues are shown in gray. The two calcium ions are represented in red, while the side chains of the Ca^{2+}-binding residues are highlighted in green. 37
3.3 The transfer of magnetization in HNCO [58]. 38
3.4 Four zoomed in planes of HNCO spectra showing sequential $(CO)_{i-1}$ residue assignments of tunicate crystallin in the presence of Ca^{2+} (a) or EDTA (b). 39
3.5 The transfer of magnetization in HN(CO)CA [58]. 41
3.6 Four zoomed in planes of HN(CO)CA spectra showing sequential $(Ca)_{i-1}$ residue assignments of tunicate crystallin in the presence of Ca^{2+} (a) or EDTA (b). 42
3.7 The transfer of magnetization in HNCA [58]. 44
3.8 Four zoomed in planes of HNCA spectra showing sequential $(Ca)_i$ and $(Ca)_{i-1}$ residue assignments of tunicate crystallin in the presence of Ca^{2+} (a) or EDTA (b). 45
3.9 The transfer of magnetization in HN(CA)CO [58]. 47

3.10 Four zoomed in planes of HN(CA)CO spectra showing sequential $(CO)_i$ and $(CO)_{i-1}$ residue assignments of tunicate crystallin in the presence of Ca^{2+} (a) or EDTA (b). 48
3.11 The transfer of magnetization in CBCA(CO)NH [58]. 50
3.12 Four zoomed in planes of CBCA(CO)NH spectra showing sequential $(Ca)_{i-1}$ and $(Cb)_{i-1}$ residue assignments of tunicate crystallin in the presence of Ca^{2+} (a) or EDTA (b). 51
3.13 The transfer of magnetization in HNCACB [58]. 53
3.14 Four zoomed in planes of HNCACB spectra showing sequential $(Ca)_i$, $(Ca)_{i-1}$, $(Cb)_i$ and $(Cb)_{i-1}$ residue assignments of tunicate crystallin in the presence of Ca^{2+} (a) or EDTA (b). 54
3.15 The transfer of magnetization in CC(CO)NH [58]. 56
3.16 Four zoomed in planes of CC(CO)NH spectra showing carbon side chains of sequential i-1 residue assignments of tunicate crystallin in the presence of Ca^{2+} (a) or EDTA (b). 57
3.17 The transfer of magnetization in H(CCO)NH [58]. 59
3.18 Four zoomed in planes of H(CCO)NH spectra showing proton side chains of sequential i-1 residue assignments of tunicate crystallin in the presence of Ca^{2+}. 59
3.19 The transfer of magnetization in HCCH-COSY [58]. 61
3.20 A ^{13}C plane of HCCH-COSY spectrum showing several proton and carbon side chains of the same residue in tunicate crystallin in the presence (a) and absence (b) of Ca^{2+}. 62
3.21 The transfer of magnetization in HCCH-TOCSY [58]. 64
3.22 A ^{13}C plane of HCCH-TOCSY spectrum showing several proton and carbon side chains of the same spin system in tunicate crystallin in the presence (a) and absence (b) of Ca^{2+}. 65
3.23 The transfer of magnetization in ^{15}N-TOCSY-HSQC [58]. 67
3.24 Four zoomed in planes of ^{15}N-TOCSY-HSQC spectra showing proton side chains of sequential i residue assignments of tunicate crystallin in the presence (a) and absence (b) of Ca^{2+}. 68
3.25 The transfer of magnetization in NOESY-^{15}N-HSQC [58]. 70
3.26 A ^{15}N plane of ^{15}N-TOCSY-HSQC spectrum showing assignments of protons and nitrogens connected through space of tunicate crystallin in the presence of Ca^{2+}. 71
3.27 The transfer of magnetization in ^{13}C-NOESY HSQC [58]. 72
3.28 A ^{13}C plane of ^{13}C-NOESY HSQC spectrum showing assignments of protons and carbons connected through space of tunicate crystallin in the presence of Ca^{2+}. 73
3.29 ^{15}N-HSQC IPAP spectra in the presence (a) and absence (b) of Ca^{2+} of tunicate crystallin. Each backbone peak is split, unlike in a regular ^{15}N-HSQC. This splitting corresponds to a N-H J-coupling of 91-94 Hz in the isotropic samples. 75
3.30 Overlay of a series of temperature ^{15}N-HSQC spectra of tunicate crystallin in the holo (a) and apo (b) form. The protein remains fully folded even at 75 °C in the holo form yet denatures at 50 °C in the apo form. 78

3.31 Amide proton temperature coefficient plots of six residues taken from the temperature ^{15}N-HSQC spectrum of tunicate crystallin in the presence of EDTA. Plots shown in blue have slopes < -4.6 ppb/K and these residues which are hydrogen bonding intramolecularly. Plots shown in red have slopes > -4.6 ppb/K and these residues which are hydrogen bonding with the solvent. 79
3.32 Hydrogen bonds determined from the amide proton temperature coefficients are represented on the crystal structure (PDB: 2BV2) [3]. Residues which are hydrogen bonding with the solvent are shown in red and residues which are hydrogen bonding intramolecularly are shown in blue. Both the apo and the holo form of the tunicate crystallin shows similar hydrogen bonding patterns. The main difference between the two structures is that the loop-like region which typically binds to the Ca^{2+} ions is hydrogen bonding more with the solvent in the EDTA structure. 80

4.1 Isotropic (a) to chiral nematic (b) phase transition of DMPC/DHPC/CS. . . 87
4.3 ^{2}H NMR spectra of DLPC/DHPC/CS in the presence of 10 mM Ca^{2+} and in the absence (a) and presence (b) of tunicate crystallin. Alignment of the bicelles occurs at 8 °C in both samples. 89
4.2 ^{2}H NMR spectra of DLPC/DHPC/CS in the presence of 10 mM Mg^{2+} and in the absence (a) and presence (b) of DD. There is a liquid crystallin phase transition from the isotropic to anisotropic phase at 6 °C. Addition of DD decreased the bicelle alignment slightly as can be seen by the decrease in the deuterium splittings. 90
4.4 Small regions of DQF-COSY spectra comparing DD cytidine H5/H6 couplings in the absence (a) and presence (b, c) of DLPC/DHPC/CS at 5 °C (magenta) and -5 °C (green). Solid contours represent positive intensities and dashed contours represent negative intensities. Couplings were measured using only the F2 dimension from the top of a positive contour to the top of a negative contour. 91
4.5 Small region of the ^{15}N-HSQC IPAP of tunicate crystallin with 10 mM Ca^{2+} taken at 8 °C in the absence (a) and presence (b) of 15 % w/v DLPC/DHPC and 13.4 % CS with respect to moles of DLPC. There are five residues that are shown in the spectra which are aligned in the presence of the bicelles as indicated by the change in the N-H couplings. This change in the couplings is used to calculate residual dipolar couplings of each residue. 93

5.1 Titration curves of the α-phosphate ^{31}P chemical shift as a function of increasing (a) $[Mg^{2+}_{Free}]$ and (b) $[Ca^{2+}_{Free}]$ at different pH values and temperatures relative to 85 % phosphoric acid (external reference). Blue represents titrations at 8 °C and red represents titrations at 25 °C. At 8 °C, the pH increases by about 0.2 units from the pH values given. 104

5.2 (a) ^{31}P spectra of dCDP in the presence of $\beta\gamma$-crystallin and 7 mM Ca^{2+} showing differences in the α- phosphate chemical shifts at two different temperatures and neutral pH. The differences in the chemical shifts correspond to differences in the free divalent ion concentration in solution as interpolated using the method shown in (b) for 8 ° C: e.g. 5.7 ± 1.0 mM of free plus bound Ca^{2+} to dCDP out of 7 mM added in the protein sample (shown by the arrow) implying that 1.1 ± 1.0 mM was bound by the protein. Using this method, the DNA bound 2.3 ± 0.7 mM Mg^{2+}, bicelles bound 7.7 ± 0.3 mM Mg^{2+}, and the bicelles bound 6.0 ± 0.7 mM Ca^{2+} at 8 ° C. 106

LIST OF TABLES

Page

1.1 Thermodynamic parameters for binding of Ca^{2+} to *Ci*-$\beta\gamma$-crystallin. 8
1.2 Thermodynamic parameters for guanidinium hydrochloride denaturation. . . 13

2.1 Thermodynamic parameters for binding of Sr^{2+} to *Ci*-$\beta\gamma$-crystallin. 28

3.1 HNCO NMR parameters of tunicate crystallin with 10 mM Ca^{2+} 40
3.2 HNCO NMR parameters of tunicate crystallin with 10 mM EDTA 40
3.3 HN(CO)CA NMR parameters of tunicate crystallin with 10 mM Ca^{2+} 43
3.4 HN(CO)CA NMR parameters of tunicate crystallin with 10 mM EDTA . . . 43
3.5 HNCA NMR parameters of tunicate crystallin with 10 mM Ca^{2+} 46
3.6 HNCA NMR parameters of tunicate crystallin with 10 mM EDTA 46
3.7 HN(CA)CO NMR parameters of tunicate crystallin with 10 mM Ca^{2+} 49
3.8 HN(CA)CO NMR parameters of tunicate crystallin with 10 mM EDTA . . . 49
3.9 CBCA(CO)NH NMR parameters of tunicate crystallin with 10 mM Ca^{2+} . . 52
3.10 CBCA(CO)NH NMR parameters of tunicate crystallin with 10 mM EDTA . 52
3.11 HNCACB NMR parameters of tunicate crystallin with 10 mM Ca^{2+} 55
3.12 HNCACB NMR parameters of tunicate crystallin with 10 mM EDTA 55
3.13 CC(CO)NH NMR parameters of tunicate crystallin with 10 mM Ca^{2+} 58
3.14 CC(CO)NH NMR parameters of tunicate crystallin with 10 mM EDTA . . . 58
3.15 H(CCO)NH NMR parameters of tunicate crystallin with 10 mM Ca^{2+} 60
3.16 HCCH-COSY NMR parameters of tunicate crystallin with 10 mM Ca^{2+} . . . 63
3.17 HCCH-COSY NMR parameters of tunicate crystallin with 10 mM EDTA . . 63
3.18 HCCH-TOCSY NMR parameters of tunicate crystallin with 10 mM Ca^{2+} . . 66
3.19 HCCH-TOCSY NMR parameters of tunicate crystallin with 10 mM EDTA . 66
3.20 ^{15}N-TOCSY-HSQC NMR parameters of tunicate crystallin with 10 mM Ca^{2+} 69
3.21 ^{15}N-TOCSY-HSQC NMR parameters of tunicate crystallin with 10 mM EDTA 69
3.22 NOESY-^{15}N-HSQC NMR parameters of tunicate crystallin with 10 mM Ca^{2+} 72
3.23 ^{13}C-NOESY HSQC NMR parameters of tunicate crystallin with 10 mM Ca^{2+} 74
3.24 ^{15}N-HSQC IPAP NMR parameters of tunicate crystallin with 10 mM Ca^{2+} . 76
3.25 ^{15}N-HSQC IPAP NMR parameters of tunicate crystallin with 10 mM EDTA 76

4.1 H5/H6 cytidine splittings in Hertz in the presence and absence of DLPC/DHPC/CS and all in the presence of 10 mM Mg^{2+} at 5 °C and - 5 °C. X represents couplings which were not resolved or were absent from the spectrum as a result of negative dipolar couplings. 92

4.2 Residual dipolar couplings of 37 residues of the tunicate $\beta\gamma$-crystallin in the presence of 10 mM Ca^{2+} at 8 °C. 94

5.1 Interaction of the dCDP α-phosphate with $[Mg^{2+}_{Free}]$. 105
5.2 Macromolecule- bound $[Mg^{2+}]$ and $[Ca^{2+}]$ at 25 °C and 8 °C calculated from the ^{31}P chemical shifts of dCDP. 108

ACKNOWLEDGMENTS

I would like to thank numerous individuals for their support and helpful insight over the past five years en route to developing myself as a better scientist. First and foremost, I would like to acknowledge my Ph.D. advisor Professor Rachel Martin who has developed me into an independent, collaborative and self-motivated scientist by allowing me to pursue research projects that I was both curious about and thought were important. Rachel gave our lab the freedom to work on several projects simultaneously and encouraged us to attend scientific meetings and workshops that would enhance our career paths. She placed an enormous amount on publishing our work whenever we made significant progress which undoubtly helped me focus better and prioritize my work. I will forever be grateful for her ability to care for each of her students in helping them move forward with their careers.

I am grateful for my dissertation committee members, Professor Andrej Lupták and Professor James Nowick. They have both continued to support me throughout my graduate studies and have given me great advice in both my research projects and career paths. Andrej has been involved on several of my structural NMR methods projects and has remained both my research collaborator and my go to person whenever I needed advise about future career plans. I cannot thank him enough for always listening to my frantic worries about which step I should take next after graduation. He was also the chair of my advancement committee and guided me tremendously on my original proposal project. James was also an important part of my graduate studies especially during the first two years by advising me through classes and through my original proposal for the advancement exam. Although I have not interacted with James as much over the past couple of years, he has been a huge influence in my studies and has always been open to hearing about my current and future work.

In addition, I want to thank my B.S. advisor Dr. Henry Acquaye at the University of Redlands who has remained a significant part of my life even after graduation. It was because of Dr. Acquaye that I got introduced to conducting my own research projects and starting to become some-what independent as an undergraduate researcher. He mentored me through my research projects and encouraged me to attend conferences to present my work. After graduating from the University of Redlands, a couple of his research students continued to pursue my research project further to the point where it was enough data to be published in a scientific journal. He became not only my research advisor but also my academic one and guided me through the graduate school application process. He also quickly became my mentor in life and I would daily stop by his office and share with him about my day and personal life. I will never forget how I would constantly panic in his office about exams or presentations that I had coming up and he would always calm me down with his light hearted personality.

My friends and colleagues have all contributed immensely to my growth as a chemist and human being during my undergraduate and graduate studies. This list is highly extensive but I want to thank you all for keeping me sane and teaching me how to develop into a better person. I have had so much fun during my time in California and if it were not for every one of you then it would not have been as enjoyable.

I want to thank my boyfriend Dr. Gregory Lackner who has stood by my side during this past stressful year and continued to support me by listening to my daily complaints. I am so lucky to have met someone who encourages me to keep going and pursuing my dreams no matter how difficult that path might be. Thank you for being my everything and always being able to calm me down!

Last but not least I want to thank my whole family including Mama, Papa, my two sisters Vika and Lena, my sister's husband Dima, and my two little nephews Vanya and Andryusha. They have all contributed in helping me succeed throughout my studies by motivating me to keep moving forward and to attain the best goal that I can for myself. It is because of each one of them that I never gave up and kept going during my studies. Although you all think that I will forever be a student even as a post-doc, I promise that I will eventually have a real job!

The research presented herein was supported by grants from NSF CHE-1308231 and NIH EY021514.

CURRICULUM VITAE

Natalia Kozlyuk

EDUCATION

Doctor of Philosophy in Chemistry **2012-2017**
University of California, Irivne *Irvine, CA*

Bachelor of Science in Biochemistry **2008-2012**
University of Redlands *Redlands, CA*

RESEARCH EXPERIENCE

Structural Biology **2012–2017**
University of California, Irvine *Irvine, California*

Organic Synthesis **2012**
Loma Linda University *Loma Linda, CA*

Bio-inorganic Chemistry **2010–2012**
University of Redlands *Redlands, CA*

PUBLICATIONS

1. **Synthesis and the Characterization of Schiff-base Copper Complexes: Reactivity with DNA, 4-NPP and BNPP.** Kozlyuk, N.; Lopez, T.; Roth, P.; Acquaye, J. H. *Inorg. Chem. Acta* **2015**, *428*, 176-184.

2. ***In Situ* NMR Measurement of Macromolecule-molecule Bound Metal Ion Concentration.** Kozlyuk, N,; Sengupta, S.; Lupták, A.; Martin, R. W. *J. Biomol. NMR* **2016**, *64*, 269-273.

3. **Calcium Binding Dramatically Stabilizes an Ancestral Crystallin Fold in Tunicate $\beta\gamma$-Crystallin.** Kozlyuk, N.; Sengupta, S.; Bierma, J.; Martin, R. W. *Biochemistry* **2016**, *55*, 6961-6968.

4. **Cyclizing Pentapeptides: Mechanism and Application of Dehydrophenylalanine as a Traceless Turn-Inducer.** Le, N, D.; Riedel, J., Kozlyuk, N.; Martin, R. W.; Dong, V. M. *Org. Lett.* **2016**, *19*, 114-117.

PRESENTATIONS

Oral Presentations:

1. Calcium Binding Stabilizes an Ancestral Crystallin Fold in Tunicate $\beta\gamma$-Crystallin. 251^{st}American Chemical Society National Meeting and Exposition, March 2016.

2. Exploring the Interactions of Divalent Cations with Bicelle Mixtures and Biomolecules. University of Redlands Chemistry Seminar, November 2015.

3. NMR Studies of DNA Aligned in DMPC/DHPC/CS Bicelle Mixtures. Inter-Continental Advanced Materials for Photonics Summer School in Cambridge, England, June-July 2013.

4. Syntheses and the Characterization of Schiff-Base Copper Complexes: Reactivity with BNPP and DNA. Southern California Conference for Undergraduate Research, November 2011.

Poster Presentations:

1. Investigating the Structural and Metal Binding Properties of an Ancestral Eye Lens Crystallin from the *Ciona Intestinalis* Tunicate. Experimental Nuclear Magnetic Resonance Conference and American Chemical Society National Meeting and Exposition, March 2017 and April 2017.

2. *In Situ* Determination of Free [Mg^{2+}] and [Ca^{2+}] in Biomolecular NMR Samples Using an Internal dCDP Standard. Experimental Nuclear Magnetic Resonance Conference, April 2015.

3. NMR Studies of DNA Aligned in DMPC/DHPC/CS Bicelle Mixtures. Inter-Continental Advanced Materials for Photonics Summer School in Cambridge, England, June-July 2013.

4. Synthesis and the Crystal Structures of Schiff-Base Copper Complexes: Hydrolysis of Phosphodiester Bonds. Southern California Conference for Undergraduate Research, November 2010.

HONORS AND ACTIVITIES

1. Recipient of the Graduate Award for Departmental Service at UC Irvine-June 2016
2. Participant at a Cell-free Protein Synthesis Workshop at University of Gothenburg, Sweden-October 2014
3. Student Employee of the Year Award at University of Redlands-May 2012
4. Winner of the ACS Analytical Chemistry Award-May 2011
5. Nominee for the Barry Goldwater Scholarship at University of Redlands-November 2010
6. Member of the Chemistry Faculty Search Committee at University of Redlands-September-December 2010
7. Member of the American Chemical Society-August 2010-Present
8. Athlete of University of Redlands Track and Field Team-October 2009-May 2012
9. President of the University of Redlands Chemistry Club-February 2009-May 2012
10. University of Redlands Dean's List-January 2009-May 2012

11. Presidential Scholarship at the University of Redlands-August 2008-May 2012
12. Achievement Award at the University of Redlands-August 2008-May 2012

ABSTRACT OF THE DISSERTATION

Investigating the Structural and Metal Binding Properties of an Ancestral Eye Lens Crystallin

By

Natalia Kozlyuk

Doctor of Philosophy in Chemistry

University of California, Irvine, 2017

Associate Professor Rachel W. Martin, Chair

$\beta\gamma$-crystallins are structural proteins in the eye lens that refract light to produce an image. These proteins are found at extremely high concentrations in the lens and must remain soluble and transparent. If their solubility is perturbed due to a mutation, chemical damage, or a disturbance in metal ion homeostasis, then cataract can develop and cloud the eye lens. In order to understand more about the evolutionary origin of the structure and aggregation of these proteins in the human eye lens, the structure and metal binding properties of an ancestral Ca^{2+} binding $\beta\gamma$-crystallin found in the *Ciona intestinalis* tunicate were investigated using biophysical characterization techniques such as fluorescence, CD, ITC, DLS and solution-state NMR. It was found that the tunicate crystallin has a conformational change upon addition of Ca^{2+} and other divalent cations. This protein is highly stabilized both chemically and thermally upon binding to Ca^{2+} and it binds more strongly than has been previously reported for other Ca^{2+} binding $\beta\gamma$-crystallins. It was also found that this crystallin interacts with other divalent cations, all of which thermally stabilize the protein. Although divalent metal ions raise the melting temperature of the tunicate crystallin, aggregation is induced by the interaction with some of these metal ions well below the melting temperature. Several solution-state NMR techniques were developed in order to solve the structure of this tunicate $\beta\gamma$-crystallin and other related biomolecules in the presence of

divalent metal ions. One of the methods uses DLPC/DHPC bicelles, a low-temperature alignment medium, to obtain long range distance and angular restraints of dynamic and heat sensitive biomolecules in the presence of divalent metal ions. These restraints are determined via measurement of residual dipolar couplings, where J-couplings of a biomolecule in isotropic solution are compared with the J+D values for the biomolecule in the presence of an alignment medium. If there is a change in this peak splitting, then alignment of the biomolecule is occuring. Another technique involves using a small molecular probe dCDP and ^{31}P NMR to determine the macromolecule-free and macromolecule-bound divalent metal ion concentrations in NMR samples out of a total amount of divalent metal ions put into the system.

Chapter 1

Calcium binding dramatically stabilizes an ancestral crystallin fold in tunicate $\beta\gamma$-crystallin.

1.1 Background

The $\beta\gamma$-crystallin fold is an ancient structural motif found in diverse organisms from all three domains of life. In organisms without eyes, e.g. archaea [1], bacteria [2], tunicates [3], and sponges [4], $\beta\gamma$-crystallins serve as calcium-binding proteins. In vertebrates, they are primarily found in the eye lens, where they play an important role in controlling the refractive index gradient of this specialized tissue. The ubiquitous $\beta\gamma$-crystallins of the vertebrate lens are believed to have descended from an ancestral single-domain Ca^{2+}-binding crystallin by a process that included gene duplication resulting in two copies of the double Greek key domain per chain, as well as selection for high refractive index, concomitant with the loss of Ca^{2+}-binding functionality [5].

Phylogenetic analysis suggests that the $\beta\gamma$-crystallin superfamily, ubiquitous in vertebrates, evolved from a common ancestor also related to the sponge crystallin [4] and the spherulins of slime molds [6]. The single-domain $\beta\gamma$-crystallin of the tunicate, *Ciona intestinalis*, (*Ci*-$\beta\gamma$-crystallin), appears to be representative of the single-domain ancestor of the vertebrate $\beta\gamma$-crystallin fold. However, the story of $\beta\gamma$-crystallin evolution is not a simple progression from simple to complex; the calcium-binding $\beta\gamma$-crystallin from the sponge *Geodia cydonium* has two domains linked by an interdomain interface; however the relative orientation of its its domains is reversed with respect to that of its vertebrate orthologs [7]. Two-domain crystallins in microbes may have evolved via a different pathway after the divergence of single-domain ancestors, as evidenced by differences in the arrangement of the β-strands [8], as well as the absence of the Tyr-corner structures conserved in vertebrate members of the superfamily [9] and even the Trp corners thought to serve as critical folding nuclei [10].

Many microbial $\beta\gamma$-crystallins such as spherulin 3a from the slime mold *Physarum polycephalum* and protein S from the soil bacterium *Myxococcus xanthus* increase in stability upon binding Ca^{2+} [11, 12]. The C-terminal domain of M-crystallin from the archaeon *Methanosarcina acetivorans* binds Ca^{2+} with only moderate to low affinity (K_d= 35 μM and 200 μM, for two different sites); however ion binding has a profound effect on the protein. Solution NMR structures reveal that both the apo and holo forms adopt the canonical $\beta\gamma$-crystallin fold, however in the holo form most of the β strands are longer, and a number of disorganized loops surrounding the metal binding site become much more ordered relative to the apo form. The protein stability also increases upon Ca^{2+} binding, with T_m values of 55 °C and 71 °C in the presence and absence of Ca^{2+}, respectively [13]. This behavior is even more pronounced for some other microbial crystallins; the bacterial crystallin proteins of *Yersinia pestis* [10] and *Caulobacter crescentus* [14], and *Hahella chejuensis* [15] are fully or partly unstructured in the absence of calcium ions and adopt the characteristic double Greek key arrangement only upon binding Ca^{2+}.

In general, crystallins have been recruited from proteins of diverse function [16], leading to situations where it is difficult for multiple functions to be selected for simultaneously. This results in divergence in properties of the lens and non-lens proteins [17], or even of different isoforms within the lens [18]. It has been suggested that the lack of Ca^{2+} binding is essential for vertebrate lens protein function. In a series of mammalian γB-crystallin variants, introducing features critical for the microbial crystallin Ca^{2+}-binding sites negatively impacted the protein stability, particularly in the presence of Ca^{2+} [5]. The conclusions of this study suggest that loss of Ca^{2+}-binding ability is necessary prior to selection for high stability, due to Ca^{2+}-induced destabilization, particularly in single-domain proteins that lack the stabilizing influence of the interdomain interface. On the other hand, it has also been shown that bovine γB-crystallin binds Ca^{2+} ions, stabilizing its fold and playing a role in maintaining a homeostatic concentration of Ca^{2+} in the cell [19]. Clearly, the relationship between Ca^{2+}-binding and $\beta\gamma$-crystallin function in the vertebrate eye lens is not straightforward. Here we investigate the tunicate *Ciona intestinalis* $\beta\gamma$-crystallin because of its unique evolutionary position between the microbial crystallins and the vertebrate lens proteins. Although the tunicate does not have an eye lens, these crystallins are found in organs rich of Ca^{2+} (ocellus and otolith) which are responsible for sensing depth and light when the organism swims [16]. We show that the tunicate $\beta\gamma$-crystallin binds Ca^{2+} with a high affinity, and that Ca^{2+}-binding greatly stabilizes the protein against both thermal and chemical denaturation. We also compare and contrast structures of the Ca^{2+} binding site of the tunicate $\beta\gamma$-crystallin with that of other $\beta\gamma$-crystallins in order to look more closely as to the structural evolution of depletion of Ca^{2+} binding.

1.2 Materials and Methods

1.2.1 Gene construction, protein expression and purification

A plasmid containing the *Ci*-$\beta\gamma$-crystallin gene, codon-optimized for *Escherichia coli*, was purchased from Blue Heron Biotechnology (Bothell, WA). Primers for cloning were purchased from Integrated DNA Technologies (Coralville, IA) and used to amplify the crystallin gene containing restriction sites for NcoI and XhoI. After PCR, the gene was cloned into a pET28a(+) vector (Novagen, Darmstadt, Germany). *Ci*-$\beta\gamma$-crystallin was overexpresed in a Rosetta *Escherichia coli* cell line (DE3) using Studier's auto-induction protocol [20] for 20-24 hours at 25 °C. The cells were lysed, spun down and dialyzed overnight into a buffer containing 10 mM piperazine (pH 6), 10 mM NaCl, 0.05 % NaN_3. The protein was purified with an anion exchange column, eluting at $\sim$ 200 mM NaCl in 10 mM piperazine, EDTA was added to the samples and size exclusion was performed, eluting into 10 mM Tris-HCl buffer (pH 7.1), 0.05 % NaN_3. SDS PAGE and ES MS were performed to verify the identity of the purified protein (Figure A.1 and Figure A.2).

A plasmid containing wild-type human γS-crystallin, an N-terminal 6x His tag and a TEV protease cleavage sequence was amplified by PCR. The PCR product was cloned into a pET28a(+) vector (Novagen, Darmstadt, Germany). WT human γS-crystallin was overexpresed similar to *Ci*-$\beta\gamma$-crystallin for both ^{15}N labeled and natural abundance expressions and purified as stated in [21]. After purification, EDTA was added and the protein samples were dialyzed in 10 mM Tris-HCl (pH 7.1), 0.05 % NaN_3.

All buffers were deionized using a Profinity IMAC uncharged resin (Biorad) for all subsequent experiments.

1.2.2 Circular dichroism spectroscopy

Purified tunicate $\beta\gamma$-crystallin was diluted to 0.075 mg/mL in 10 mM Tris-HCl buffer (pH 7.1) for full circular dichroism spectra and in 10 mM HEPES buffer (pH 7.1) for unfolding experiments in the presence of either 1 mM EDTA (0 mM Ca^{2+}) or 1 mM $CaCl_2$. Measurements were performed using a J-810 spectropolarimeter (JASCO, Easton, MD) equipped with a thermal controller. Data were recorded between 260 nm and 190 nm using a 1 nm bandwidth and a 4 second response for full circular dichroism spectra.

1.2.3 Fluorescence spectroscopy

Tryptophan fluorescence of purified tunicate $\beta\gamma$-crystallin was measured at concentrations of 0.1 mg/mL in 10 mM Tris-HCl buffer (pH 7.1), 0.05 % NaN_3 in the presence of either 1 mM EDTA or 1 mM $CaCl_2$ at room temperature. Data were acquired using a Varian Cary Eclipse fluorescence spectrophotometer with 10 nm excitation slits, and an excitation wavelength of 280 nm. Each spectrum is the average of three scans. The ratio of the signals at 360 nm, (corresponding to solvent-exposed tryptophans), and at 320 nm (buried tryptophans) were used to monitor protein unfolding during thermal and chemical denaturation experiments.

Thermal denaturation experiments were performed over a temperature range from 17-100 °C in two degree increments. As for the fluorescence spectra, the buffer used was 10 mM HEPES (pH 7.1), 0.05 % NaN_3. The sample temperatures were increased using a Quantum Northwest TC 1 temperature controller with a two minute equilibration at every temperature point. Data were fit to a two-state equilibrium unfolding model in Mathematica to determine the thermal denaturation temperature (T_m) of each sample. Thermal denaturation experiments using intrinsic tryptophan fluorescence were also verified with DSC experiments in the absence and presence of 1 mM $CaCl_2$ in 10 mM MES buffer (pH 7.1) (Figure A.3). Chemical denaturation experiments were performed with increasing concentrations of urea or guani-

dinium hydrochloride in 10 mM Tris (pH 7.1), 0.05 % NaN_3 in the presence of 1 mM EDTA or 1 mM $CaCl_2$. Samples were allowed to equilibrate for about 24 hours with guanidinium hydrochloride and for 48 hours with urea before fluorescence spectra were acquired. Each point in the spectrum is an average of 12 measurements. To determine the Gibbs free energy at room temperature and the dependence of ΔG on denaturant concentration (ΔG°_{w} and m, respectively), denaturation data were fit to either a two-state or a three-state model in Mathematica as performed by Morjana, et al [22] depending on the presence or absence of an intermediate.

1.2.4 Isothermal titration calorimetry

ITC measurements were performed using a MicroCal VP-ITC microcalorimeter. In all cases, the protein sample and $CaCl_2$ solutions were degassed prior to titration. A titration consisted of 3 μL injections of 5 mM $CaCl_2$ to a protein sample in 10 mM Tris-HCl (pH 7.1), 0.05 % NaN_3 every 300 seconds. Overall 60 titrations were carried out. To subtract the heat of dilution, 5 mM $CaCl_2$ was titrated into 10 mM Tris-HCl (pH 7.1), 0.05 % NaN_3 and the data were subtracted from the protein titration data. Two experimental runs were performed; one with 386 μM and one with 405 μM. The reported fit parameters (Table 1.1) are the mean, and the error bars are the standard deviations between them. ITC data were analyzed using Mathematica and the fitting functions are shown in the SI.

1.3 Results

1.3.1 Unlike human γS-crystallin, *Ci*-βγ binds Ca^{2+} with strong affinity.

Isothermal titration calorimetry (ITC) was performed in order to measure the Ca^{2+}-binding affintity of the tunicate βγ-crystallin (Figure 1.1). The data were best fit to a sequential binding model, and binding at both sites was enthalpically driven (Table 1.1). The binding constants for the two sites were found to be 5.0 x 10^7 M^{-1} and 8.58 x 10^6 M^{-1} with an overall dissociation constant of 0.048 μM ($K_d = \frac{1}{\sqrt{K_1 K_2}}$), indicating a strong affinity for Ca^{2+}. The flatter portion of the curve is where sequential binding of Ca^{2+} occurs at the two sites. When the higher affinity site is saturated, the lower affinity site binds the rest of the Ca^{2+}, representative of the steep part of the curve. Other thermodynamic parameters were extrapolated from the best fit model and are tabulated in (Table 1.1). In contrast, the ITC thermogram of WT human γS-crystallin (Figure A.4) showed no binding of Ca^{2+}, even at a 5 mM concentration, which is consistent with its lack of Ca^{2+} binding sites [5].

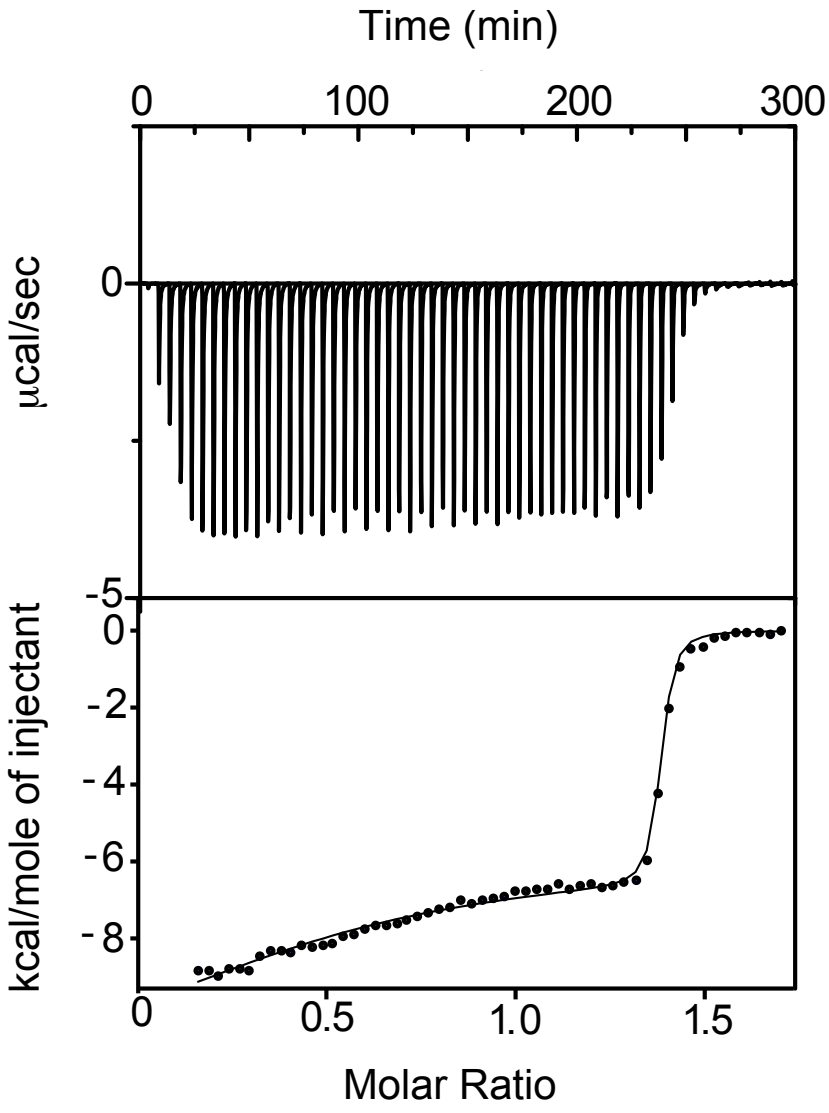

Figure 1.1: Thermogram demonstrating the binding of Ca^{2+} to tunicate $\beta\gamma$-crystallin. Ca^{2+} (5 mM) was titrated into 386 μM protein sample in 10 mM Tris-HCl (pH 7.1) and the curve was best fit to a sequential binding model.

Table 1.1: Thermodynamic parameters for binding of Ca^{2+} to *Ci*-$\beta\gamma$-crystallin.

	K (M^{-1})	ΔH (kcal/mol)	ΔS (cal/mol·K)	ΔG (kcal/mol)
Site 1	5.0 x 10^7±5.8 x 10^4	-9.9±0.21	3.7	-11
Site 2	8.6 x 10^6±5.0 x 10^5	-6.9±0.29	8.4	-9.4

1.3.2 Ca^{2+} binding does not change the secondary structure of *Ci*-$\beta\gamma$-crystallin

Although the protein binds Ca^{2+} with relatively strong affinity, circular dichroism (CD) and fluorescence data do not indicate significant changes in protein structure upon addition of 1 mM Ca^{2+}, representing a 100:1 Ca^{2+}: protein stoichiometric ratio. The CD spectra in the presence and absence of Ca^{2+} are almost identical, indicating that there is very little change in the secondary structure of the protein. The strong minimum around 218 nm under both conditions (Figure 1.2a) is consistent with the protein remaining in a mostly β-sheet conformation. With the addition of 1 mM Ca^{2+}, the intrinsic tryptophan fluorescence intensity is slightly increased at its peak maximum compared to the fluorescence spectrum in the presence of 1 mM EDTA (Figure 1.2b), however the emission wavelength does not shift, suggesting that the environment of the two tryptophans remains mostly unchanged.

1.3.3 The resistance of *Ci*-$\beta\gamma$-crystallin to both thermal and chemical denaturation dramatically increases upon binding Ca^{2+}

Thermal denaturation experiments were performed using the intrinsic tryptophan fluorescence over a 17-100 °C temperature range. In globular proteins, the signals from the solvent-exposed and buried tryptophans appear at approximately 360 and 320 nm, respectively. In this case, the emission maxiumum of the folded protein appears at 332 nm. Here unfolding is monitored using the ratio of the 360/330 peak intensities, normalized to plot the fraction unfolded as a function of temperature (Figure 1.3). Ca^{2+} binding results in a dramatic increase in resistance to thermal denaturation. In the absence of Ca^{2+}, the protein begins to unfold at a temperature as low as 35 °C and fully denatures by about 70 °C, with a T_m of 45.8 °C. Upon addition of Ca^{2+}, the temperature at the onset of denaturation rises to about 83 °C, while T_m increases to 94.2 °C. Denaturation of both the apo and the holo forms of

the protein were reversible upon cooling to the initial temperature.

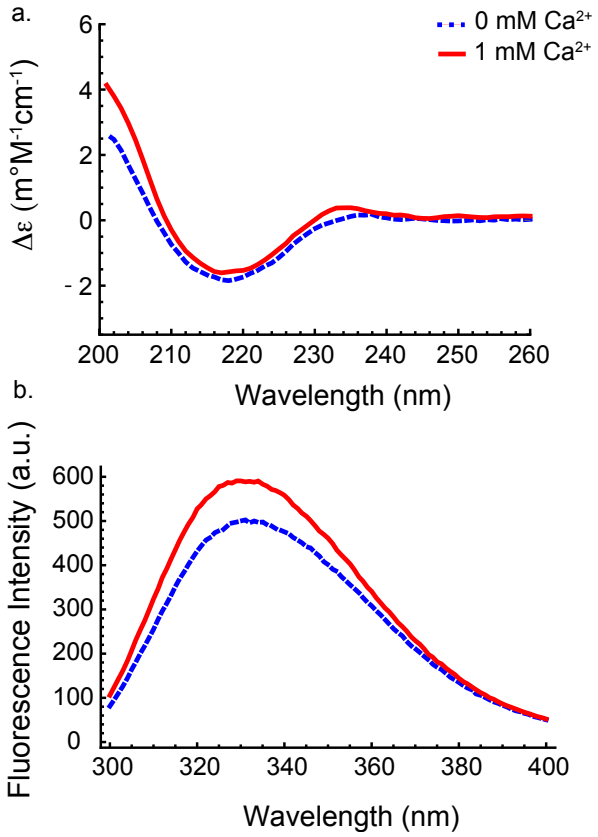

Figure 1.2: (a) The CD spectra of both the apo (blue dashed line) and holo (red solid line) forms of tunicate $\beta\gamma$-crystallin display strong minima at 218 nm, indicating primarily β-sheet secondary structure that does not significantly change upon the addition of Ca^{2+}. (b) Similarly, the intrinsic tryptophan fluorescence signal displays only a slight increase in intensity as a result of Ca^{2+} binding. The wavelength of the emission maximum does not shift, indicating that the environment of the Trp residues remains mostly unchanged.

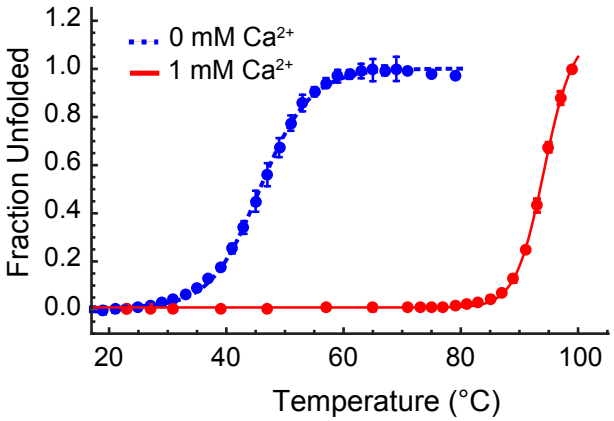

Figure 1.3: Thermal denaturation curves showing the thermal stability of the protein measured over a range of 17-100 °C. The holo form of the protein shows an increase in thermal stability compared with the apo form. The T_m increases from 45.8 °C to 94.2 °C upon addition of Ca^{2+}. Open circles indicate reversibility of the experiment.

Binding to Ca^{2+} also protected the *Ci*-$\beta\gamma$-crystallin against chemical denaturation by both GndHCl and urea. Protein unfolding in the presence of both denaturants was established by the observation of that the emission maximum for the intrinsic tryptophan fluorescence shifts by about 30 nm with the addition of the maximum denaturant concentration (Figure A.5). In the absence of Ca^{2+}, the protein begins to denature at concentrations of GndHCl as low as 0.25 M and keeps unfolding until about 3 M GndHCl has been added (Figure 1.4a) having a $[\text{denaturant}]_{1/2}$ of 1.75 M. In the presence of Ca^{2+}, GndHCl unfolding curves show gradual unfolding initiated again at 0.25 M, but the steeper unfolding is not initiated until 3 M GndHCl (Figure 1.4a). The same experiment for the holo form indicates the presence of an intermediate and the data were therefore fit to a three-state model with two transition points at $[\text{denaturant}]_{1/2}$ of 0.74 and 4.08 M. The overall ΔG°_w was found to be 5.08 kcal $\cdot$ mol^{-1} for the two unfolding transitions in the presence of Ca^{2+} as compared to 2.77 kcal $\cdot$ mol^{-1} in the absence of Ca^{2+}. Refolding experiments in the absence of Ca^{2+} were found to be reversible but in the presence of this divalent metal, the protein only refolded back to its intermediate state instead of fully back to its native state. ΔG°_w, m, and $[\text{denaturant}]_{1/2}$ are tabulated in Table 1.2 for GndHCl.

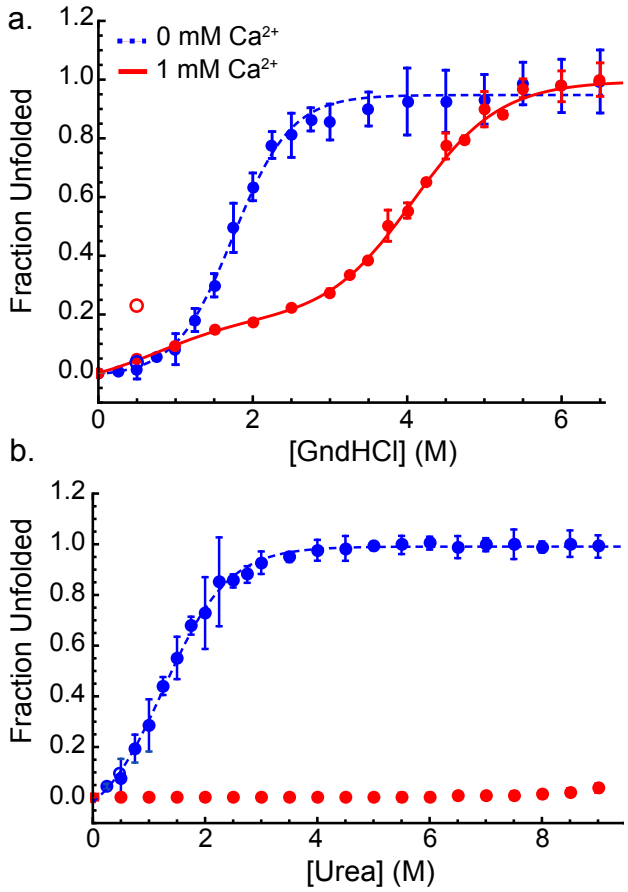

Figure 1.4: The *Ci*-$\beta\gamma$-crystallin is resistant to chemical denaturation with (a) GndHCl and (b) urea upon addition of Ca^{2+}. Open circles indicate the reversibility of the experiment. Denaturation of the apo form is fully reversible in both denaturing conditions, while the holo form refolds to the intermediate state in the GndHCl denaturing conditions.

Resistance to unfolding by urea is even more dramatically increased in the presence of Ca^{2+}. Ca^{2+} stabilizes *Ci*-$\beta\gamma$-crystallin against detectable unfolding even at very high urea concentrations approaching saturation. In the absence of Ca^{2+}, the protein begins to unfold starting at 0.25 M urea and continues to unfold until 5 M urea (Figure 1.4b). Compared with the GndHCl data for the apo from of the protein, the $[\text{denaturant}]_{1/2}$ was lower (1.26 M) indicating that the protein was not as stable in urea. Refolding experiments showed that the unfolding curve was reversible upon lowering the denaturant concentration.

Table 1.2: Thermodynamic parameters for guanidinium hydrochloride denaturation.

	$[\text{denaturant}]_{1/2}$ (M)	ΔG°_{w} (kcal/mol)	m (kcal/mol·M^{-1})
GndHCl (apo)	1.75	2.8 ± 0.095	1.6 ± 0.17
GndHCl (holo N → I)	0.74	0.77 ± 0.72	1.0 ± 0.59
GndHCl (holo I → U)	4.08	4.3 ± 0.37	1.1 ± 0.087

1.4 Discussion

Ci-$\beta\gamma$-crystallin strongly binds Ca^{2+}, and binding of this divalent metal ion dramatically increases the stability of the protein to denaturation by heat, GndHCl, and urea. The addition of Ca^{2+} stabilized the protein structure, where the midpoint of the transition temperature increased by almost 50 °C, from 45.8 °C to 94.2 °C. Previous studies have shown that the binding of Ca^{2+} stabilizes the structures of many non-lens $\beta\gamma$-crystallins such as Protein S and Spherulin 3a, which are microbial proteins produced during stress [10]. The T_m of the apo form is comparable to those of the microbial $\beta\gamma$-crystallins, (i.e. T_m of Flavollin is 47.3 °C, Rhodollin is 45.2 °C, Clostrillin is 44.6 °C [23]), however the increase in the transition temperature of the holo form is much higher than what has previously been observed for other proteins. This observation can perhaps be attributed to the tighter binding affinity of *Ci*-$\beta\gamma$-crystallin for Ca^{2+}.

Ci-$\beta\gamma$-crystallin bound Ca^{2+} at both of its sites with a higher affinity than previously observed for many non-mammalian $\beta\gamma$-crystallins (i.e. overall K_d for M-crystallin is 32 μM, Clostrillin is 4 μM and for rhodollin crystallin is 370 μM). The data were fit to a sequential binding model in which one site has a higher K_d than the other; K_{d1} is 0.020 μM and K_{d2} is 0.12 μM. Despite the high Ca^{2+} affinity of this protein, CD and intrinsic tryptophan fluorescence spectra did not show dramatic changes in secondary structure, even upon addition of 100:1 stoichiometric ratio of Ca^{2+} to protein. This result is consistent with other studies showing that the binding of Ca^{2+} does not induce major conformational changes in protein S and spherulin 3a [19].

The microbial $\beta\gamma$-crystallins act as Ca^{2+} storage proteins, while most of the vertebrate $\beta\gamma$-crystallins appear to lack functional Ca^{2+} binding sites. Questions still remain about the reason the human $\beta\gamma$-crystallin evolved to lose its metal ion binding sites, and whether the high stability of the mammalian proteins, even without binding Ca^{2+}, represents a necessary tradeoff in function. Disturbance in Ca^{2+} homeostasis is one way that cataract can develop in the eye lens [24]. The Ca^{2+} sites remain functional in some vertebrate $\beta\gamma$-crystallins (e.g. bovine γB), potentially contributing to the regulation of Ca^{2+} homeostasis in the mammalian lens. In Figure 1.5, we compare the sequences of M-crystallin, bovine γ-crystallin, clostrillin microbial crystallin, human γS-crystallin, *Ci*-$\beta\gamma$-crystallin and the *Geodia cydonium* sponge crystallin, for which the binding site is highly similar to that of the *Ci*-$\beta\gamma$-crystallin. This comparison provides insight into the loss of Ca^{2+} binding sites in some vertebrate crystallins. Despite their very similar folds, the sequences of the mammalian $\beta\gamma$-crystallin family have diverged from the signature Ca^{2+} binding sequence of NDXXSS [25] in such a way that the Ca^{2+} binding sites have a lower binding affinity for Ca^{2+} due to the substitution of some functionally important residues in the signature sequence. Comparing the $\beta\gamma$-crystallins from different organisms shows that there are only seven positions that are strictly conserved, and nine that are functionally conserved. Of the residues involved in calcium binding, only one is in a strictly conserved site and another in a functionally conserved site. By comparing sequences of $\beta\gamma$-crystallins with functional calcium binding sites to those that are unable to bind Ca^{2+}, it can be seen that some structural rearrangement has taken place during the selection of these proteins to fulfill their role in the lens (Figure 1.5). This structural rearrangement appears to eliminate the necessary Ca^{2+} binding contacts, eliminating some sidechain carbonyls and reorienting other backbone carbonyls that were involved in binding. Additionally, two positively charged residues at or near the binding site have been added, leading possibility of forming salt bridges with the negatively charged residues, which would both disrupt the interactions with Ca^{2+} and generate an electrostatic repulsion between

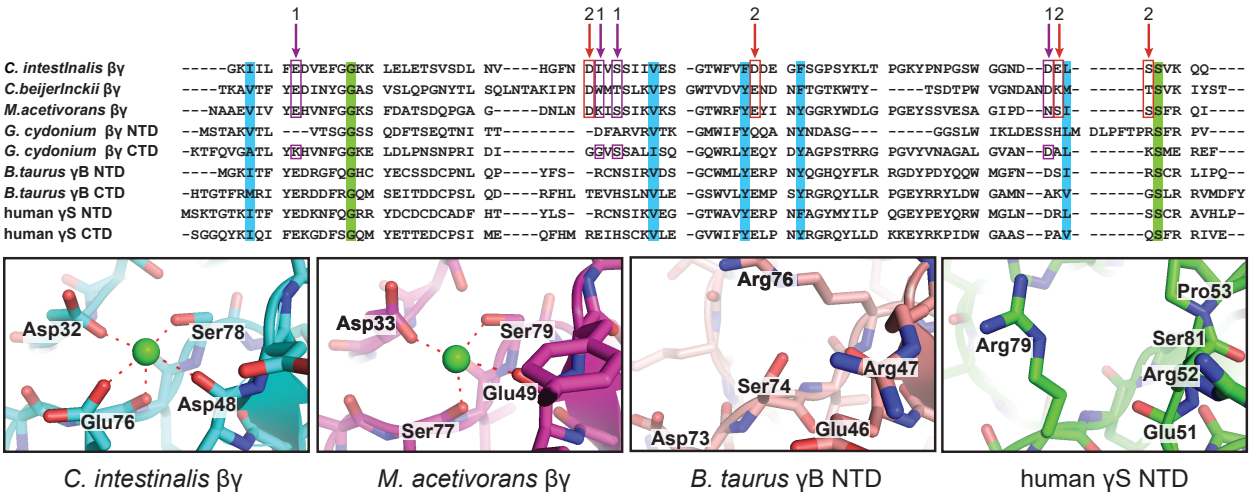

Figure 1.5: (Top) Sequence alignment of $\beta\gamma$-crystalllins from *C. intestinalis*, *C. beijerinckii*, *M. acetivorans*, *G. cydonium*, *B. taurus*, and *H. sapiens*. Residues highlighted in green are strictly conserved, while residues highlighted in cyan are functionally conserved. Boxes enclose residues involved in calcium binding as determined by polar contacts made in the structure. Arrows indicate the calcium binding residues of sites 1 and 2. (Bottom) View of calcium binding site 2 in *C. intestinalis* $\beta\gamma$, *M. acetivorans* $\beta\gamma$, *B. taurus* γ-crystallin and human γS-crystallin.

the residue and the calcium ion. It is likely that other subtle and complicated nonlinear binding effects play a role in the loss of Ca^{2+} binding that has occurred during the evolution of vertebrate crystallins. More experimental data on related proteins is needed to fully characterize these effects.

Although the bovine γ-crystallin is able to bind Ca^{2+}, it does so with weaker affinity (90 μM) as compared to the tunicate crystallin. The residues involved in Ca^{2+} binding are similar to that of the tunicate (Glu 46, Arg 47, Asp 73, Ser 74) [19], but there is also a positively charged residue in the binding pocket which might be responsible for the weaker Ca^{2+} affinity. Overall, the Ca^{2+} binding affinity decreases for $\beta\gamma$-crystallins, and in many cases Ca^{2+} binding destabilizes the proteins. The presence of the additional domain (CTD) in the cow and human crystallins has been hypothesized to compensate for the evolutionary decreased ability for Ca^{2+} binding and increase the protein's stability [5].

As for thermal denaturation, results from the chemical denaturation experiments also showed that the addition of Ca^{2+} greatly stabilized *Ci*-$\beta\gamma$-crystallin, possibly due to the tighter packing of the protein in the presence of the divalent ions. When GndHCl was used as the denaturant, the protein was more stable in the holo form as compared to the apo form. Unfolding of the holo form, but not the apo form, proceeded via an intermediate. The $[GndHCl]_{1/2}$ was 1.8 M in the apo form and 0.74/4.1 M for the two unfolding transitions respectively, in the holo form. The $[GndHCl]_{1/2}$ of the apo form were similar to those of many other $\beta\gamma$-crystallins such as those of the microbial crystallins, however, the $[GndHCl]_{1/2}$ values for the holo form exceeded that which have been previously observed for single domain $\beta\gamma$-crystallins (i.e. protein S has a $[GndHCl]_{1/2}$ of 1.7 M, however, it only increases to 1.9 M in the presence of Ca^{2+} in contrast to this tunicate crystallin) [26, 27]. The overall free energy of unfolding was also consistent with the $[denaturant]_{1/2}$ where the protein was more stable and more resistant to denaturation in the presence of Ca^{2+} (5.08 in the holo form versus 2.77 kcal $\cdot$ mol^{-1} in the apo form). This observation is also consistent with the result that the T_m was higher for the tunicate crystallin in the presence of Ca^{2+} than for these microbial crystallins.

When urea was added to the tunicate protein in the presence of Ca^{2+}, the protein became completely resistant to unfolding. Vertebrate γB-crystallin has also been shown to resist denaturation by urea at pH 7 due to strong interactions between its two domains [12]. In the apo form, the $[urea]_{1/2}$ was 1.26 M, which is relatively unstable relative to other similar crystallins. The large difference in urea denaturation susceptibility between the apo and holo forms, coupled with the smaller difference in GndHCl sensitivity suggests some hypotheses about the mechanism of stabilization.GndHCl is an ionic denaturant that could shield the favorable electrostatic interactions between the positive Ca^{2+} and the negative residues at the binding sites, reducing the Ca^{2+}-protein interaction and allowing a loosening of the fold. On the other hand, urea denaturation has been hypothesized to occur either via direct or indirect mechanisms. The direct mechanism occurs when urea hydrogen bonds to the polar

groups of the proteins, which unfolds the protein and exposes the hydrophobic residues to solvation with the water molecules and urea. The indirect mechanism occurs when urea disrupts the water structure around the protein which weakens the hydrophobic effect and exposes those non polar residues to the solvent [28]. The ionic character of GndHCl may explain the lower resistance against this type of chemical denaturation in the holo form, as it is competing with the Ca^{2+} for the residues involved in the Ca^{2+} binding sites. Its ionic character could also be responsible for stabilizing an intermediate along the unfolding pathway of the holo form, however, this is not seen in the apo form. Urea, on the other hand, has little effect on electrostatics and primarily binds to the protein during denaturation via polar interactions. Thus, no denaturation is observed in the holo form of *Ci*-$\beta\gamma$-crystallin even at high concentrations, however, the lower $[\text{denaturant}]_{1/2}$ value for the apo form of the protein with urea as compared to GndHCl makes it seem that urea is a stronger denaturant for this protein in the absence of the stabilizing metal ions. Follow-up NMR experiments at varying concentrations presence of urea and GndHCl will be performed to further elucidate the differences in how the protein is chemically unfolded by these two denaturants.

The *Ciona intestinalis* $\beta\gamma$-crystallin, an ancestor of the vertebrate lens crystallins, binds Ca^{2+} with high affinity. In contrast, human γS-crystallin lacks many of the key residues involved in metal ion binding, and does not bind Ca^{2+}. In the tunicate protein, Ca^{2+} binding dramatically increases the protein's thermal and chemical stability, to a larger degree than has been previously observed for single domain $\beta\gamma$ crystallins. This result provides a basis for future studies of the evolution of vertebrate lens proteins from ancestral Ca^{2+}-storage proteins.

Chapter 2

Effects of divalent cations on the structure of tunicate $\beta\gamma$-crystallin.

2.1 Background

The Ca^{2+}-binding $\beta\gamma$-crystallins are ancestral to the ubiquitous $\beta\gamma$-crystallins that provide the structure and refractive index increment of the vertebrate eye lens. These proteins are found in microbes, fungi, and the tunicate *Ciona intestinalis*, which is part of phylum Chordata but lacks a fully formed eye lens. Despite this functional legacy, many of the vertebrate $\beta\gamma$-crystallins have evolved to eschew this metal binding property [1, 7, 23]. This may have happened as part of their selection for a higher refractive index or the duplication of the double Greek key domain [5], or simply genetic drift due to lack of positive selection. The addition of Ca^{2+} to the *C. intestinalis* $\beta\gamma$-crystallin (*Ci*-$\beta\gamma$) highly stabilizes the protein thermally up to 94 °C, and this protein binds Ca^{2+} with a higher affinity than previously observed for other $\beta\gamma$-crystallins with an overall K_d of 0.05 μM [29].

The otolith where the *Ci*-$\beta\gamma$-crystallin is found in the tunicate is composed of a calcium

carbonate-rich matrix. As in many other biominerals, Sr^{2+} may substitute for the Ca^{2+} in that matrix. Depending on the environment that the organism lives in, the otolith can contain high concentrations of trace metals such as cations of Mn, Fe, Ni, and Zn [30]. These heavy metals can be sequestered by proteins, potentially inhibiting, modifying and enhancing normal biological activity. Some protein-heavy metal interactions can be toxic, and it is important to investigate their effects on protein stability [31]. In the human lens, metal ions can play a role in cataract formation. For example, the presence of copper and zinc ions can promote nonamyloid aggregation of human γ-D crystallin, while Zn^{2+} decreases its thermal stability [32]. Binding of these metal ions to α-crystallin has shown to increase its chaperone activity; however, when α-crystallin is bound to human γ-D crystallin in the aging cell, binding to metal ions is reduced, resulting in oxidation and cataract [33].

Exploring the relationship between protein thermal denaturation and aggregation is important in understanding the mechanism of cataract and other diseases caused by protein conformational changes and aggregate deposition. These two biophysical properties are not always directly correlated, as aggregates can form at moderate concentrations below the protein's unfolding temperature [18]. For example, some of the human prion protein variants that accumulate and cause neurological diseases are not less thermally stable than their wild-type counterparts [34, 35]. Aggregation is not always due to protein unfolding or misfolding but can also be caused as a result of changes in protein-protein interactions in the folded state induced by sample conditions (pH, salt type and concentration, ligands, surfactants) and residue-solvent contacts. The protein's native conformation is an ensemble of substates that expand and compact, and which can cause proteins to aggregate at physiological conditions [36]. For example, the immune interferon protein rhIFN-γ has an expanded state with 9 % more solvent-exposed area than the compact state of the protein, and this is enough to cause aggregation [37, 38, 39]. Also, the human granulocyte colony stimulating factor rhGCSF aggregates at physiological conditions in its expanded conformation, which contains 15 % more exposed surface area relative to the native form [40].

Because the relationship between protein thermal stability and aggregation propensity is complex, it is crucial to understand the connection between these two biophysical properties in order to get more insight into the mechanism of protein deposition diseases such as cataract. The tunicate Ca^{2+}-binding $\beta\gamma$-crystallin is a great model system to study the effects of divalent metal ions on the protein structure and stability as this protein binds Ca^{2+} in its native form but may also be able to coordinate to a variety of other metal ions. In this chapter, we investigate the specificity of the tunicate crystallin binding and the ability of other divalent metal ions to stabilize the protein to thermal denaturation and aggregation.

2.2 Materials and methods

^{15}N labeled and natural abundace tunicate crystallin was expressed and purified using a protocol previously described in chapter 1.

2.2.1 Thermal denaturation

Thermal denaturation experiments were performed using intrinsic tryptophan fluorescence at 0.1 mg/mL protein concentrations in 10 mM HEPES (pH 7.1), 0.05 % NaN_3 buffer and in the presence of 1 mM $MgCl_2$, 1 mM $NiCl_2$, 1 mM $MnCl_2$, 1 mM $SrCl_2$, 1 mM $ZnCl_2$ or 1 mM $CoCl_2$ over a temperature range of 17-99 °C. Data were acquired using a Varian Cary Eclipse fluorescence spectrophotometer with 10 nm excitation slits, and an excitation wavelength of 280 nm. Each spectrum is the average of twelve scans. The sample temperatures were increased using a Quantum Northwest TC 1 temperature controller with a two minute equilibration at every temperature point. Data were fit to a two-state equilibrium unfolding model in Mathematica to determine the thermal denaturation temperature (T_m) of each sample.

2.2.2 Dynamic light scattering

Dynamic light scattering (DLS) experiments were acquired on a Malvern Zetasizer NS DLS instrument at concentrations of 3 mg/mL in 10 mM HEPES (pH 7.1), 0.05 % NaN_3 buffer in the presence of 1 mM divalent cation concentration. Experiments were performed over a 20-92 °C temperature range with a 1 °C/min heating rate. At each temperature, samples were equilibrated for 2 min before measurements were obtained in triplicate.

2.2.3 Isothermal titration calorimetry

ITC measurements were performed using a MicroCal VP-ITC microcalorimeter. A titration consisted of 3 μL injections of 10 mM divalent cation to a 400 μM protein sample in 10 mM Tris-HCl (pH 7.1), 0.05 % NaN_3 every 400 seconds and every 600 seconds with 10 mM $SrCl_2$. Overall 60 titrations were carried out. To subtract the heat of dilution, 10 mM divalent cation was titrated into 10 mM Tris-HCl (pH 7.1), 0.05 % NaN_3 and the data were subtracted from the raw protein data. ITC data were analyzed using Mathematica and the fitting functions are shown in the Appendix for chapter 1. The reported fit parameters (Table 2.1) are the mean, and the error bars are the standard deviations between them of three fitting iterations.

2.2.4 NMR experiments

Experiments were performed at 25 °C on a Varian ^{Unity}INOVA system operating at 800 MHz equipped with a $^{1}H/^{13}C/^{15}N$ 5 mm tri-axis PFG triple-resonance probe. ^{15}N-^{1}H HSQC experiments were acquired with 4 scans in the direct dimension and 64 scans in the indirect dimension at protein concentrations of 1.7 mM in the presence of 0 equiv, 1 equiv, 2 equiv, and 6.5 equiv of $MgCl_2$, $NiCl_2$, $ZnCl_2$, or $SrCl_2$.

2.3 Results and Discussion

In order to explore the selectivity of *Ci*-$\beta\gamma$-crystallin for Ca^{2+} over other divalent cations, the stability and binding properties of the tunicate crystallin were studied upon addition of $MgCl_2$, $NiCl_2$, $ZnCl_2$, $SrCl_2$, $CoCl_2$ and $MnCl_2$. In the presence of each divalent cation tested, the tunicate crystallin was more thermally stable than the apo form, which had a T_m of 46 °C (Figure 2.1). It was the most thermally stable in the presence of Ca^{2+}, as we have previously reported, with a $T_m \geq 94$ °C. This effect was almost as pronounced in the presence of Sr^{2+}, with a T_m of 91 °C. Sr^{2+} is an alkali earth metal with a similar ionic radius to Ca^{2+} (0.100 and 0.095 respectively), suggesting that it may be able to directly occupy the protein's Ca^{2+}-binding sites [41]. Mn^{2+} also provided thermal stabilization, although to a lesser degree. This may again be related to its larger size and lower effective nuclear charge as compared with the other metal ions tested. The presence of Zn^{2+} only slightly thermally stabilized the protein over the apo form, with at T_m of 53 °C, while other transition metals produced intermediate results.

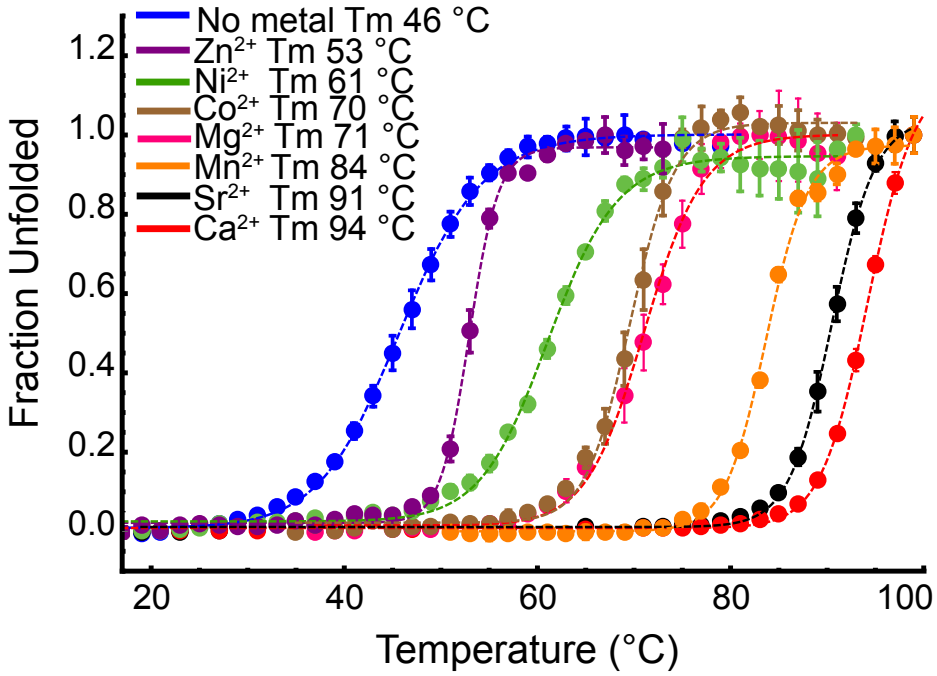

Figure 2.1: Thermal denaturation of *Ci-βγ* crystallin in the presence of 1 mM EDTA, $MgCl_2$, $NiCl_2$, $ZnCl_2$, $SrCl_2$, $CoCl_2$, $CaCl_2$ and $MnCl_2$. The presence of all divalent cations tested thermally stabilized the protein relative to the apo form; however the degree of stabilization varied from an increase in T_m of 7 °C (Zn^{2+}) to 48 °C (Ca^{2+}).

Dynamic light scattering (DLS) experiments were performed to test the aggregation propensity of the tunicate crystallin under thermal stress in the presence of the various divalent metal ions (Figure 2.2). These data indicate that the relationship between aggregation propensity and thermal stability is not simple for this protein. In the presence of its preferred metal ion, Ca^{2+}, the protein remained monomeric until around 82 °C. In the presence of Sr^{2+} this was increased to 88 °C, consistent with the result that this protein is very thermally stable when bound to both Ca^{2+} and Sr^{2+}. Although the apo form of the protein was the most susceptible to thermal denaturation, it was not the most aggregation-prone. The most aggregation-prone sample contained Ni^{2+}, where small aggregates in the range of 4-30 nm formed around 40-55 °C, and larger 1000 nm aggregates appeared near 78 °C. Zn^{2+} had a similar aggregation-inducing effect, with aggregates forming around 48 °C, compared to

52 °C in the absence of divalent cations. Zn^{2+} also caused the tunicate crystallin to form large aggregates around 70 °C, yet in the absence of any metal ion, those same aggregates did not form until the sample was heated to almost 90 °C. This result is consistent with the previous observation that Zn^{2+} causes protein aggregation in human γ-D crystallin [32]. Our DLS and thermal denaturation data suggest that this metal ion might be also unfavorably impacting the tunicate crystallin structure.

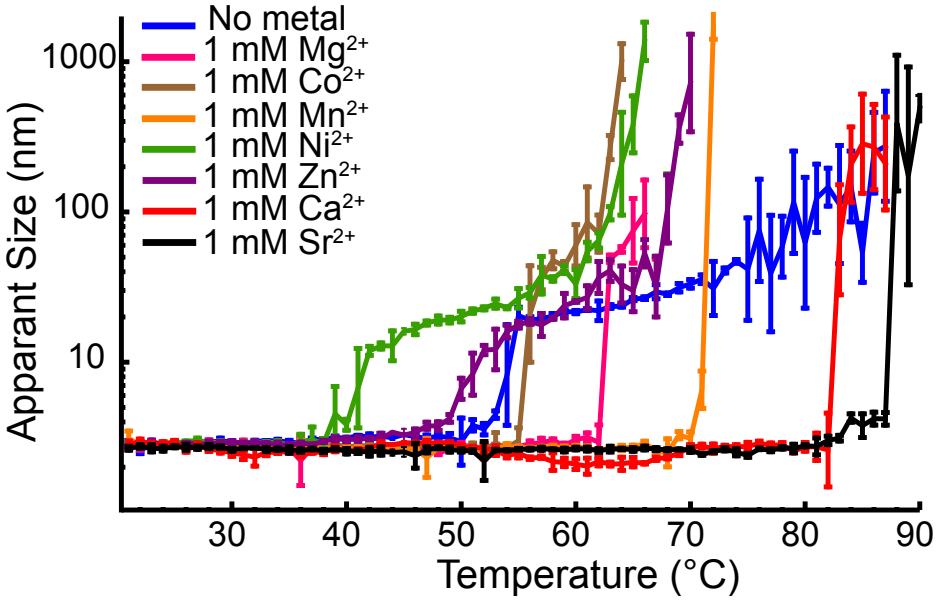

Figure 2.2: DLS measurements of tunicate crystallin in the presence of 1 mM EDTA, $MgCl_2$, $NiCl_2$, $ZnCl_2$, $SrCl_2$, $CoCl_2$, $CaCl_2$ and $MnCl_2$. Data were plotted up to the temperature when the majority of the protein crashed out and caused a reduction in signal intensity. The presence of Zn^{2+} and Ni^{2+} caused the protein to form aggregates at lower temperatures but the presence of Ca^{2+} and Sr^{2+} did not cause protein aggregation until 80-90 °C.

Isothermal titration calorimetry (ITC) data showed that the binding of tunicate crystallin to Ca^{2+} and Sr^{2+} proceeded via an exothermically driven two-site sequential binding mechanism where one site bound the metal ion tighter than the other site Figure 2.3 and Figure 2.4. Out of the two alkali earth metal ions, the crystallin bound its native Ca^{2+} ion with an overall higher affinity; K_1 and K_2 were 5.0 x 10^7 M^{-1} and 8.6 x 10^6 M^{-1}, respectively [29]. The K_1 and K_2 for Sr^{2+} binding were 3.3 x 10^7 M^{-1} and 8.5 x 10^5 M^{-1}, respectively Figure 2.1. This similar metal binding interaction can be related to alkali earth metals preferring to interact

more strongly with oxygens due to their hard Lewis acid properties. The coordination of Sr^{2+} with oxygens was shown in the crystal structure of the synaptotagmin I C_2B domain, demonstrating a similar interaction [42]. Like Ca^{2+}, Sr^{2+} can also tolerate a wide range of coordination spheres (6-8 ligands), and because of its similar size to Ca^{2+}, it should be able to fit into the binding sites of *Ci*-$\beta\gamma$-crystallin. Sr^{2+}, Ba^{2+} and trivalent lanthanides have been shown to replace Ca^{2+} in three of the four binding sites of thermolysin, a thermostable metalloproteinase [43, 31].

Compared with the binding mechanism of tunicate crystallin with $CaCl_2$ and $SrCl_2$, ITC data indicate different binding mechanisms for *Ci*-$\beta\gamma$-crystallin with $MgCl_2$, $NiCl_2$, $ZnCl_2$, $CoCl_2$ and $MnCl_2$. The isotherms of tunicate crystallin with the transition metal ions and Mg^{2+} demonstrated endothermic binding of these metal ions (Figure S1-S5). These endothermic binding curves might be the result of the release of water molecules, either from the protein or from the metal ion upon binding, since the reactivity of metal ions with water differs. For example, the alkali metals and the alkali earth metals (excluding Mg^{2+}) exchange their coordinated water molecules with bulk solvent on the rates of greater than 10^8 per second but the exchange rate decreases to 10^4-10^8 per second for Mg^{2+} and some first-row transition metals [44]. The binding mechanism of these divalent metal ions might also differ from that of Ca^{2+} and Sr^{2+} because the transition metal ions tested lie somewhere between hard and soft. As a result, these transition metal ions tend to interact more with sulfur and nitrogen atoms instead of oxygens which are preferred by Ca^{2+} and Sr^{2+}, hard Lewis acids. They also prefer different number of coordinations sites than Ca^{2+} [45]. For example, Zn^{2+} prefers a range of coordination sites that is lower than that of Ca^{2+}, ranging from 4 to 6 and prefers to bind histidine, cysteine and acidic residues. Ni^{2+} and Co^{2+} also prefer to bind similar residues as Zn^{2+} but favor an octahedral geometry [46]. Major binders of Mn^{2+} include oxygen atoms from carboxyl groups of acidic residues similar to the other metal ions histidine side chains but not cysteine residues [47].

Although Mg^{2+} is also an alkali earth metal, it showed a different mechanism of binding to tunicate crystallin from Ca^{2+} and Sr^{2+}; it appears to be similar to the binding mechanism with the transition metals. Such a difference in binding was also observed in calmodulin, a Ca^{2+} binding protein, which binds Sr^{2+} and Cd^{2+} much stronger than Mg^{2+} due to the coordination similarities and differences of the COO- groups in the side chains of Asp and Glu residues[41]. This difference in binding can be attributed to several factors. Mg^{2+} has shown to bind to more water molecules when bound to biomolecules than Ca^{2+} (1.5 versus 2.2 water molecules per metal ion site), which could mean that it might prefer to bind to overall solvent-accessible areas. In addition, this metal ion has a rigid inner coordination sphere and thus prefers an octahedral geometry around it. If that coordination site is perturbed, then a significant energy penalty is incurred [48]. Its smaller ionic radius versus that of the other alkali earth metals can also cause water to water repulsion during binding [45] and can prevent the metal ion from forming bidentate interactions which are commonly observed in Ca^{2+} structures [44]. Binding characteristics of Mn^{2+} have been shown to be similar to that of Mg^{2+} due to its similar size, but Mn^{2+} does not coordinate to as many water molecules [44].

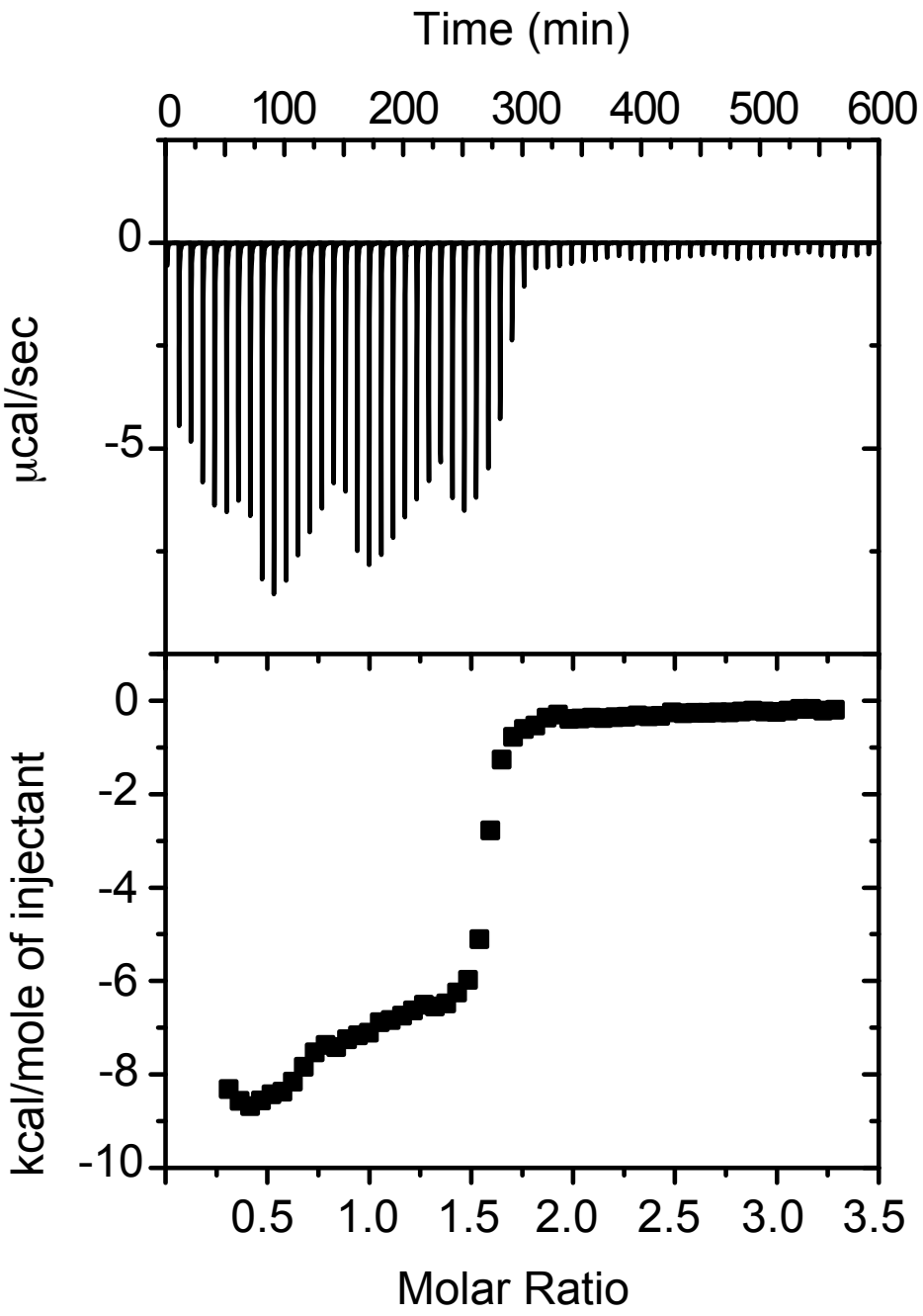

Figure 2.3: ITC binding isotherm of tunicate crystallin titrated with 10 mM $SrCl_2$ showed a similar binding mechanism to that with $CaCl_2$ (chapter 1).

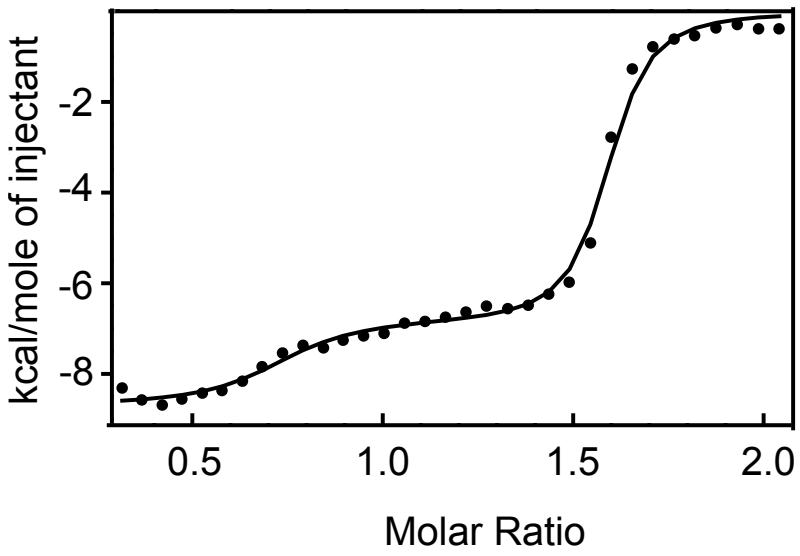

Figure 2.4: ITC binding isotherm of tunicate crystallin titrated with 10 mM $SrCl_2$ was fit to a sequential binding model with Mathematica similar to chapter 1. Molar ratio was cut off at 2 to obtain a better fit of the data.

Table 2.1: Thermodynamic parameters for binding of Sr^{2+} to *Ci*-$\beta\gamma$-crystallin.

	K (M^{-1})	ΔH (kcal/mol)	ΔS (cal/mol·K)	ΔG (kcal/mol)
Site 1	3.3 x 10^7±7.7 x 10^6	-8.9±0.17	4.5	-10
Site 2	8.5 x 10^5±1.6 x 10^5	-6.9±0.092	4.0	-8.1

^{15}N HSQC experiments were acquired to investigate whether the same residues were binding to Sr^{2+} as to Ca^{2+}, as might be expected from the similarity of their binding isotherms. For comparison, ^{15}N HSQC experiments were also acquired in the presence of the other divalent cations. One equiv, 2 equiv and 6.5 equiv of divalent cation were titrated into the protein and peak shifts from HSQCs (Figure S6) of each sample were calculated using the chemical shift perturbation equation: $\Delta\delta_{avg} = \sqrt{\frac{(\Delta\delta_N/5)^2+(\Delta\delta_H)^2}{2}}$. Chemical shift perturbations upon addition of various equivalents of Sr^{2+}, Mg^{2+}, Ni^{2+} and Zn^{2+} are plotted in Figure 2.5 a, c, e, g, with thresholds for large ($>$ 0.2 ppm) and moderate (0.06 - 0.2 ppm) perturbations shown

with the dotted lines. Residues for which the shift was less than 0.06 ppm were classified as unperturbed. These perturbations are represented on the X-ray crystal structures of the Ca^{2+}-bound protein (PDBID 2BV2) [3] in Figure 2.5 b, d, f, h.

Two regions consistently shifted in all the samples upon addition of divalent cations; residues 31-34 and 73-80. Residues Asp 32, Ile 33, Ser 35, Asp 75, Glu 76 and Ser 78 are responsible for binding Ca^{2+} in the native tunicate crystallin. Although the HSQC spectrum of the tunicate protein in the presence of Ca^{2+} was the closest to that in the presence of Sr^{2+} as compared to the presence of the other metal ions, the residues which shifted upon addition of Sr^{2+} were not identical to those responding to the addition of Ca^{2+} [29]. In the case of the other metal ions, most of the significant chemical shift perturbations were observed in the same loop region, which has a negative overall charge (Figure 2.5 b, d, f, h). The Mg^{2+} sample had the most residues that shifted as a function of metal ion and that could be the result of more nonspecific protein-metal ion interactions. Binding to more residues could explain the overall higher endothermic reaction of the Mg^{2+} ITC data. The Ni^{2+} sample had the most perturbed nitrogen-containing residues, which is consistent with Ni preferring to coordinate nitrogen containing atoms, unlike the alkali earth metals (Mg, Ca and Sr), which preferentially coordinate oxygen. Because Ni^{2+} is a paramagnetic ion, saturated Ni^{2+} concentrations caused peak broadening and thus peak disappearance upon protein binding. Overall, we can hypothesize that in the presence of Ni^{2+}, the protein thermally unfolds at a lower temperature as compared to in the presence of Mg^{2+} and Sr^{2+} because Ni^{2+} even at room temperature promotes the greatest nonnative conformational change due to the absence of many residues. This conformational change is what favors the room temperature unfolding and aggregation. Although we observe more peak shifts in the Mg^{2+} sample, those peak shifts correspond to conformational changes that are less pronounced.

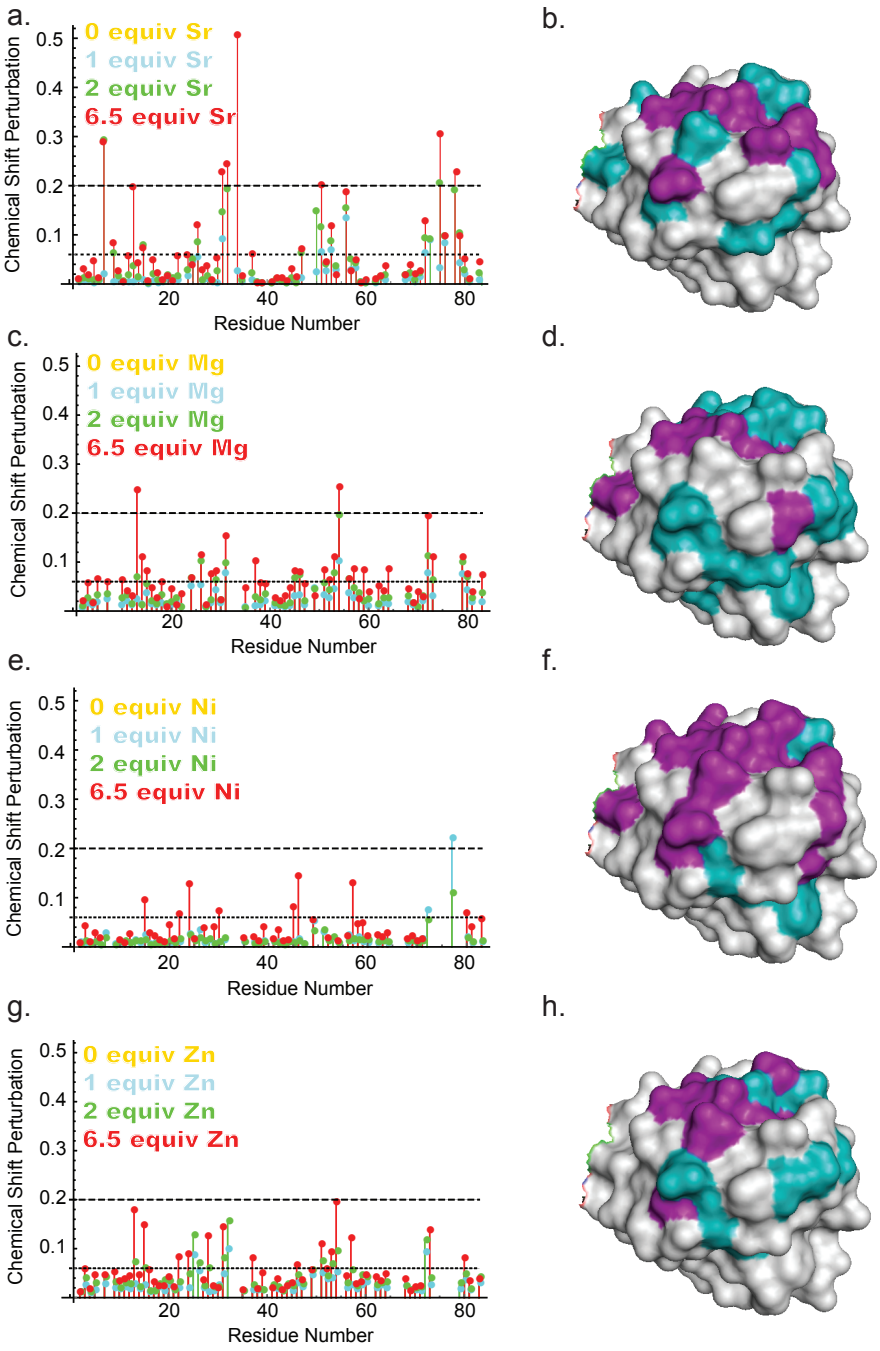

Figure 2.5: Chemical shift perturbation for tunicate $\beta\gamma$-crystallin with increasing Sr^{2+} (a), Mg^{2+} (c), Ni^{2+} (e), and Zn^{2+} (g) calculated from ^{15}N HSQC experiments. The residues that shift the most fall above the 0.2 cut off and they are represented in the X-ray crystal structure (PDBID 2BV2) in purple, residues that minimally shift are between 0.06 and 0.2 and are represented in teal, and residues that do not shift or were unassigned are represented in grey (b, d, f, g).

In conclusion, we have shown that Mg^{2+}, Ni^{2+}, Mn^{2+}, Sr^{2+}, Zn^{2+} and Co^{2+} all cause thermal stabilization of tunicate $\beta\gamma$-crystallin. In the presence of all the metal ions, we have also shown that the protein begins to aggregate below its melting temperature. Additionally, the binding of tunicate crystallin to Sr^{2+} occurs via a similar mechanism to that of binding to Ca^{2+}. The residues involved in the binding of tunicate crystallin to Sr^{2+} are not identical to that of binding to Ca^{2+}, however, the NMR data shows more of a specificity for the binding for this metal ion than for the other metal ions.

Chapter 3

Solution-state NMR structure determination of tunicate $\beta\gamma$-crystallin in the apo and holo form.

3.1 Background

There are several methods that are currently used to solve structures of biomolecules including X-ray crystallography, NMR and cryo-EM. Out of these three, the main ones that are used in structure determination of small to medium sized biomolecules are X-ray crystallography and solution-state NMR. Each of these techniques has its own advantages and disadvantages. X-ray crystallography has been widely used as the primary method for biomolecular structure determination due to the ease of its data collection and analysis over NMR once a good quality crystal is obtained. Crystallography is also the method of choice when working with biomolecules over 30 kDa, however, unlike with NMR, very little information about protein dynamics can be obtained and the crystal-packing forces of multi-domain proteins

can cause deviations from physiologically relevant domain orientations [49]. Even though solution-state NMR is mainly used to determine the structures of small biomolecules, it is powerful in that it enables the study of conformational heterogeneity of macromolecules by providing high resolution data regarding protein dynamics over ps-s time scales [50]. In addition, it is useful in characterizing protein folding, stability and function [51]. In the 1970s, it was shown that, using NMR, it was possible to visualize fast timescale ring flips of amino acids that were not observed using crystallography [52, 53, 54]. Overall, surface disorder in NMR structures is more pronounced than in crystal structures, which could be because in NMR structures many of the residues are solvent-exposed while in the crystal structures, the surface consists of protein-protein contacts that are similar to the protein core contacts [55].

Some biomolecules are difficult to crystallize because they are highly soluble which is the reason that NMR is preferred for determining their structures. One example of soluble biomolecules that are difficult to crystallize are proteins called $\beta\gamma$-crystallins, which are structural proteins found in the human eye lens. Human $\beta\gamma$-crystallins are hypothesized to have evolved from the *Ciona intestinalis* tunicate. In the tunicates, the $\beta\gamma$-crystallins bind Ca^{2+} unlike in the human eye lens and it is therefore essential to study the structural difference between the crystallins in tunicate and in vertebrates in order to develop more productive hypotheses as to how and why vertebrate $\beta\gamma$-crystallins evolved to lose their Ca^{2+} binding ability. There is a crystal structure of the tunicate $\beta\gamma$-crystallin in the Ca^{2+}-bound form; however, usable crystals were not obtained for the apo form, making comparison studies difficult. We set out to solve its apo and holo form structures in order to compare these structures with the human γS-crystallin structure, which was also solved via solution-state NMR by Brubaker, et al [21].

NMR structure determination for proteins larger than about 80 amino acids requires the collection of multidimensional spectra in order to resolve resonance overlap. 3D assignment experiments are acquired for the backbone and the amino acid side-chain resonances, where

each cross peak is labeled by three frequencies (^{15}N, ^{13}C and ^{1}H) [56]. For these experiments, proteins are isotopically labeled with ^{15}N and ^{13}C to enhance both signal to noise ratios and to obtain correlations among coupled nuclei. After the backbone and side-chain assignments are complete, distance restraints such as NOEs and residual dipolar couplings are used to calculate the NMR structure. Lastly, multiple rounds of data collection and structure calculations are required in order to obtain a final ensemble of high-resolution structures. The final structure consists of a superposition of a group of conformers that are obtained either relative to a predetermined conformer or by taking the mean of the atomic coordinates of structures calculated with different initial conditions [55].

3.2 Materials and Methods

3.2.1 Sample preparation

^{13}C/^{15}N isotopically labeled tunicate crystallin was expressed in minimal media. Briefly, 50 mL of overnight *E. coli* culture containing the plasmid with *Ci*-$\beta\gamma$-crystallin gene was transferred to 1 L LB media and grown to an OD_{550} of 1. The cultures were spun down and resuspended in 1 L of M9 minimal media with $^{15}NH_4Cl$ and ^{13}C-glucose. Afterwards, the cells were grown for two hours at 37 °C and induced with IPTG to a final concentration of 1 mM. The cells were then grown for an additional 20-25 hours at 25 °C and purified as stated in chapter 1.

^{15}N isotopically labeled WT-human γS-crystallin was expressed and purified as stated in chapter 1 and in Brubaker et al. [21].

3.2.2 NMR experiments

Experiments were performed at 25 °C on a Varian ^{Unity}INOVA system operating at 800 MHz equipped with a $^{1}H/^{13}C/^{15}N$ 5 mm tri-axis PFG triple-resonance probe. ^{15}N-^{1}H HSQC experiments were acquired with 4 scans in the direct dimension and 64 scans in the indirect dimension at protein concentrations of 1.7 mM in the presence of 10 mM EDTA or 10 mM $CaCl_2$. The rest of the parameters for the NMR experiments are detailed below.

3.2.3 Data processing

All data were first processed in NMRPipe and Sparky and assignments were performed in CcpNMR.

3.3 Results and Discussion

Examination of the crystal structure of the holo form (PDBID 2BV2) [3] reveals that negatively charged residues such as glutamic and aspartic acids participate in binding the divalent metal ions, along with serine. Specifically, Glu 7, Ile 33, Ser 35 and Asp 75 make up one of the two Ca^{2+} binding sites and Asp 32, Asp 48, Glu 76 and Ser 78 make up the other [3] (Figure 3.1). Although CD and fluorescence do not indicate large changes in protein secondary structure, solution-state NMR data (chemical shifts measured via ^{15}N-^{1}H HSQC) do show peak shifts for backbone residues involved in binding Ca^{2+} upon addition of 10 mM $CaCl_2$, indicating more subtle, local conformational changes responsible for stabilizing the protein against denaturation. The HSQC spectra, showing backbone assignments of both the apo and holo forms of tunicate crystallin are overlaid in Figure 3.2a. The ^{1}H and ^{15}N chemical shifts for the apo and holo forms have been deposited in the BioMagRes Bank, un-

der accession numbers 26860 and 26861, respectively. Chemical shift perturbation weighted averages upon addition of Ca^{2+} were measured using the chemical shift perturbation equation: $\Delta\delta_{avg} = \sqrt{\frac{(\Delta\delta_N/5)^2+(\Delta\delta_H)^2}{2}}$. Chemical shift perturbations upon addition of Ca^{2+} are plotted in Figure 3.2b, with thresholds for large (> 0.2 ppm) and moderate (0.06 - 0.2 ppm) perturbations shown. Residues for which the shift was less than 0.06 ppm were classified as unperturbed. These perturbations are shown in the context of the structure in Figure 3.2c. Examination of these data in the context of the protein structure suggest that the slight change in the fluorescence spectra upon addition of Ca^{2+} (Figure 1.2b) may be caused by a change in the local environment of Trp 70. Similarly, in a previous study, several residues were perturbed in the NMR spectrum upon addition of Ca^{2+} to M-crystallin, another case where Ca^{2+}-binding stabilized the protein [13]. In contrast, when Ca^{2+} was added to WT human γS-crystallin, no significant peak shifts were observed (Figure A.6), consistent with the lack of Ca^{2+} binding suggested by the ITC data.

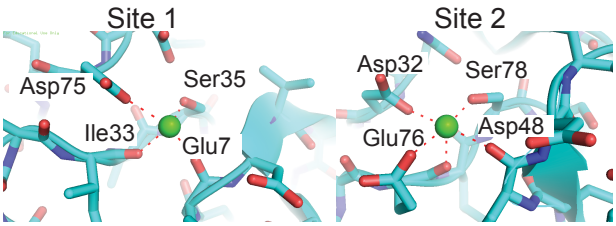

Figure 3.1: Residues involved in the calcium binding sites of the tunicate $\beta\gamma$-crystallin, observed in the X-ray crystal structure PDBID 2BV2 [3].

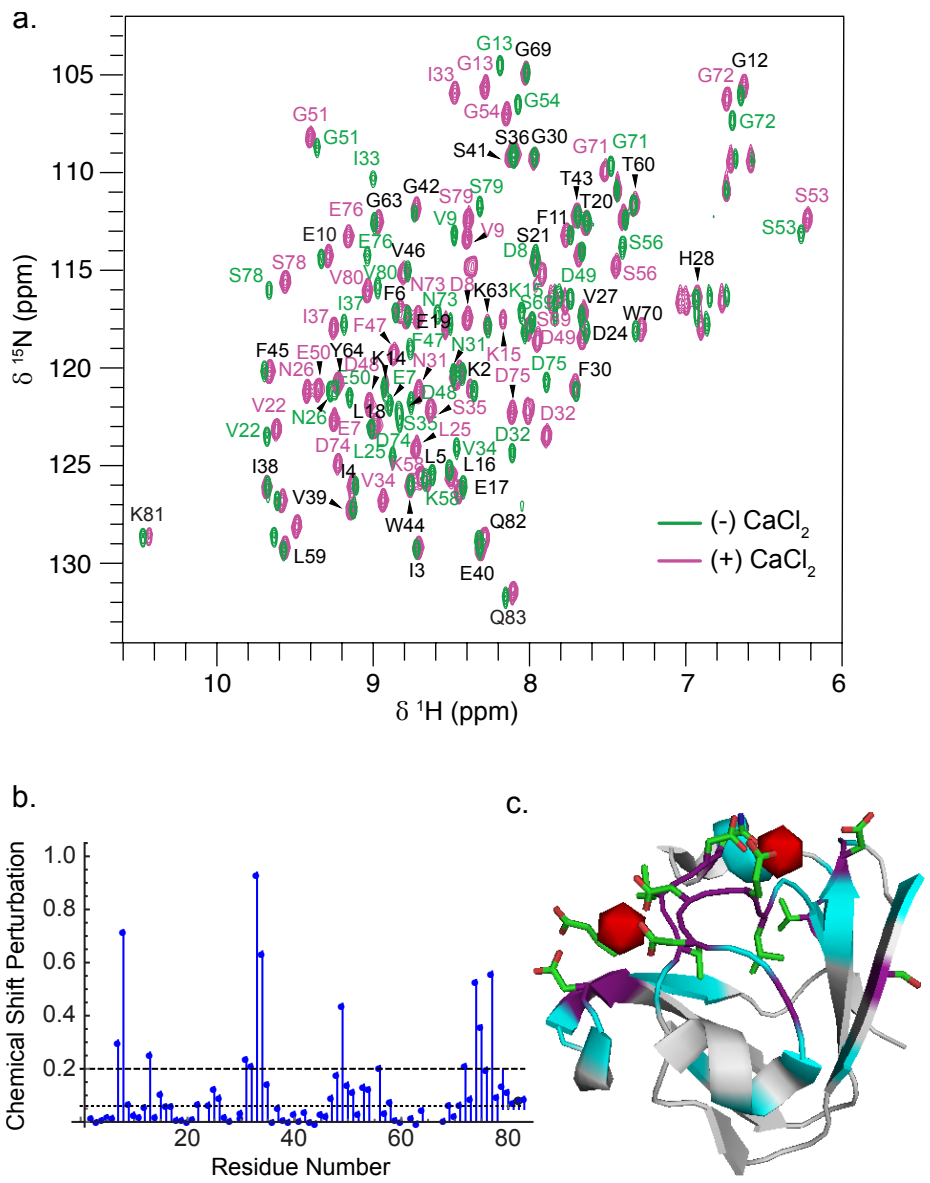

Figure 3.2: a. ^{15}N-^{1}H HSQC spectra of the tunicate $\beta\gamma$-crystallin in the absence (green) and presence (magenta) of 10 mM $CaCl_2$. Residues that have the same chemical shift under both conditions are labeled in black. b. Average chemical shift perturbation plot as a function of residue number, with thresholds for large ($>$ 0.2 ppm) and moderate (0.06-0.2 ppm). Residues for which the shift is $<$ 0.06 ppm upon addition of $CaCl_2$ are classified as unperturbed. c. The same CSP data represented on the X-ray crystal structure. The backbone corresponding to amide NHs for which the chemical shift perturbation is large are shown in purple, while amides that are slightly perturbed are in cyan and those of unperturbed residues are shown in gray. The two calcium ions are represented in red, while the side chains of the Ca^{2+}-binding residues are highlighted in green.

Solution-state NMR experiments that were used in making tunicate crystallin assignments are described in more detail below. The first step consisted of acquiring a series of triple resonance experiments that were used in assigning the backbone resonances as seen in the HSQC spectra in Figure 3.2a. Afterwards, sidechains were assigned using a similar type of approach to the backbone residues, with the acquisition of 3D experiments. Lastly, short range and long range distance restraints were measured using 3D NOE and residual dipolar coupling experiments. As an additional parameter, inter- and intramolecular hydrogen bonds were also determined using amide proton temperature coefficients from ^{15}N-^{1}H HSQC spectra.

3.4 Backbone Resonance Assignments

3.4.1 HNCO

The HNCO experiment is an out and back experiment that transfers magnetization from the amide proton through the amide nitrogen of the i residue to the carbonyl of the i-1 (previous) residue (Figure 3.3) [57, 56]. As a result, it is used in assigning the CO of the i-1 residue.

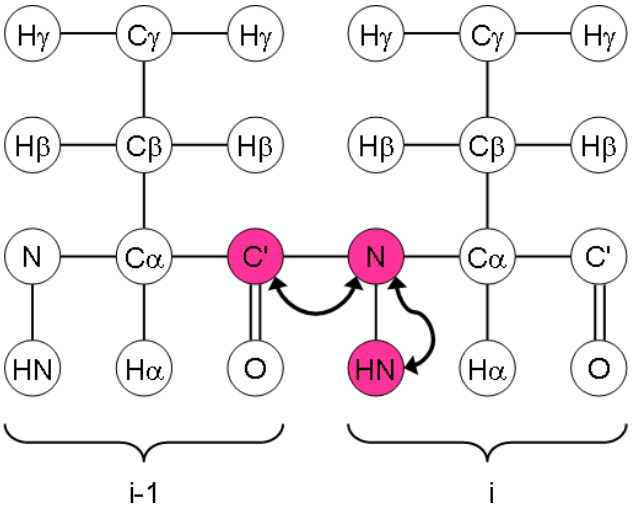

Figure 3.3: The transfer of magnetization in HNCO [58].

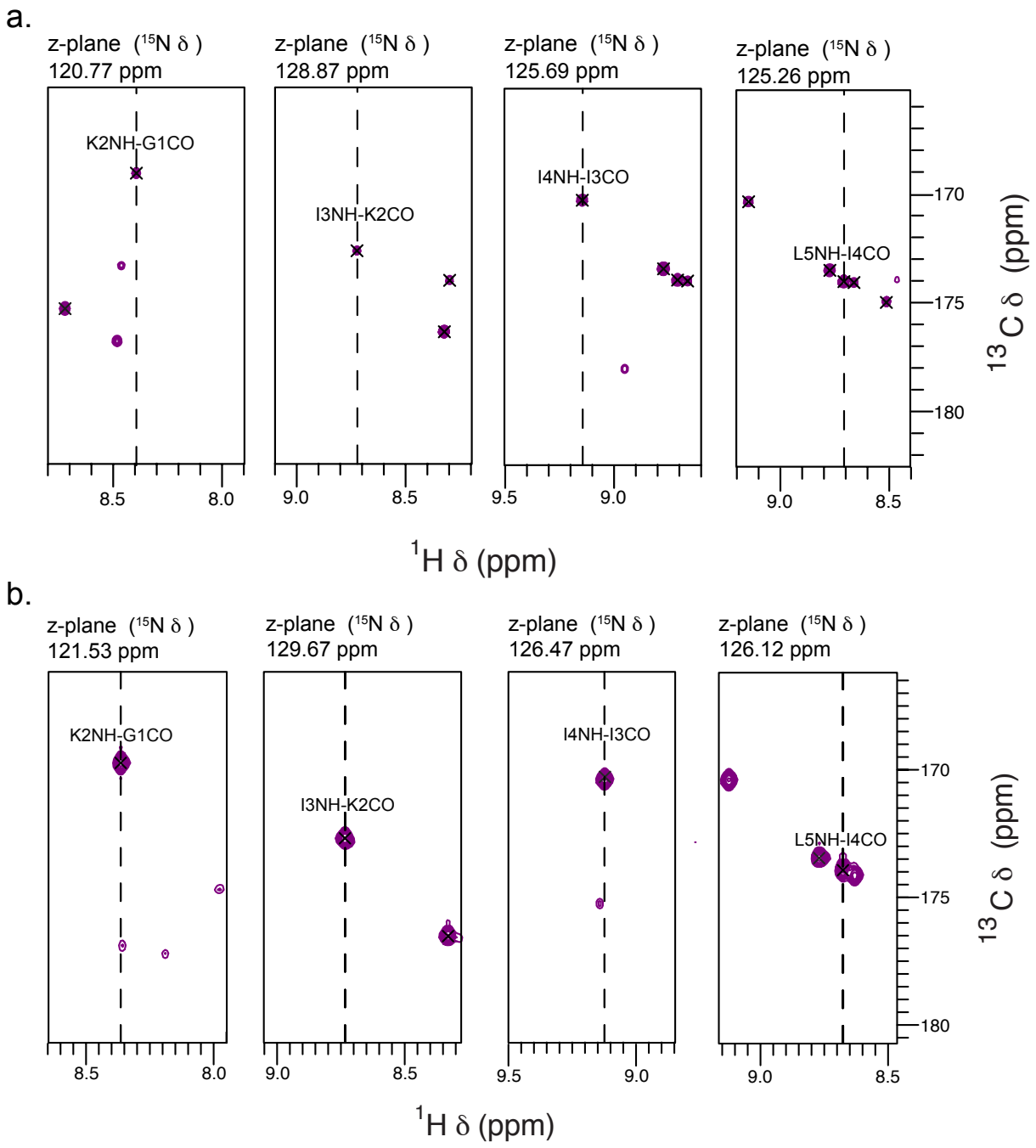

Figure 3.4: Four zoomed in planes of HNCO spectra showing sequential $(CO)_{i-1}$ residue assignments of tunicate crystallin in the presence of Ca^{2+} (a) or EDTA (b).

Table 3.1: HNCO NMR parameters of tunicate crystallin with 10 mM Ca^{2+}

	1H	13C	15N
SW (Hz)	12999.68	4000.00	3600.04
Number of scans	4		
Number of points	2218	64	48
Transmitter offset (ppm)	-306.86		
90 time (μs)	8.60	13.25	43.00
Decoupling power	60	41	48
Center frequency (ppm)	4.79	174.03	118.78

Table 3.2: HNCO NMR parameters of tunicate crystallin with 10 mM EDTA

	1H	13C	15N
SW (Hz)	12999.68	4000.00	3600.04
Number of scans	4		
Number of points	2048	48	36
Transmitter offset (ppm)	-305.00		
90 time (μs)	10.00	12.40	45.50
Decoupling power	60	41	48
Center frequency (ppm)	4.79	174.26	120.18

3.4.2 HN(CO)CA

Unlike the HNCO experiment, the HN(CO)CA experiment connects the amide proton of the i residue to the C_α of the i-1 residue through the magnetization transfer of the carbonyl of this preceding amino acid (i-1) [59].

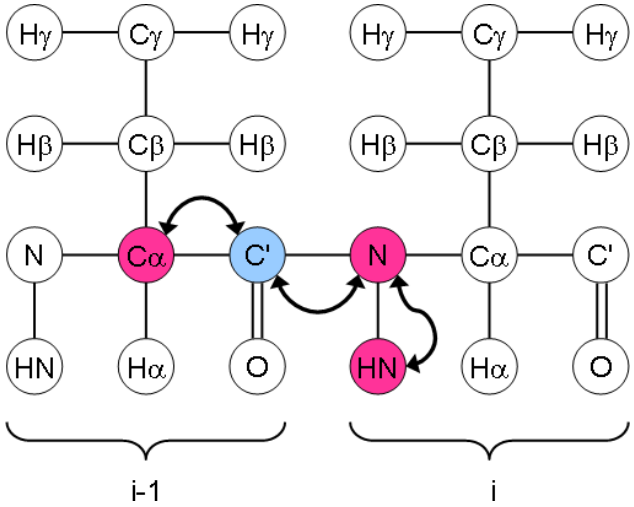

Figure 3.5: The transfer of magnetization in HN(CO)CA [58].

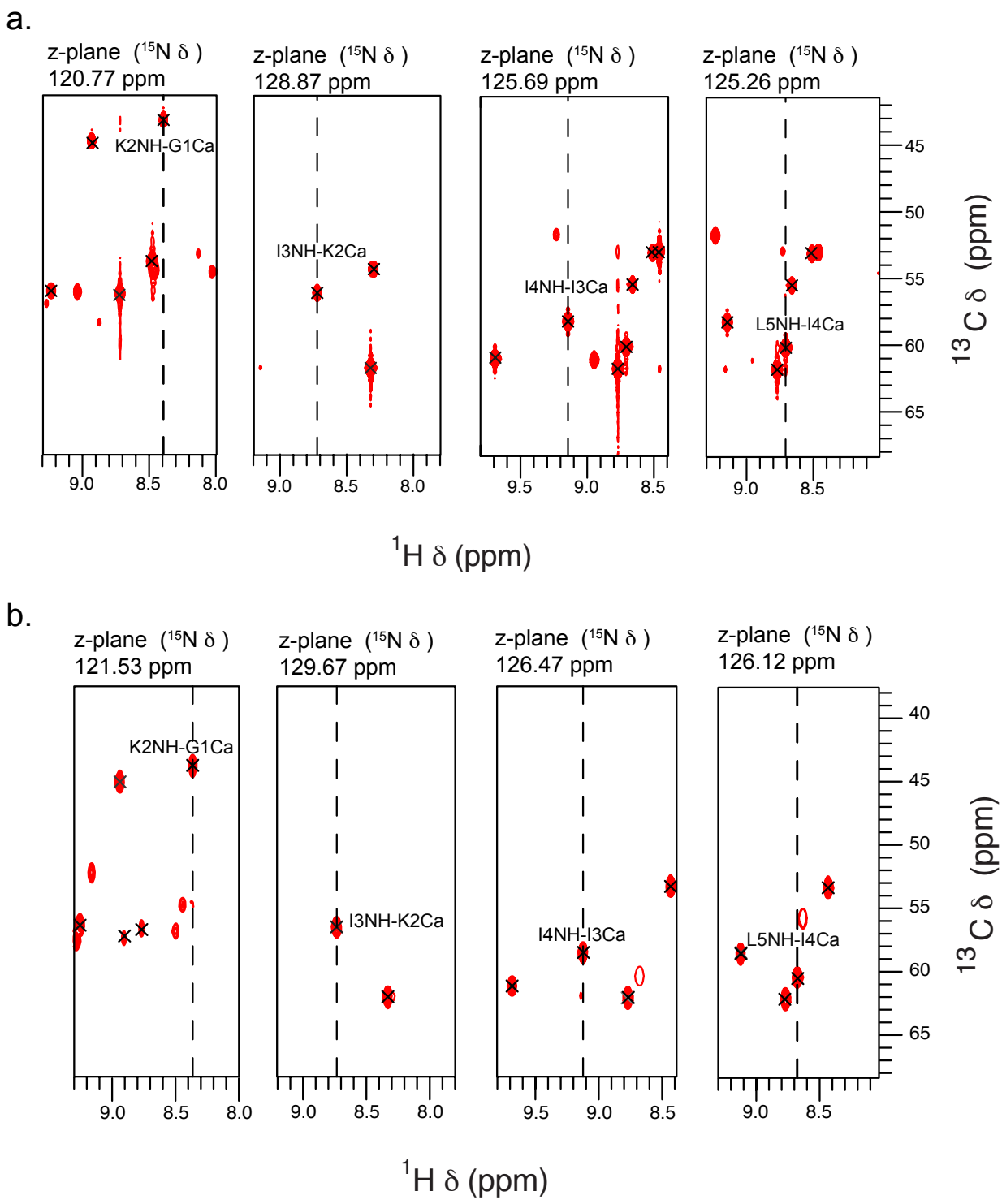

Figure 3.6: Four zoomed in planes of HN(CO)CA spectra showing sequential $(Ca)_{i-1}$ residue assignments of tunicate crystallin in the presence of Ca^{2+} (a) or EDTA (b).

Table 3.3: HN(CO)CA NMR parameters of tunicate crystallin with 10 mM Ca^{2+}

	1H	13C	15N
SW (Hz)	12019.23	6033.64	3600.04
Number of scans	4		
Number of points	2048	48	36
Transmitter offset (ppm)	-310.80		
90 time (μs)	8.70	13.00	42.00
Decoupling power	60	41	48
Center frequency (ppm)	4.79	56.05	118.79

Table 3.4: HN(CO)CA NMR parameters of tunicate crystallin with 10 mM EDTA

	1H	13C	15N
SW (Hz)	12999.68	10055.41	3600.04
Number of scans	4		
Number of points	2048	48	36
Transmitter offset (ppm)	-305.00		
90 time (μs)	10.00	12.40	45.50
Decoupling power	60	41	48
Center frequency (ppm)	4.79	56.15	120.18

3.4.3 HNCA

The HNCA experiment is similar to the HNCO experiment as the magnetization is transferred from the amide proton through the amide nitrogen of the i residue but it allows for detection of C_αs of the i and the i-1 residues via coherence transfer of the ${}^2J_{N-C_\alpha}$ [57]. Since the coupling of the directly bonded C_α of the i residue will be larger, this peak will have a stronger intensity.

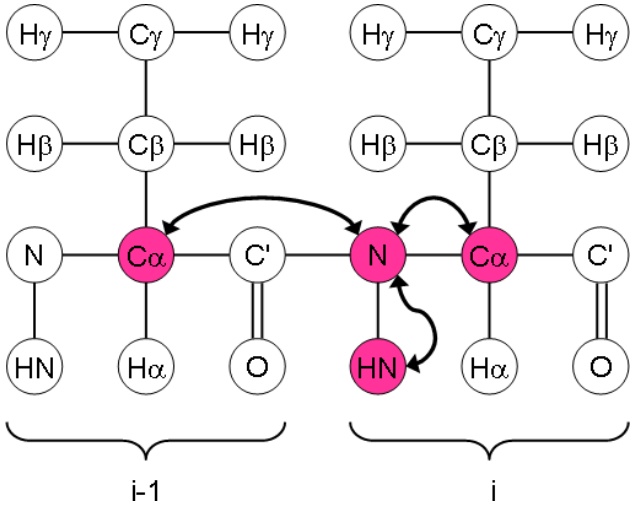

Figure 3.7: The transfer of magnetization in HNCA [58].

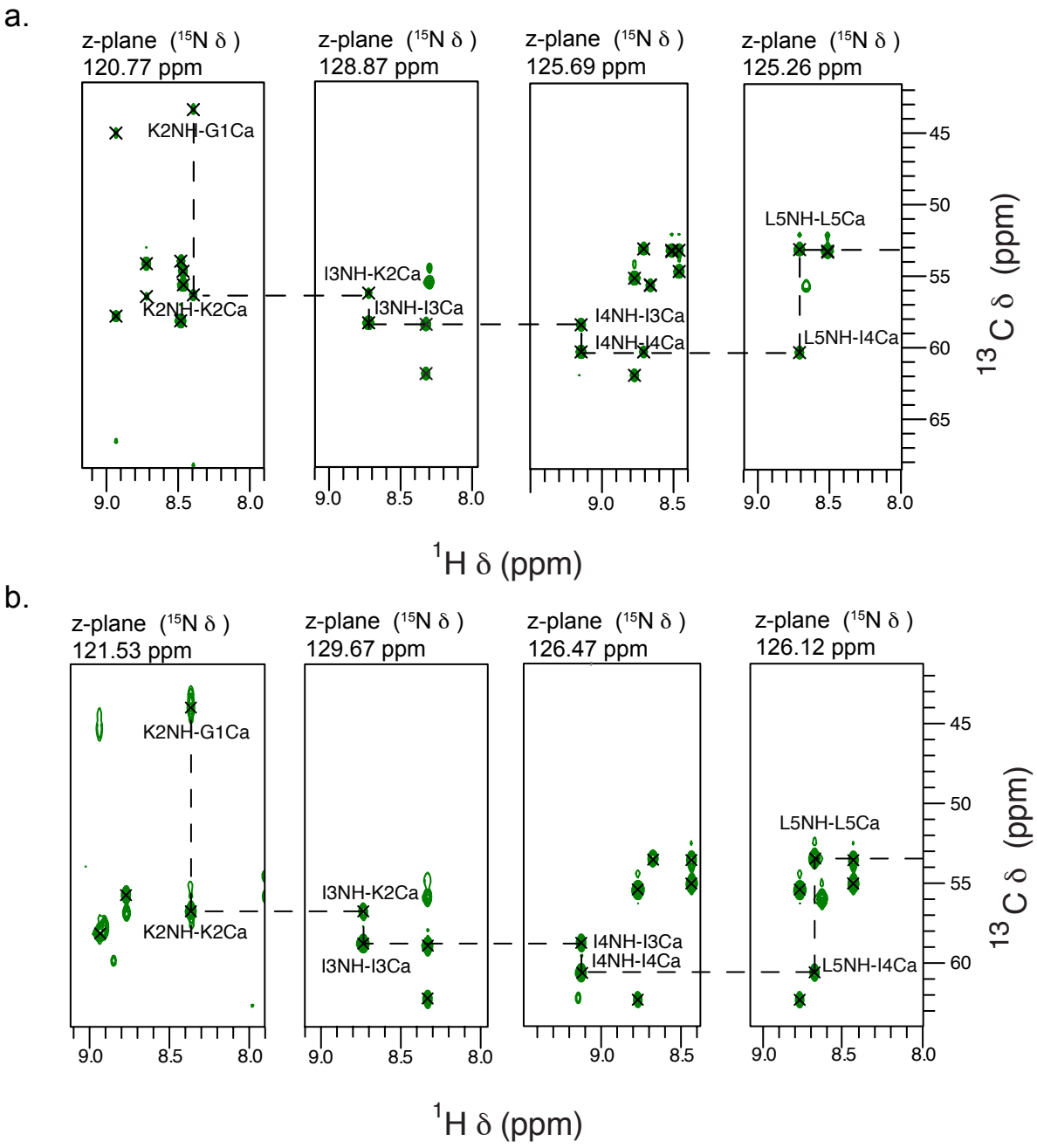

Figure 3.8: Four zoomed in planes of HNCA spectra showing sequential $(Ca)_i$ and $(Ca)_{i-1}$ residue assignments of tunicate crystallin in the presence of Ca^{2+} (a) or EDTA (b).

Table 3.5: HNCA NMR parameters of tunicate crystallin with 10 mM Ca^{2+}

	1H	13C	15N
SW (Hz)	12019.23	6033.64	2500.00
Number of scans	4		
Number of points	2048	64	48
Transmitter offset (ppm)	-306.90		
90 time (μs)	8.60	14.00	43.00
Decoupling power	60	41	48
Center frequency (ppm)	4.79	56.04	118.78

Table 3.6: HNCA NMR parameters of tunicate crystallin with 10 mM EDTA

	1H	13C	15N
SW (Hz)	12999.68	6034.29	3600.04
Number of scans	4		
Number of points	2048	48	36
Transmitter offset (ppm)	-305.00		
90 time (μs)	10.00	12.30	45.50
Decoupling power	60	41	48
Center frequency (ppm)	4.79	56.27	120.18

3.4.4 HN(CA)CO

Unlike the HNCA experiment, in this experiment the magnetization is transferred via the amide nitrogen to the C_α spins using the ${}^2J_{N-C_\alpha}$ couplings, and finally to the carbonyls of the i and the i-1 residues. Again as with the HNCA experiment, the peak intensity will be stronger of i carbonyl because the J_{N-C_α} coupling of the i residue will be higher than that to the i-1 residue [60].

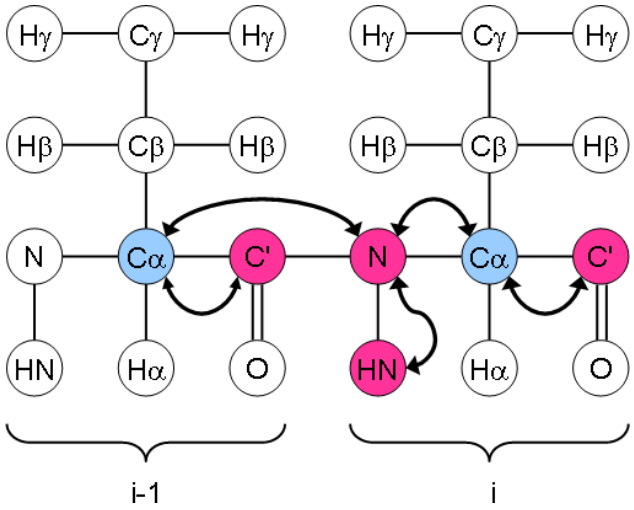

Figure 3.9: The transfer of magnetization in HN(CA)CO [58].

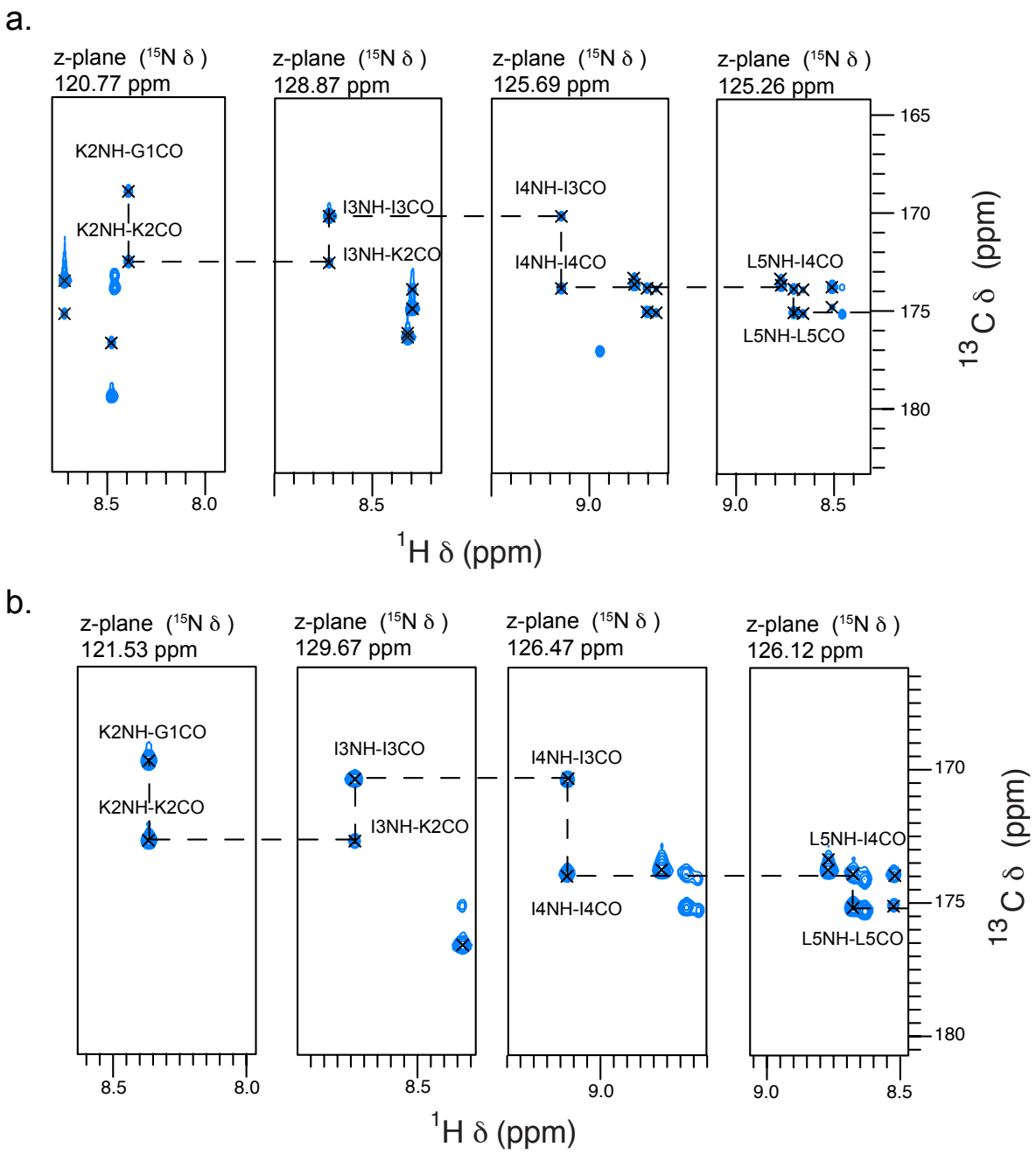

Figure 3.10: Four zoomed in planes of HN(CA)CO spectra showing sequential $(CO)_i$ and $(CO)_{i-1}$ residue assignments of tunicate crystallin in the presence of Ca^{2+} (a) or EDTA (b).

Table 3.7: HN(CA)CO NMR parameters of tunicate crystallin with 10 mM Ca^{2+}

	1H	13C	15N
SW (Hz)	12019.23	4000.00	3600.04
Number of scans	4		
Number of points	2048	48	36
Transmitter offset (ppm)	-310.76		
90 time (μs)	8.70	13.00	42.00
Decoupling power	60	41	48
Center frequency (ppm)	4.79	56.05	118.79

Table 3.8: HN(CA)CO NMR parameters of tunicate crystallin with 10 mM EDTA

	1H	13C	15N
SW (Hz)	12999.68	4000.00	3600.04
Number of scans	4		
Number of points	2048	48	36
Transmitter offset (ppm)	-305.00		
90 time (μs)	10.00	12.40	45.50
Decoupling power	60	41	48
Center frequency (ppm)	4.79	56.15	120.18

3.4.5 CBCA(CO)NH

The CBCA(CO)NH correlates the amide proton chemical shifts of the i residue with the C_α and the C_β of the i-1 residues. Magnetization is first transferred from the H_α and the H_β to the C_α and the C_β of the i-1 residue and finally transferred via the carbonyl of the i residue to the amide of the i residue for detection [61].

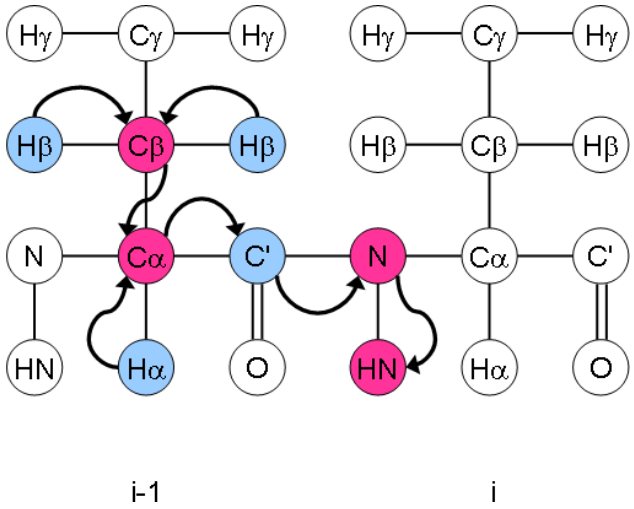

Figure 3.11: The transfer of magnetization in CBCA(CO)NH [58].

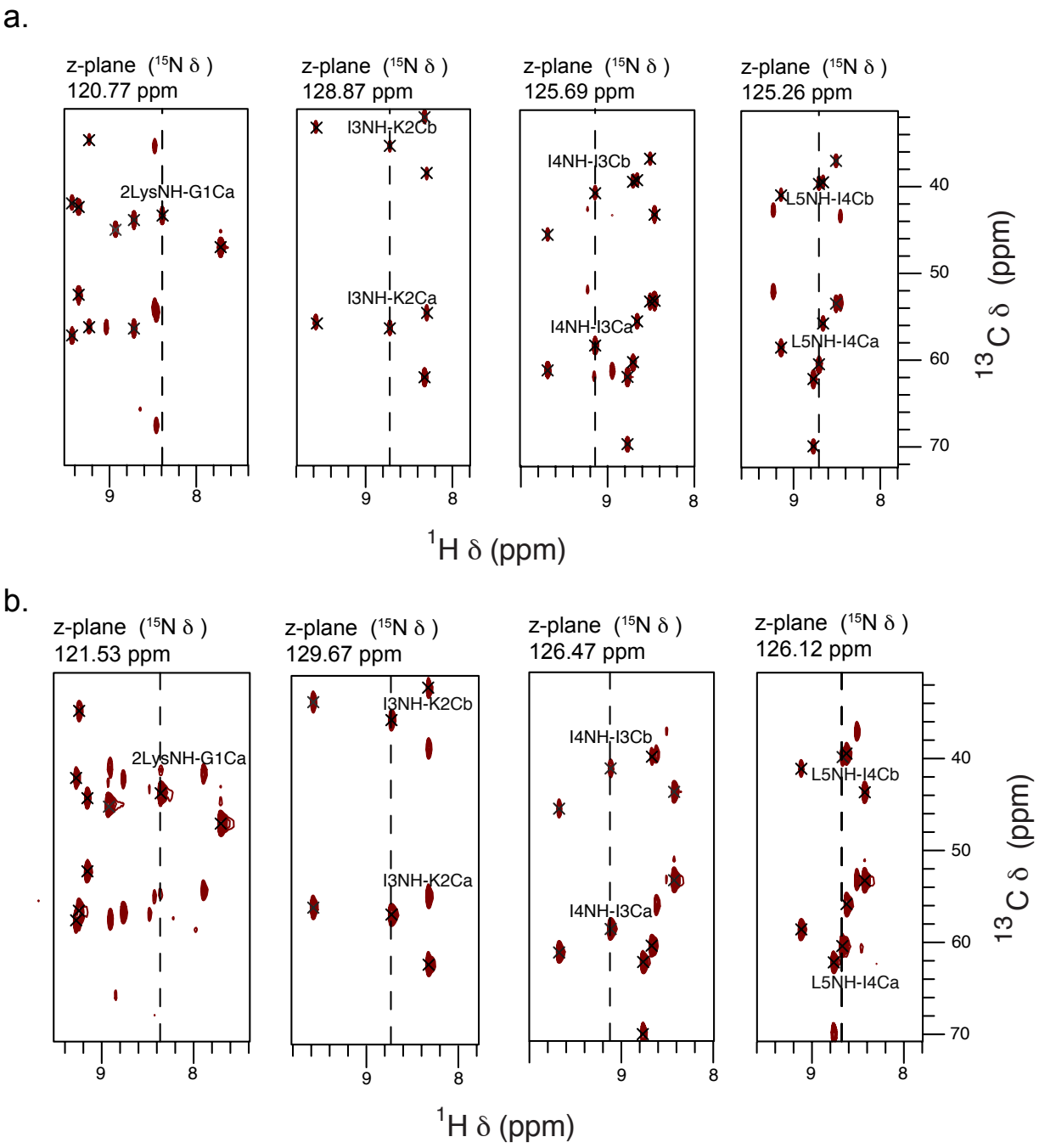

Figure 3.12: Four zoomed in planes of CBCA(CO)NH spectra showing sequential $(Ca)_{i-1}$ and $(Cb)_{i-1}$ residue assignments of tunicate crystallin in the presence of Ca^{2+} (a) or EDTA (b).

Table 3.9: CBCA(CO)NH NMR parameters of tunicate crystallin with 10 mM Ca^{2+}

	1H	13C	15N
SW (Hz)	12019.23	16000.00	3600.04
Number of scans	4		
Number of points	2048	64	36
Transmitter offset (ppm)	-304.90		
90 time (μs)	8.70	13.30	42.00
Decoupling power	60	41	48
Center frequency (ppm)	4.79	46.03	118.79

Table 3.10: CBCA(CO)NH NMR parameters of tunicate crystallin with 10 mM EDTA

	1H	13C	15N
SW (Hz)	12999.68	16000.00	3600.04
Number of scans	4		
Number of points	2048	48	36
Transmitter offset (ppm)	-305.00		
90 time (μs)	10.10	12.40	45.50
Decoupling power	60	41	48
Center frequency (ppm)	4.79	46.16	120.18

3.4.6 HNCACB

Unlike in the CBCA(CO)NH experiment, the magnetization in this experiment is transferred from the H_α and the H_β to the C_α and the C_β of the i-1 residue and the i residue directly to the amide nitrogen and the amide proton of the i residue for detection [62].

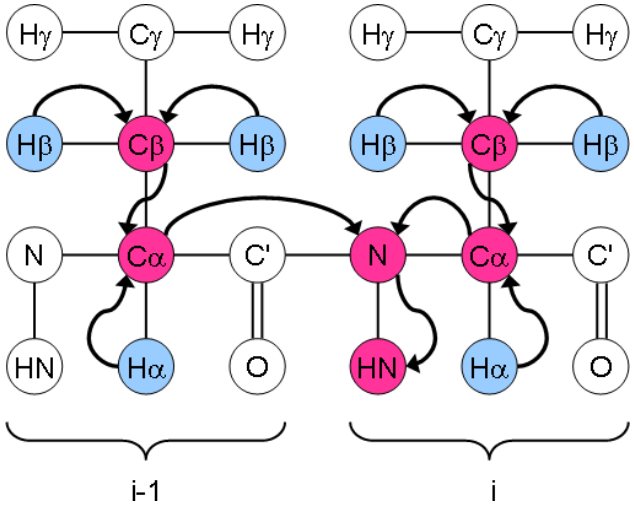

Figure 3.13: The transfer of magnetization in HNCACB [58].

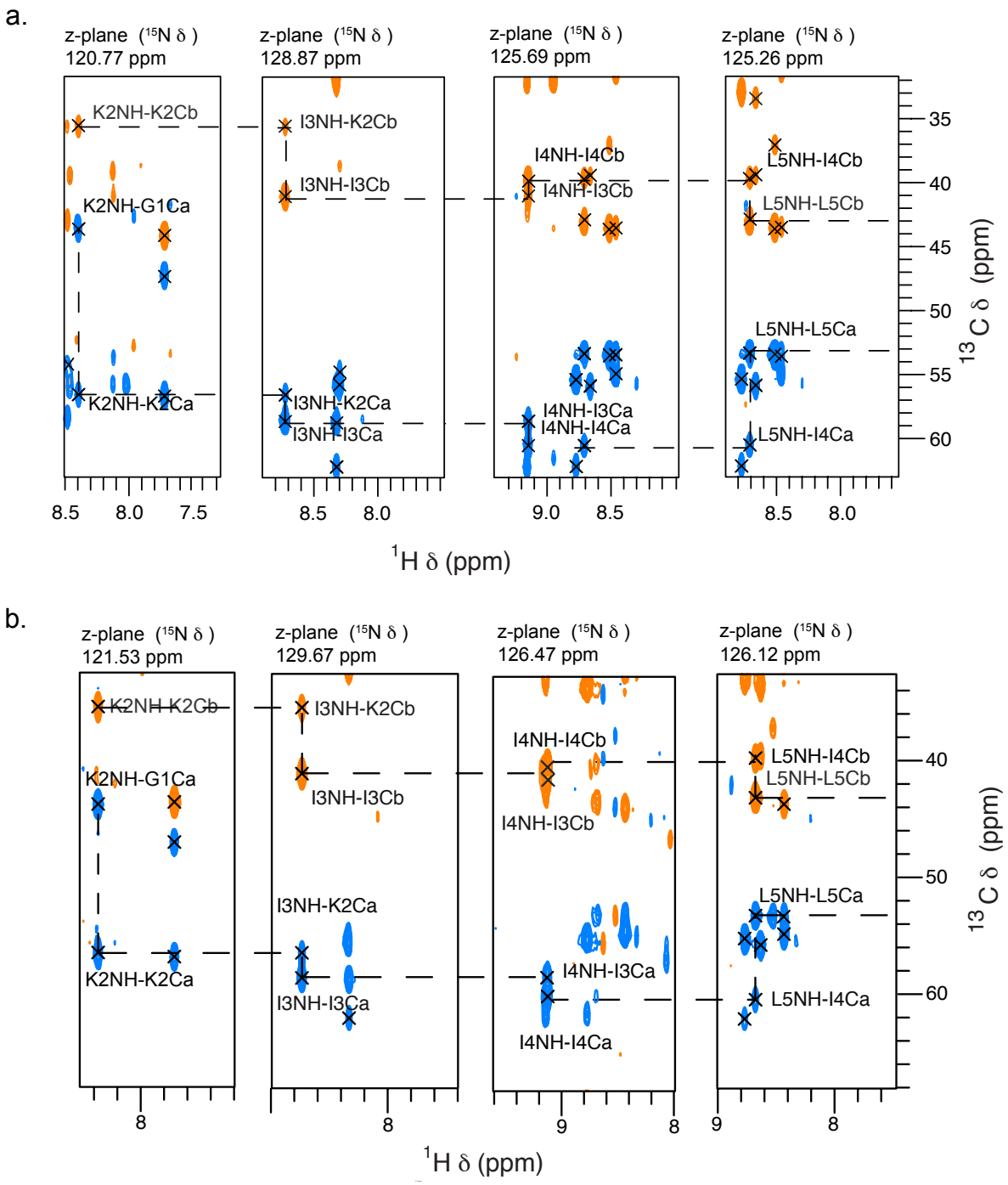

Figure 3.14: Four zoomed in planes of HNCACB spectra showing sequential $(Ca)_i$, $(Ca)_{i-1}$, $(Cb)_i$ and $(Cb)_{i-1}$ residue assignments of tunicate crystallin in the presence of Ca^{2+} (a) or EDTA (b).

Table 3.11: HNCACB NMR parameters of tunicate crystallin with 10 mM Ca^{2+}

	1H	13C	15N
SW (Hz)	12019.23	16000.00	3600.04
Number of scans	4		
Number of points	2048	64	36
Transmitter offset (ppm)	-304.90		
90 time (μs)	8.70	13.30	42.00
Decoupling power	60	41	48
Center frequency (ppm)	4.79	46.03	118.79

Table 3.12: HNCACB NMR parameters of tunicate crystallin with 10 mM EDTA

	1H	13C	15N
SW (Hz)	12999.68	16000.00	3600.04
Number of scans	4		
Number of points	2048	48	36
Transmitter offset (ppm)	-305.00		
90 time (μs)	10.00	12.40	45.50
Decoupling power	60	41	48
Center frequency (ppm)	4.79	46.15	120.18

3.5 Side-chain Resonance Assignments

3.5.1 CC(CO)NH

In this experiment, magnetization is transferred from the side chain protons to the side chain carbons of one residue followed by isotropic ^{13}C mixing time which transfers that magnetization between the carbons after which the magnetization is transferred to the carbonyl of the i-1 residue and the amide nitrogen and proton of the i residue for detection. With the help of the CC(CO)NH experiment, the carbon side chain resonances of one residue can be directly linked with the amides of the preceding residue [63].

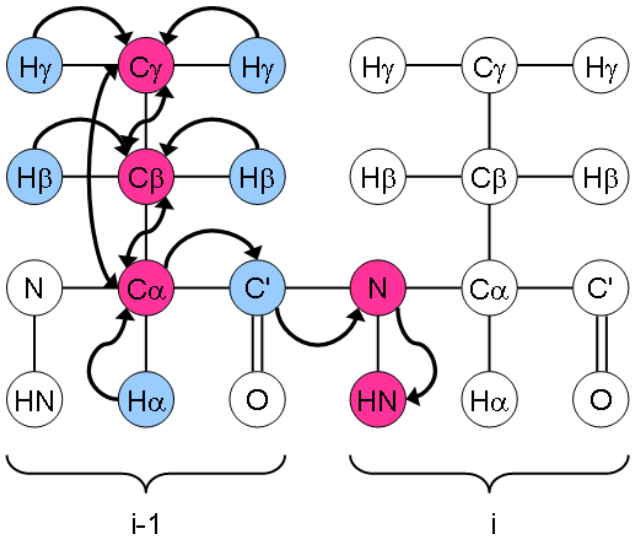

Figure 3.15: The transfer of magnetization in CC(CO)NH [58].

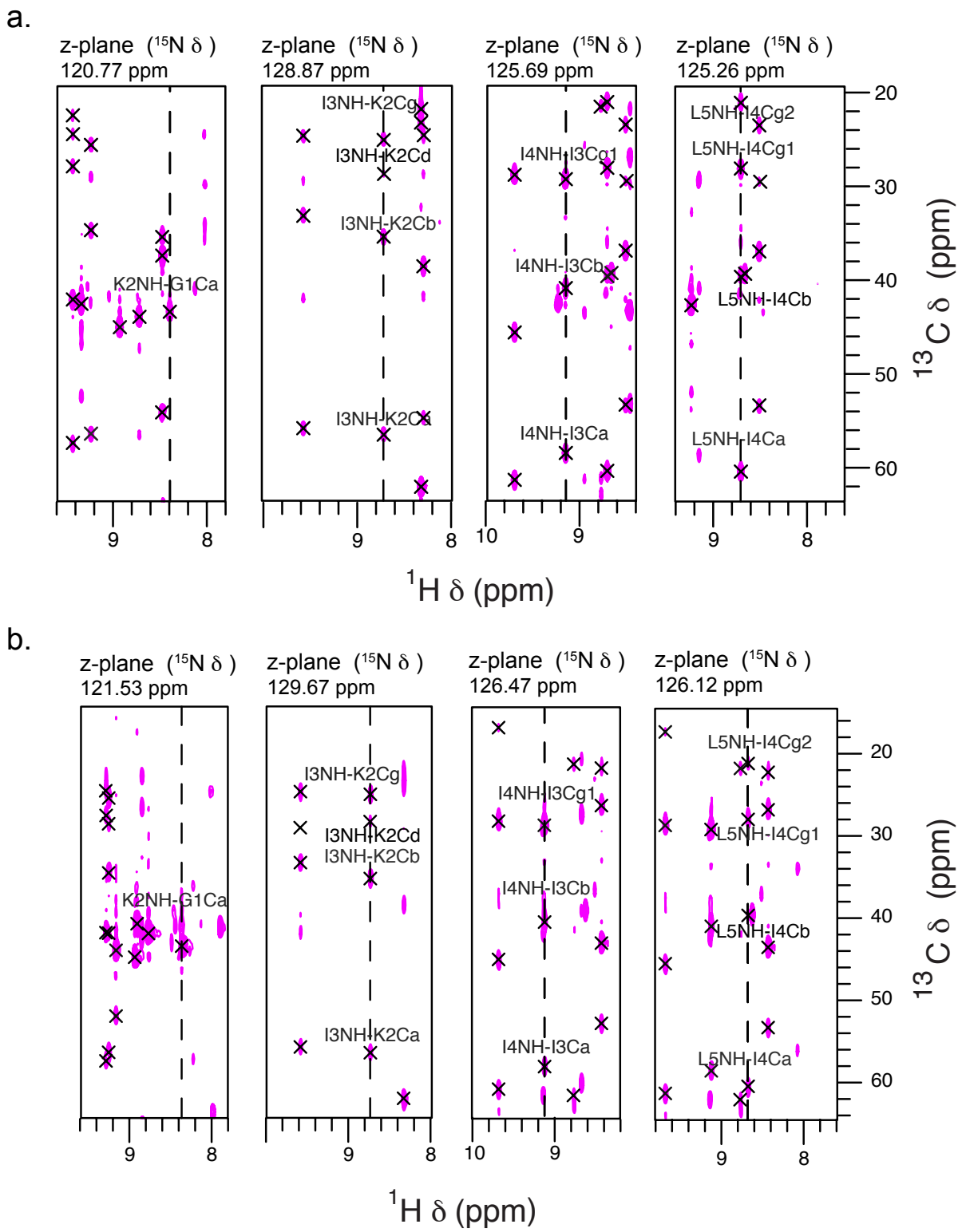

Figure 3.16: Four zoomed in planes of CC(CO)NH spectra showing carbon side chains of sequential i-1 residue assignments of tunicate crystallin in the presence of Ca^{2+} (a) or EDTA (b).

Table 3.13: CC(CO)NH NMR parameters of tunicate crystallin with 10 mM Ca^{2+}

	1H	13C	15N
SW (Hz)	12019.23	15022.78	3600.04
Number of scans	4		
Number of points	1894	64	48
Transmitter offset (ppm)	-305.00		
90 time (μs)	9.70	13.30	47.00
Decoupling power	60	41	48
Center frequency (ppm)	4.79	51.49	127.88

Table 3.14: CC(CO)NH NMR parameters of tunicate crystallin with 10 mM EDTA

	1H	13C	15N
SW (Hz)	12019.23	15022.78	3600.04
Number of scans	8		
Number of points	1894	40	25
Transmitter offset (ppm)	-296.50		
90 time (μs)	10.70	13.30	45.50
Decoupling power	60	41	48
Center frequency (ppm)	4.80	51.55	127.90

3.5.2 H(CCO)NH

The H(CCO)NH is pretty much identical to the CC(CO)NH experiment but directly links the proton side chain resonances of one residue with the amides of the preceding residue [63].

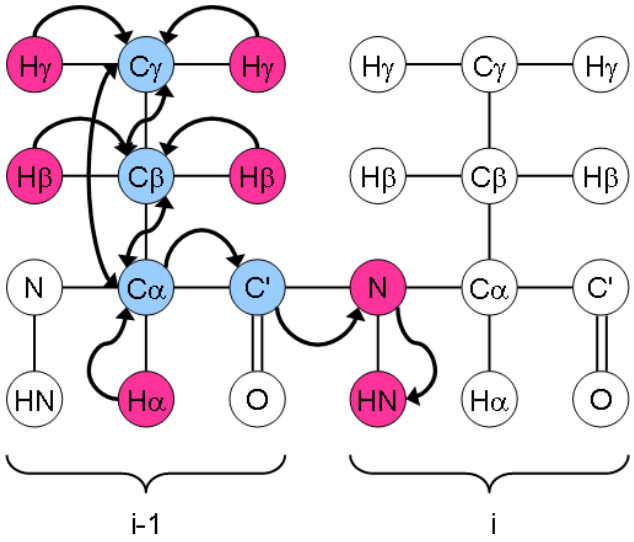

Figure 3.17: The transfer of magnetization in H(CCO)NH [58].

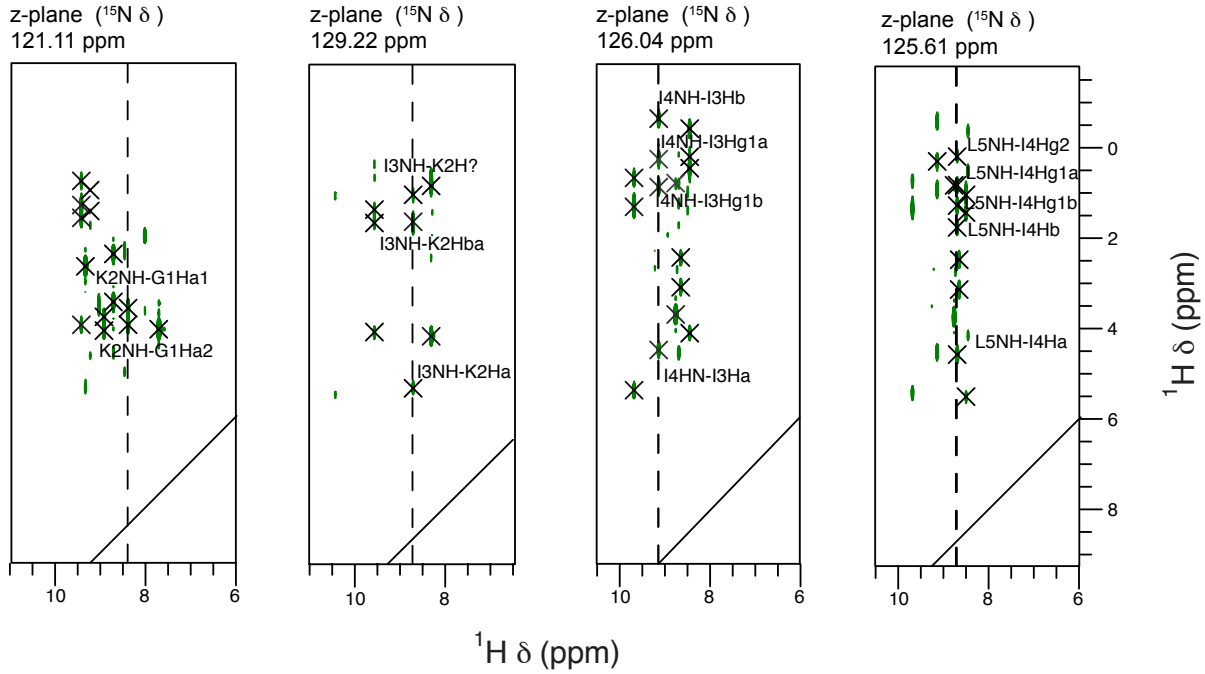

Figure 3.18: Four zoomed in planes of H(CCO)NH spectra showing proton side chains of sequential i-1 residue assignments of tunicate crystallin in the presence of Ca^{2+}.

Table 3.15: H(CCO)NH NMR parameters of tunicate crystallin with 10 mM Ca^{2+}

	1H	1H	15N
SW (Hz)	12019.23	12000.00	3600.04
Number of scans	8		
Number of points	1894	64	48
Transmitter offset (ppm)	-305.00		
90 time (μs)	9.70		47.00
Decoupling power	60		48
Center frequency (ppm)	4.79	4.79	127.81

3.5.3 HCCH-COSY

The HCCH-COSY experiment is used to assign the aliphatic ^{1}H and ^{13}C of the same residue. Some assignments are still ambiguous due to substantial peak overlap such as those for side-chain resonances of Lys and Arg. Magnetization is transferred from the side chain protons to the side chain carbons using the $^{1}J_{C-H}$-couplings followed by an exchange of that magnetization between the side chain carbons using the larger $^{1}J_{C-C}$-couplings. Finally, magnetization is transferred back to the side chain protons for detection [64, 65].

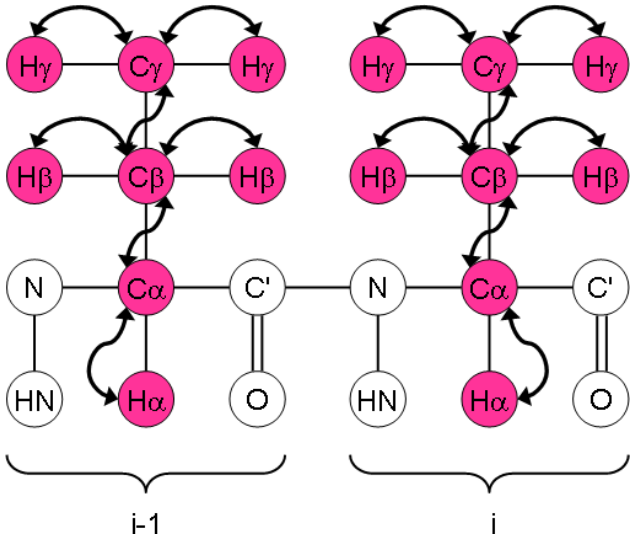

Figure 3.19: The transfer of magnetization in HCCH-COSY [58].

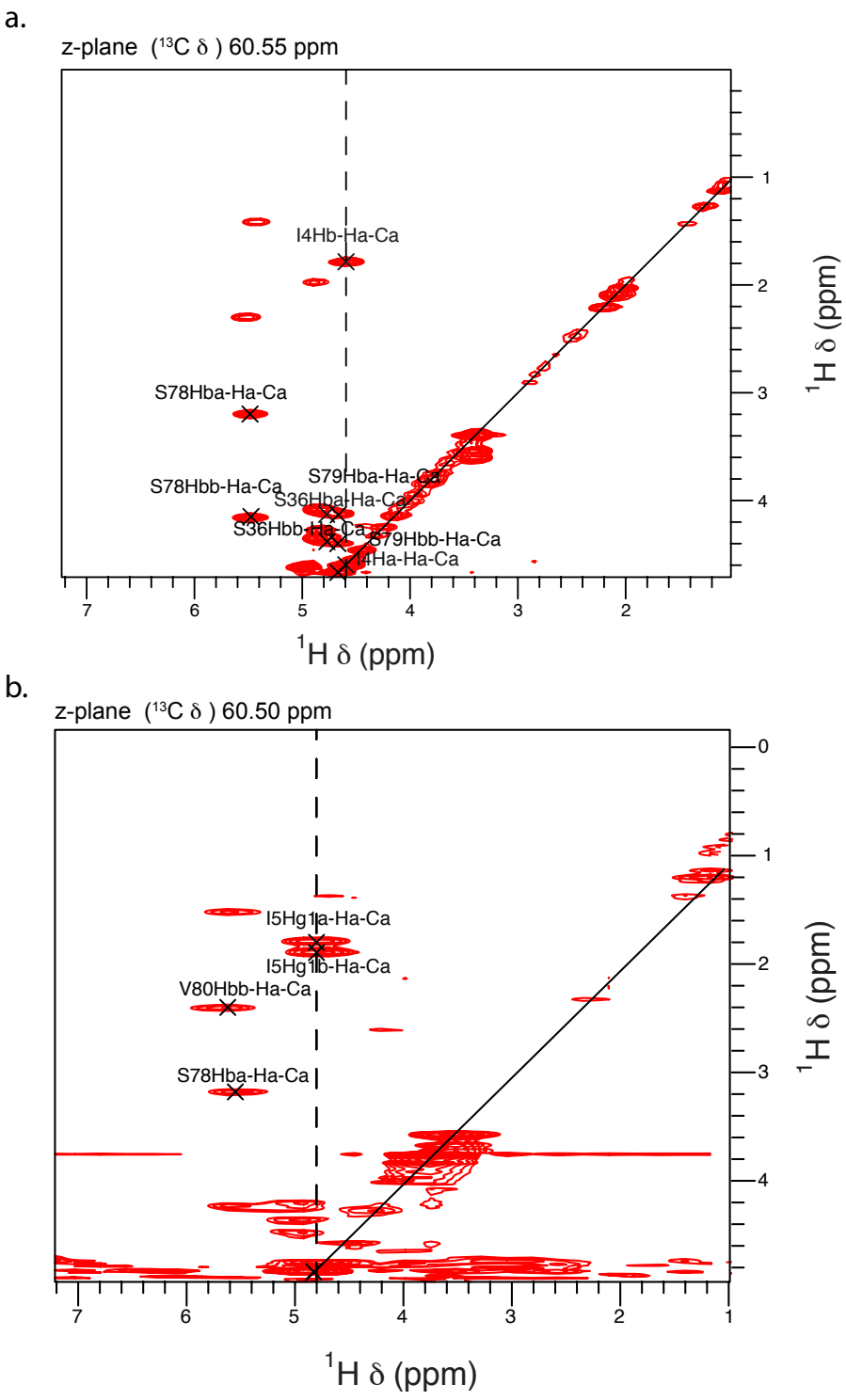

Figure 3.20: A ^{13}C plane of HCCH-COSY spectrum showing several proton and carbon side chains of the same residue in tunicate crystallin in the presence (a) and absence (b) of Ca^{2+}.

Table 3.16: HCCH-COSY NMR parameters of tunicate crystallin with 10 mM Ca^{2+}

	1H	1H	13C
SW (Hz)	12001.20	10000.00	16090.16
Number of scans	4		
Number of points	1024	64	48
Transmitter offset (ppm)	-304.90		
90 time (μs)	8.70		13.30
Decoupling power	60		41
Center frequency (ppm)	4.80	4.80	35.10

Table 3.17: HCCH-COSY NMR parameters of tunicate crystallin with 10 mM EDTA

	1H	1H	13C
SW (Hz)	12001.20	10000.00	16090.16
Number of scans	4		
Number of points	1024	64	48
Transmitter offset (ppm)	-304.90		
90 time (μs)	8.70		13.30
Decoupling power	60		41
Center frequency (ppm)	4.80	4.80	35.10

3.5.4 HCCH-TOCSY

This experiment is used in the assignment of the aliphatic ^{1}H and ^{13}C spin systems of sequentially assigned residues. Magnetization is transferred from the side chain protons to the side chain carbons of one residue and through isotropic ^{13}C mixing time, that magnetization is transferred between carbons similar to the CC(CO)NH and the H(CCO)NH experiments.

That magnetization is then transferred back to the side chain hydrogens for detection instead of the amide nitrogen and amide protons for detection [66]. This is why it is advisable to do this experiment in conjunction with the H(CCO)NH and the 15N-TOCSY-HSQC experiments in order to be able to link the side chain assignments with the backbone amides.

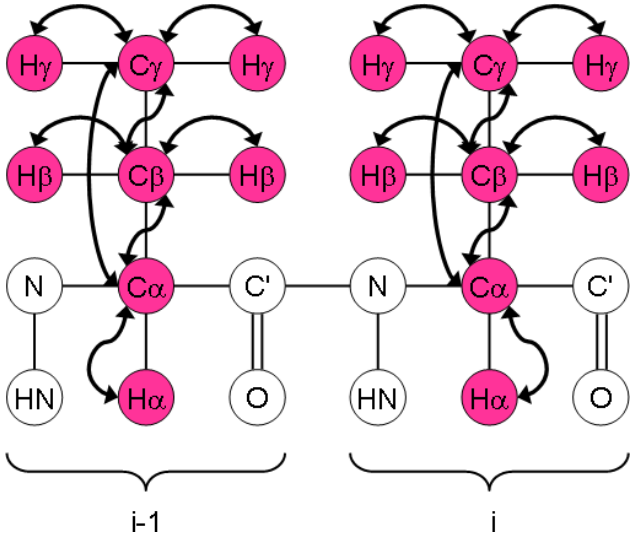

Figure 3.21: The transfer of magnetization in HCCH-TOCSY [58].

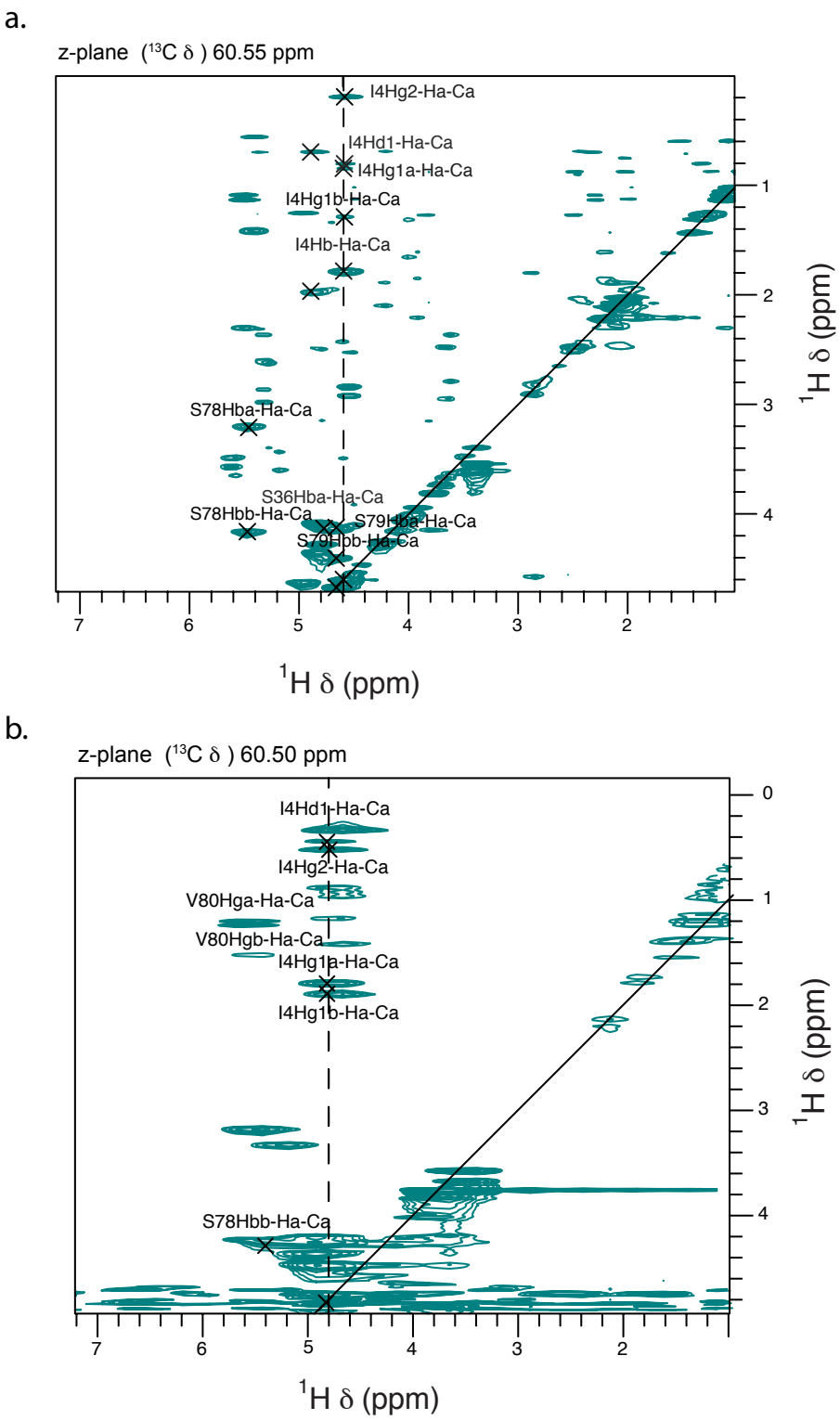

Figure 3.22: A ^{13}C plane of HCCH-TOCSY spectrum showing several proton and carbon side chains of the same spin system in tunicate crystallin in the presence (a) and absence (b) of Ca^{2+}.

Table 3.18: HCCH-TOCSY NMR parameters of tunicate crystallin with 10 mM Ca^{2+}

	1H	1H	13C
SW (Hz)	12999.68	12999.68	16090.11
Number of scans	8		
Number of points	2048	34	66
Transmitter offset (ppm)	-305.00		
90 time (μs)	10.00		12.40
Decoupling power	60		41
Center frequency (ppm)	4.79	4.79	35.14

Table 3.19: HCCH-TOCSY NMR parameters of tunicate crystallin with 10 mM EDTA

	1H	1H	13C
SW (Hz)	12999.68	12999.68	16090.11
Number of scans	8		
Number of points	2048	34	66
Transmitter offset (ppm)	-305.00		
90 time (μs)	10.00		12.40
Decoupling power	60		41
Center frequency (ppm)	4.79	4.79	35.14

3.5.5 ^{15}N-TOCSY-HSQC

The ^{15}N-TOCSY-HSQC experiment helps link side chain protons of the i residue with the amide backbone proton. This experiment works by transferring magnetization between the side-chain protons using an isotropic mixing step followed by transfer to the amide nitrogen and the amide proton for detection.

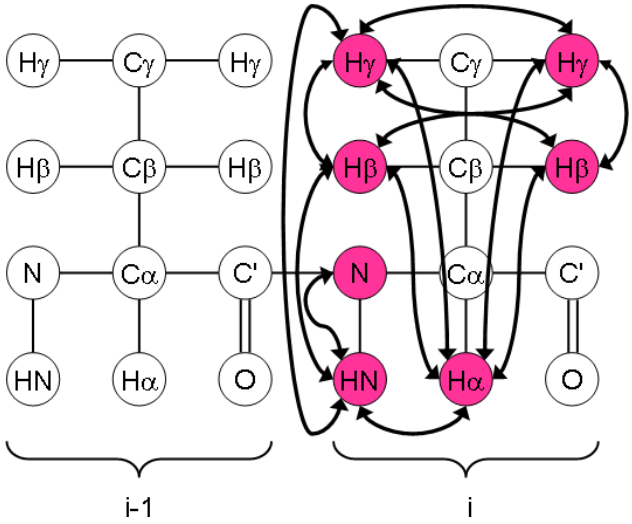

Figure 3.23: The transfer of magnetization in ^{15}N-TOCSY-HSQC [58].

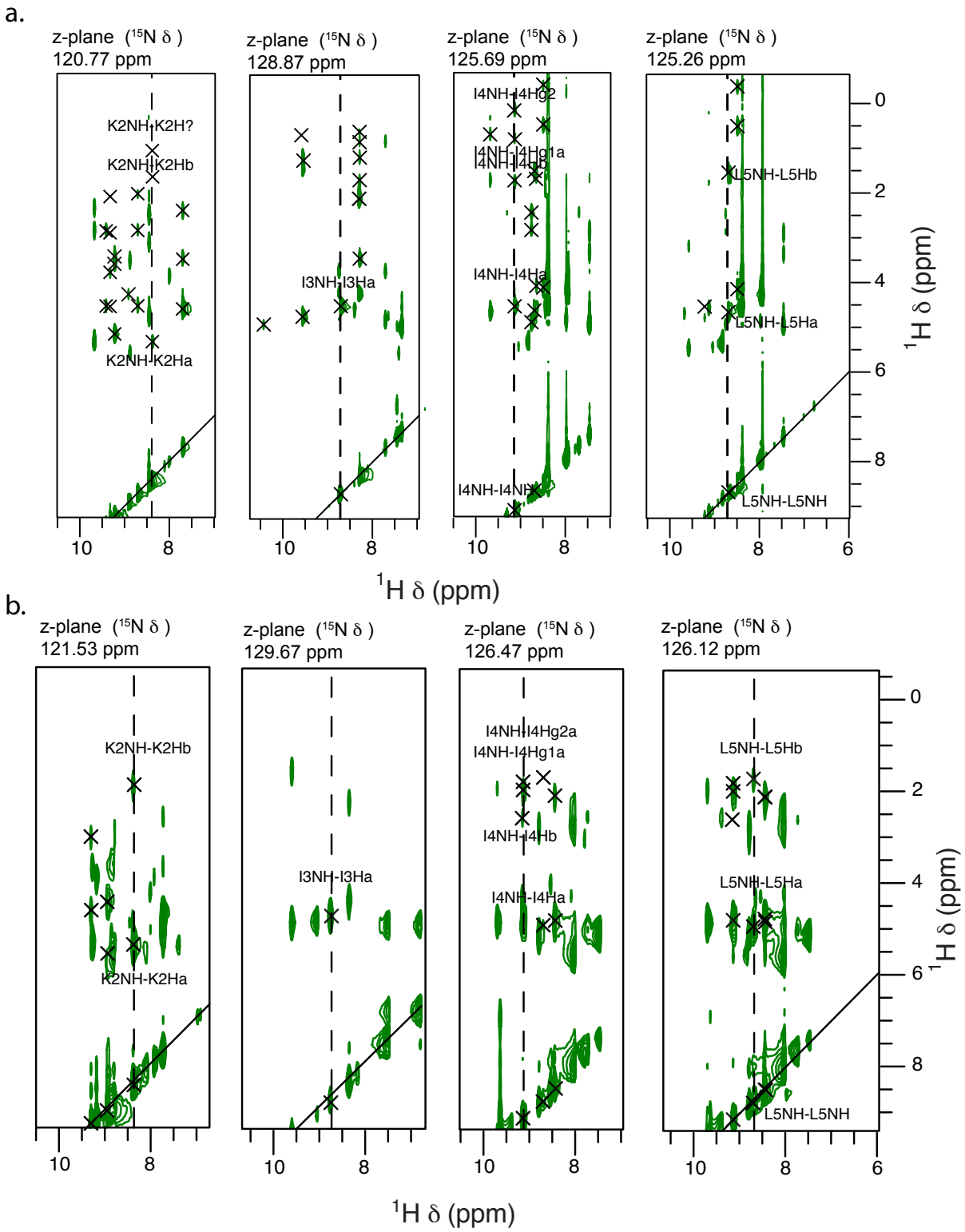

Figure 3.24: Four zoomed in planes of ^{15}N-TOCSY-HSQC spectra showing proton side chains of sequential i residue assignments of tunicate crystallin in the presence (a) and absence (b) of Ca^{2+}.

Table 3.20: ^{15}N-TOCSY-HSQC NMR parameters of tunicate crystallin with 10 mM Ca^{2+}

	1H	1H	15N
SW (Hz)	12999.68	12999.68	4100.04
Number of scans	8		
Number of points	2048	34	42
Transmitter offset (ppm)	-305.00		
90 time (μs)	9.68		47.00
Decoupling power	60		48
Center frequency (ppm)	4.79	4.79	120.26

Table 3.21: ^{15}N-TOCSY-HSQC NMR parameters of tunicate crystallin with 10 mM EDTA

	1H	1H	15N
SW (Hz)	14396.26	14393.67	4100.04
Number of scans	8		
Number of points	2268	34	42
Transmitter offset (ppm)	-305.00		
90 time (μs)	11.50		45.50
Decoupling power	60		48
Center frequency (ppm)	4.79	4.79	120.25

3.6 Distance Restraints

3.6.1 NOESY-^{15}N-HSQC

Both the NOESY-^{15}N-HSQC and the ^{13}C-NOESY HSQC experiment consists of a 2D NOESY experiment and a sensitivity enhanced HSQC experiment. Exchange of magnetization among all hydrogen occurs in this experiment using the NOE and then that magnetization is transferred to the amide nitrogen and the amide proton for detection [67].

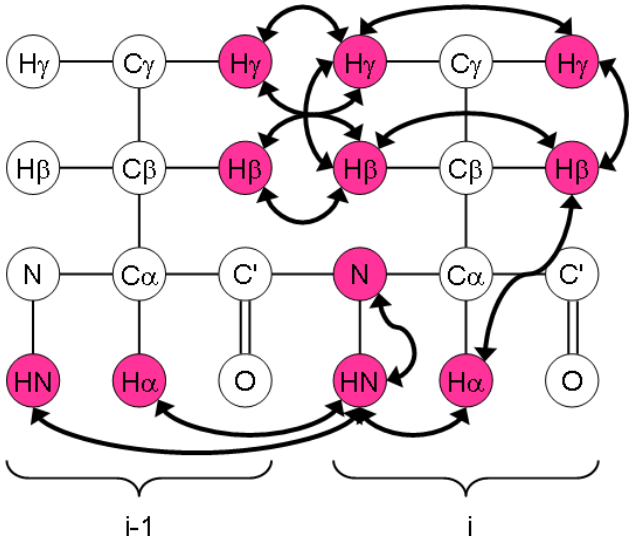

Figure 3.25: The transfer of magnetization in NOESY-^{15}N-HSQC [58].

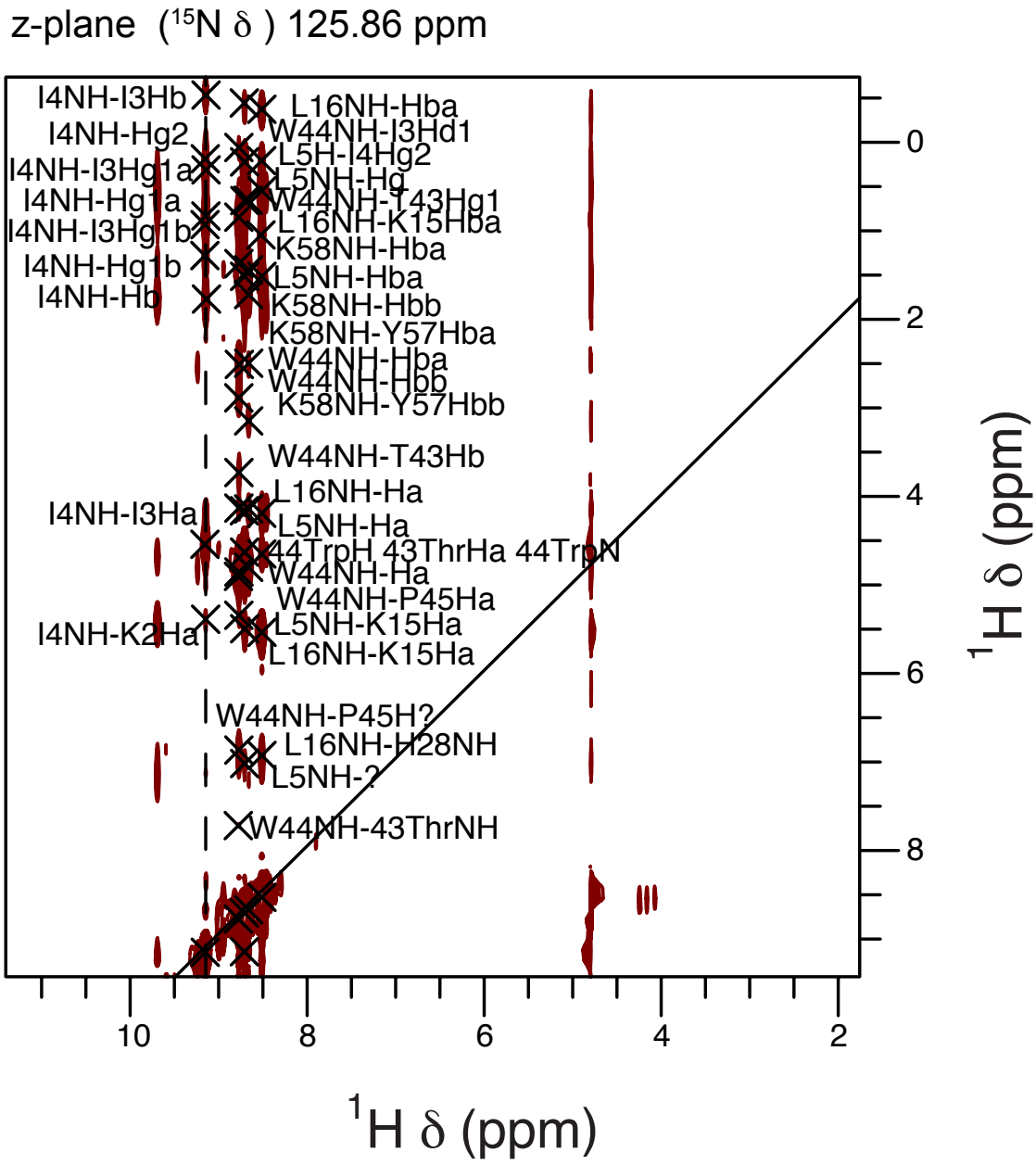

Figure 3.26: A ^{15}N plane of ^{15}N-TOCSY-HSQC spectrum showing assignments of protons and nitrogens connected through space of tunicate crystallin in the presence of Ca^{2+}.

Table 3.22: NOESY-^{15}N-HSQC NMR parameters of tunicate crystallin with 10 mM Ca^{2+}

	1H	1H	15N
SW (Hz)	11990.41	11990.41	3600.04
Number of scans	4		
Number of points	2048	48	32
Transmitter offset (ppm)	-306.90		
90 time (μs)	8.80		45.00
Decoupling power	60		48
Center frequency (ppm)	4.79	4.79	118.78

3.6.2 ^{13}C-NOESY HSQC

This experiment is similar to the NOESY-^{15}N-HSQC where the magnetization is exchanged between all hydrogens using NOEs, afterwards however, that magnetization is transferred to the ^{13}C nuclei instead of the amide nitrogen and then transferred back to the adjacent protons for detection.

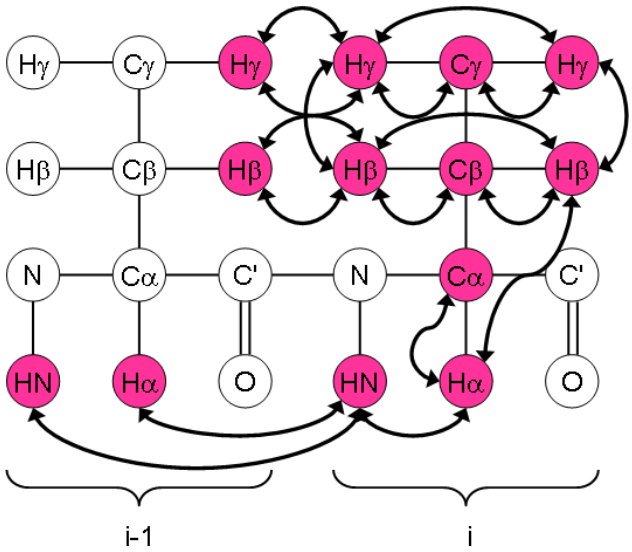

Figure 3.27: The transfer of magnetization in ^{13}C-NOESY HSQC [58].

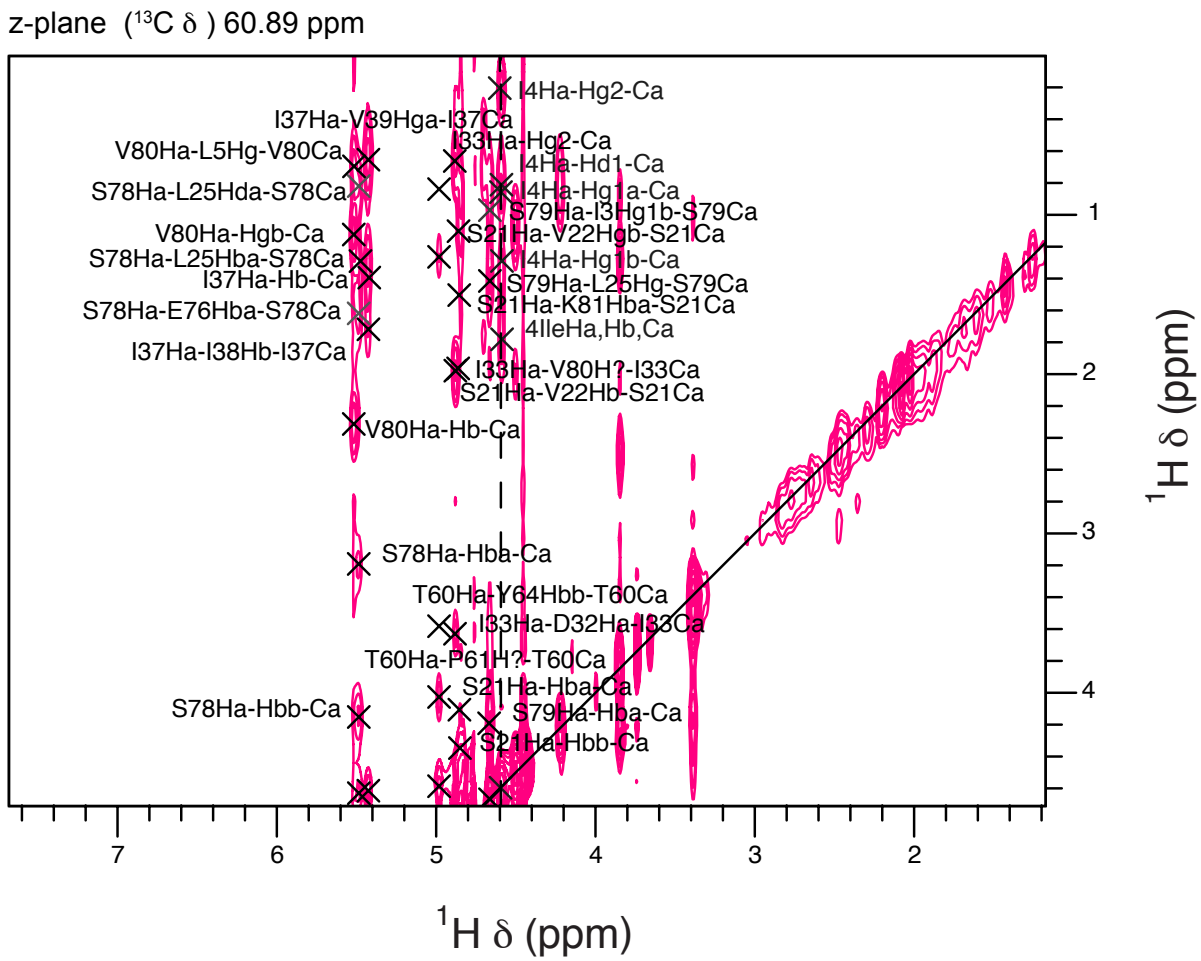

Figure 3.28: A ^{13}C plane of ^{13}C-NOESY HSQC spectrum showing assignments of protons and carbons connected through space of tunicate crystallin in the presence of Ca^{2+}.

Table 3.23: ^{13}C-NOESY HSQC NMR parameters of tunicate crystallin with 10 mM Ca^{2+}

	1H	1H	13C
SW (Hz)	12019.23	12001.20	18001.80
Number of scans	4		
Number of points	2048	48	32
Transmitter offset (ppm)	-305.88		
90 time (μs)	8.80		13.80
Decoupling power	60		41
Center frequency (ppm)	4.79	4.79	43.04

3.6.3 ^{15}N-HSQC IPAP

Long-range distance and angular restraints are calculated using measured residual dipolar couplings, and they complement the short-range distance constraints found with NOE experiments. When short-range and long-range distance restraints are taken together, they enable determination of the global structure of the biomolecule. These long-range distance restraints are measured by comparing the splitting of each amide N-H resonance in the absence (Figure 3.29) and presence of an alignment medium using a ^{15}N-HSQC in-phase, anti-phase (IPAP) NMR spectrum. The difference in their splittings corresponds to residual dipolar couplings, whether that difference is positive or negative. The alignment medium used in these experiments was a bicelle mixture consisting of 15 % w/v DLPC/DHPC and 13.4 % cholesterol sulfate with respect to moles of DLPC.

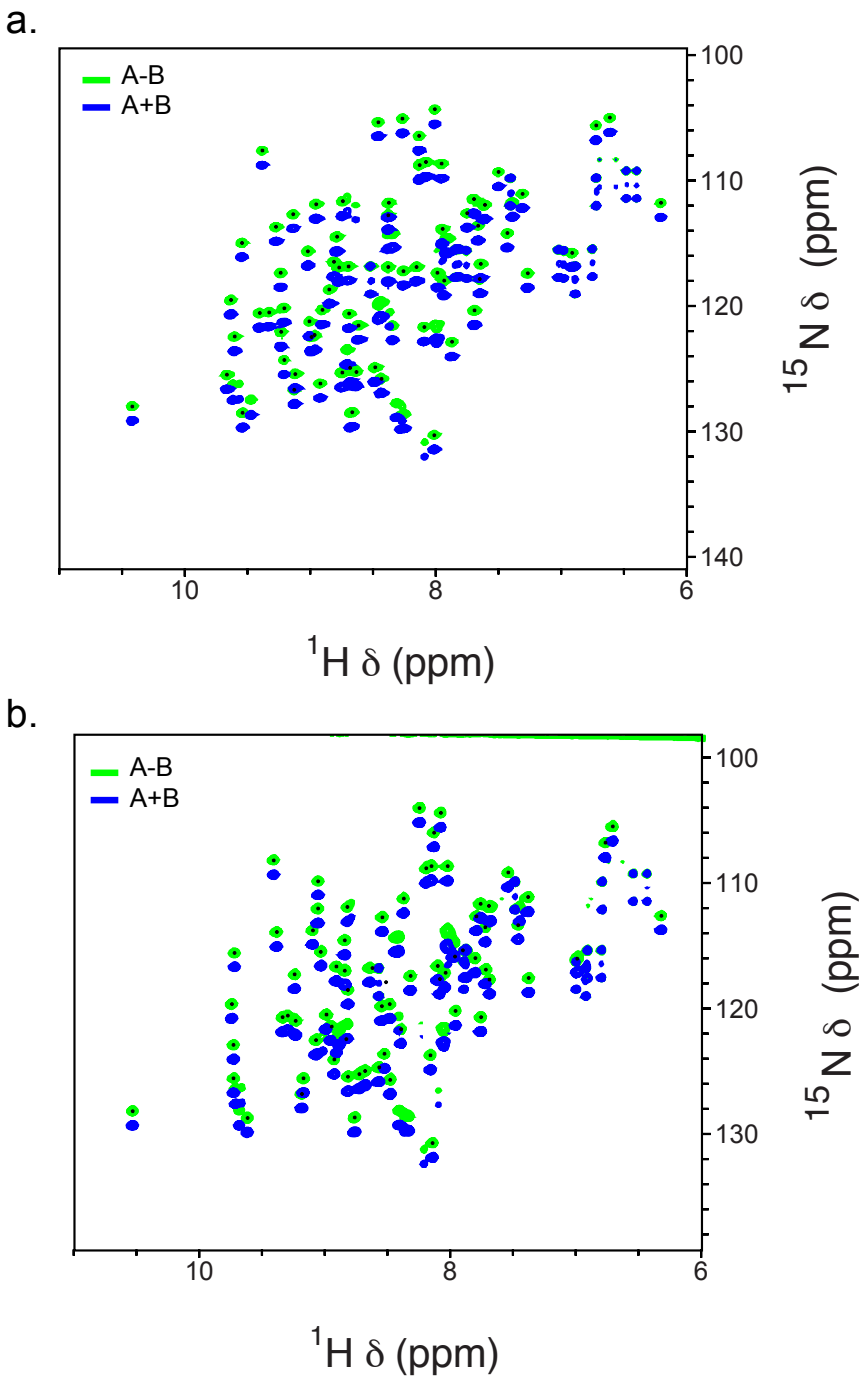

Figure 3.29: ^{15}N-HSQC IPAP spectra in the presence (a) and absence (b) of Ca^{2+} of tunicate crystallin. Each backbone peak is split, unlike in a regular ^{15}N-HSQC. This splitting corresponds to a N-H J-coupling of 91-94 Hz in the isotropic samples.

Table 3.24: ^{15}N-HSQC IPAP NMR parameters of tunicate crystallin with 10 mM Ca^{2+}

	1H	15N
SW (Hz)	12999.68	3600.00
Number of scans	32	
Number of points	1500	256
Transmitter offset (ppm)	-295.00	
90 time (μs)	13.00	48.00
Decoupling power	60	48
Center frequency (ppm)	4.78	120.15

Table 3.25: ^{15}N-HSQC IPAP NMR parameters of tunicate crystallin with 10 mM EDTA

	1H	15N
SW (Hz)	12999.68	3600.00
Number of scans	32	
Number of points	1500	256
Transmitter offset (ppm)	-298.90	
90 time (μs)	13.50	48.00
Decoupling power	60	48
Center frequency (ppm)	4.80	120.29

3.7 Hydrogen Bonds

Amide proton temperature coefficients were found by acquiring a series of ^{15}N-^{1}H HSQC experiments over a temperature range of 25-75 °C in the holo form (Figure 3.30a) and 25-50 °C in the apo form (Figure 3.30b). The sample was allowed to equilibrate for several minutes at each temperature before data acquisition were performed. The amide proton chemical

shift perturbation of each peak was plotted as a function of temperature (Figure 3.31). If the slope of the line was above the -4.6 ppb/K threshold, then that residue was hypothesized to hydrogen bond with the solvent, i.e. solvent-exchange. If the slope of the line was below the cut-off, then that residue was hypothesized to have a buried hydrogen bond [68]. The amide proton temperature coefficients are tabulated for each residue of the tunicate crystallin in the apo and holo forms (Table C.1). The hydrogen bonds from these amide proton temperature coefficients are superimposed on the X-ray crystal structure in Figure 3.32.

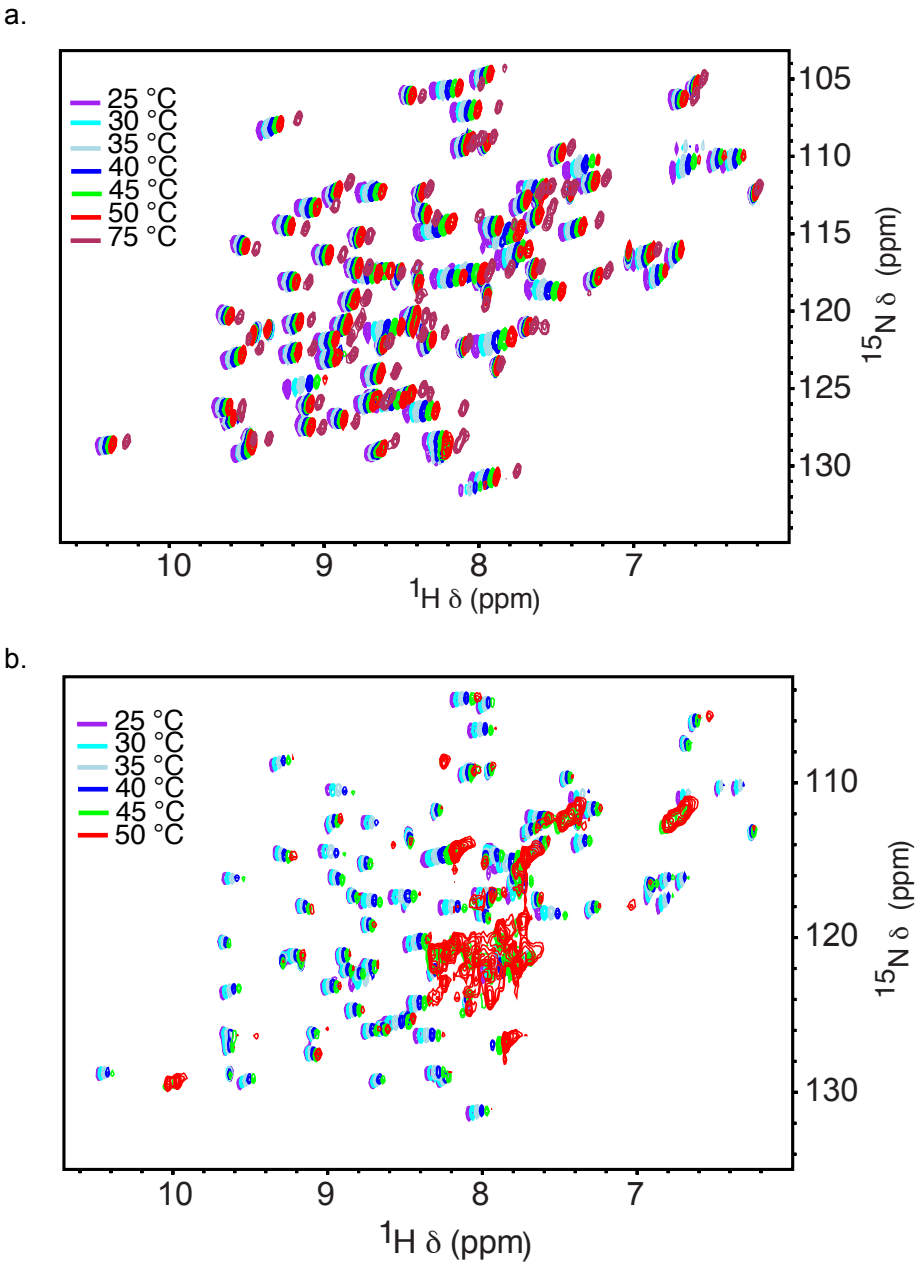

Figure 3.30: Overlay of a series of temperature ^{15}N-HSQC spectra of tunicate crystallin in the holo (a) and apo (b) form. The protein remains fully folded even at 75 °C in the holo form yet denatures at 50 °C in the apo form.

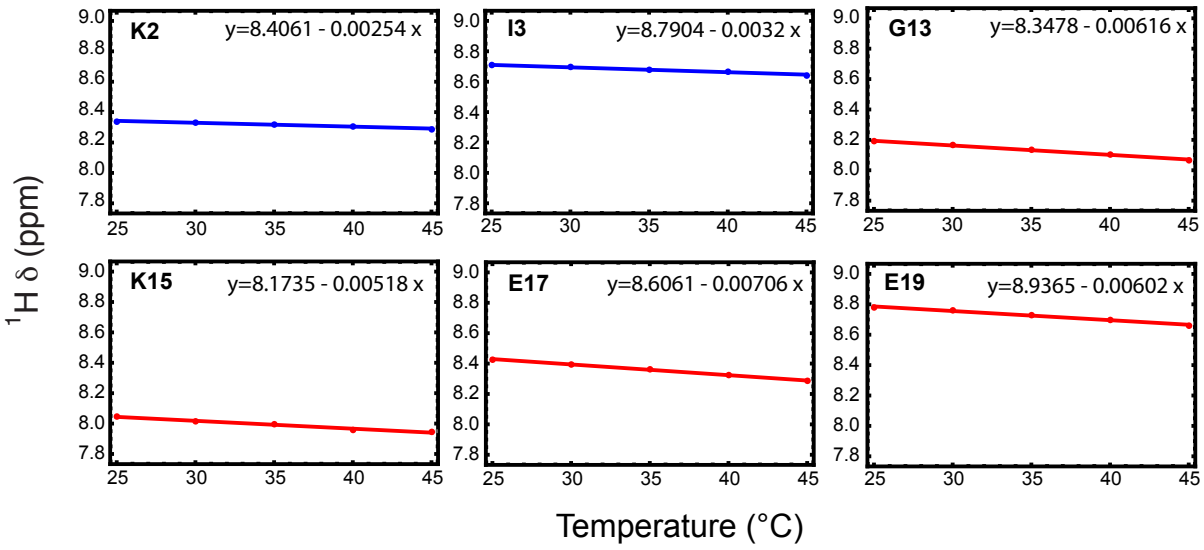

Figure 3.31: Amide proton temperature coefficient plots of six residues taken from the temperature ^{15}N-HSQC spectrum of tunicate crystallin in the presence of EDTA. Plots shown in blue have slopes $<$ -4.6 ppb/K and these residues which are hydrogen bonding intramolecularly. Plots shown in red have slopes $>$ -4.6 ppb/K and these residues which are hydrogen bonding with the solvent.

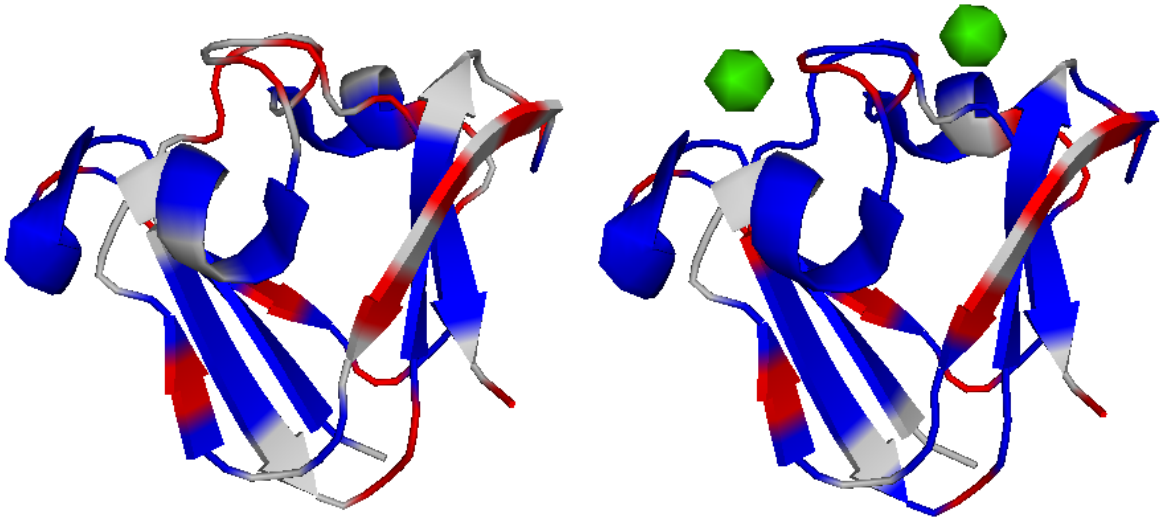

Figure 3.32: Hydrogen bonds determined from the amide proton temperature coefficients are represented on the crystal structure (PDB: 2BV2) [3]. Residues which are hydrogen bonding with the solvent are shown in red and residues which are hydrogen bonding intramolecularly are shown in blue. Both the apo and the holo form of the tunicate crystallin shows similar hydrogen bonding patterns. The main difference between the two structures is that the loop-like region which typically binds to the Ca^{2+} ions is hydrogen bonding more with the solvent in the EDTA structure.

Chapter 4

Low temperature alignment media for measuring residual dipolar couplings during biomolecular NMR structure determination.

4.1 Background

Biomolecules are essential to every living organism because they express genetic information and perform a vast array of functions, such as catalysis of metabolic reactions. DNA molecules have high backbone flexibility and bending, as well as sugar puckering and base pair rolling and twisting, all of which crucial for packaging, recognition and regulation in DNA transcription [69]. RNA structures and proteins are also highly dynamic and must undergo conformational changes to perform their specific biological functions, such as the rearrangement of secondary and tertiary structures in response to particular cellular signals.

As a result of biomolecular structure flexibility, studying them using crystallography is challenging. In crystallography the structure obtained from a diffraction pattern is static which gives no information about its structural dynamics. With appropriate attention to sample preparation, including pH and salt concentrations, solution-state nuclear magnetic resonance (NMR) offers a more attractive environment for studying dynamic structures.

Nuclear Overhauser Effect-based constraints (NOEs) and J-couplings are the most commonly used measurements in solution-state NMR structure determination of biomolecules. These data provide only short-range internuclear distance constraints (NOEs are limited to < 5 Å), as the effect scales as $\frac{1}{r^6}$, while J-couplings are inherently short-range because they are mediated by covalent bonds [70]. Using these two parameters for structure determination of large biomolecules has limitations, as short distance constraints only allow for the local structure determination, leaving the remote parts of the structure poorly defined. Complementary measurements yielding long-range distance restraints offer better parameters for studying biomolecules as they allow for the global structure determination and do not rely heavily on proton densities. Such restraints can be obtained from dipolar couplings (DCs), which measure the effect that one nucleus has on the magnetic environment of another nucleus through the direct dipole-dipole interaction. DCs provide spatial information about internuclear distances and long-range distance constraints using the average orientation of the internuclear vector $D_{ab} = -(\frac{\gamma_a \gamma_b \hbar \mu_0}{4\pi * r^3})\frac{1}{2} < 3cos^2\theta - 1 >$, where D_{ab} is the dipolar interaction between nuclei a and b, γ_a and γ_b are the gyromagnetic ratio for a and b, respectively, $\hbar$ is Planck's constant/2π, μ_0 is magnetic permeability, r is the internuclear vector between a and b, and θ is the angle between r and the magnetic field [71, 72]. The $\frac{1}{r^3}$ term in this equation allows for long-range internuclear distance measurements compared with the $\frac{1}{r^6}$ term used in short-range distance measurements from NOEs.

DCs are impossible to determine using traditional solution-state NMR because most molecules tumble at a rapid rate, averaging the $< 3cos^2\theta - 1 >$ term to zero [71, 73]. An envi-

ronment consisting of alignment media with magnetic susceptibility anisotropy in solution constrains the motion of a molecule and incompletely averages out magnetic interactions, resulting in residual dipolar couplings (RDCs) from which more accurate local and global structural features can be obtained [74, 75, 76]. The alignment medium most commonly used in biomolecular NMR structure determination consists of a bicelle mixture comprised of the long chain phospholipid 1, 2-dimyristoyl-sn-glycero-3-phosphocholine (DMPC) and the short chain phospholipid 1, 2- dihexanoyl-sn-glycero-3-phosphocholine (DHPC) [77]. Optimal alignment of DMPC/DHPC occurs at temperatures > 30 °C, above the gel-to-liquid crystal phase transition [70]. These high alignment temperatures are not ideal for structure determination of folded nucleic acids and catalytic proteins because the chemical exchange rate of imino and exocyclic amine hydrogens and other dynamic processes are too fast to observe on the NMR timescale. Therefore, obtaining bicelle alignment at low temperatures in order to determine dynamic biomolecular structures is an active area of research.

Previous work by Shapiro et al. demonstrated that cholesterol sulfate (CS), which is found in mammalian cell membranes, lowered the gel-to-liquid crystal phase transition temperature of a concentrated bicelle mixture to room temperature [78]. Alignment of the DMPC/DHPC/CS system was further improved with the addition of Mg^{2+} and Ca^{2+}, crucial divalent cations shown to participate in the folding mechanisms of nucleic acids and proteins. The presence of CS, divalent cations and the high concentration of bicelles offers an environment for aligning and stabilizing biomolecular structures in solution, however, at room temperature, imino and amine protons are still susceptible to rapid exchange and the need to optimize CS/Mg^{2+}-mediated alignment to attain a lower gel-to-liquid phase transition temperature is desired.

An alignment medium for structure determination of biomolecules in the presence of divalents that has not been explored yet consists of a bicelle mixtures comprised of the long chain phospholipid 1, 2-dilauroyl-sn-glycero-3-phosphocholine (DLPC) and the short chain

phospholipid 1, 2- dihexanoyl-sn-glycero-3-phosphocholine (DHPC). This choice of an alignment medium allows us to have more control over its alignment properties. As a result of the low gel-to-liquid phase transition temperature (- 2 °C) of DLPC, this alignment medium has been shown to align in the magnetic field at 4 °C and at - 5 °C in the presence of cholesterol sulfate (CS) [79]. At this low alignment temperature, the dynamic conformations of nucleic acids and catalytic proteins. can be more accurately determined which makes this medium a suitable candidate for its global structure determination using RDC measurements compared to the widely used alignment medium 1, 2-dimyristoyl-sn-glycero-3-phosphocholine and 1, 2-dihexanoyl-sn-glycero-3-phosphocholine (DMPC/DHPC). Here we show a proof of concept that we can use the DLPC/DHPC/CS bicelle system to measure RDCs of two biomolecules at low temperatures in the presence of their relative divalent cations; Dickerson dodecamer (DD) DNA in the presence of Mg^{2+} and a tunicate Ca^{2+} binding $\beta\gamma$-crystallin in the presence of Ca^{2+}.

4.2 Materials and Methods

4.2.1 Sample preparation

Bicelles: DLPC and DHPC lipids were purchased from Avanti Polar Lipids (Alabaster, AL) in chloroform. Appropriate volumes of the long chain (DLPC) to short chain (DHPC) were combined for a q ratio of 3.5 (q = [DLPC]/[DHPC]) and for a 25 % w/v stock concentration. Afterwards, this mixture was placed under a nitrogen stream for 8-12 hours to remove the chloroform followed by lyophilization for 24 hours. To the dried lipids, 13.4 % cholesterol sulfate (CS), with respect to moles of DLPC, was added and the contents were hydrated with 10 mM Tris buffer (pH 7.1). The hydrated bicelle sample was cycled through heating (40 °C) and cooling (5 °C) cycles for several days to dissolve the CS and obtain a viscous

consistency of the sample. The DMPC/DHPC/CS bicelles were prepared in a similar way as the DLPC/DHPC/CS bicelles.

DNA: Dickerson dodecamer DNA [d(CGCGAATTCGCG)]2 was purchased from Integrated DNA Technologies (Coralville, IA). The sample was dissolved in a 20 mM KCl buffer (pH 7.4) to a stock concentration of $\sim$ 25 mM and the two strands were annealed. Afterwards, the sample was equilibrated with 10 mM KCl via a Sephadex column.

Protein: Protein expression and purification is described in the Materials and Methods section of chapter 1.

The final DNA and protein concentrations in bicelle samples were 0.6 mM and 1.5 mM respectively. The concentration of divalent cations was 10 mM for each experiment.

4.2.2 NMR experiments

^{2}H and ^{31}P spectra of the bicelle samples were acquired using a 600 MHz Avance NMR spectrometer. Each sample was equilibrated for 15 minutes at each temperature prior to NMR data acquisition. Forty-eight scans were collected for ^{2}H experiments using the lock channel and 1024 transients were collected for ^{31}P experiments using the ^{1}H decoupled sequence.

DQF-COSY NMR spectra of bicelles in the absence of DD were acquired with 96 scans and 128 points in the indirect dimension. The acquisition time was 8 ms in the indirect dimension and 500 ms in the direct dimension. DMPC/DHPC/CS COSY spectra in the presence of DD were acquired with 8 scans (5 °C) and 16 scans (25 °C) and 640 points in the indirect dimension at both temperatures. The acquisition time was 80 ms for the indirect dimension and 100 ms for the direct dimension. DLPC/DHPC/CS COSY spectra in the presence of DD were acquired with 40 scans and 256 points in the indirect dimension. The acquisition time

was 32 ms for the indirect dimension and 100 ms for the direct dimension. All DQF-COSY data were acquired using a WATERGATE water suppression scheme.

^{15}N IPAP-HSQC spectra were acquired with 1500 points in the direct dimension and 256 points in the indirect dimension with 32 transients and a spectral width of 12999 Hz in the direction dimension and 3600 Hz in the indirect dimension.

All 2D experiments were acquired on an 800 MHz Varian INOVA system spectrometer.

4.3 Results and Discussion

The appearance and viscosity of DMPC/DHPC/CS (15% w/v DMPC/DHPC containing 13.4% CS with respect to moles of DMPC) showed a liquid crystalline phase transition from an isotropic to an anisotropic chiral nematic (Figure 4.1) with temperature increase. During the phase change, molecules transition from discoid fast tumbling micelles (bicelles) (Figure 4.1a), to wormlike micelles that orient in a magnetic field (Figure 4.1b) [80, 81]. The bicelle sample was a clear liquid below room temperature while at room temperature and above, the sample was slightly opaque and had a gel-like, viscous consistency.

The isotropic-to-anisotropic phase transition temperature of DMPC/DHPC/CS in the presence of DD was found to be 20 °C using ^{2}H and ^{31}P NMR experiments. A single HOD peak at 5-15 °C represented an isotropic unaligned phase and a splitting of that peak above 20 °C corresponded to sample alignment (Figure D.1a). These results were observed because in an anisotropic environment, an incomplete averaging of residual quadrupolar couplings occurs. Since ^{2}H nuclei have a spin of 1, alignment is indicated in ^{2}H NMR spectra by the presence of two peaks, termed quadrupolar splittings. At 5-15 °C, ^{31}P NMR spectra also showed a single isotropic peak with resonances close to 0 ppm and at 20 °C and above, an additional resonance was observed upfield, corresponding to a sample phase transition into

an anisotropic phase. Both DMPC and DHPC are aligned in this phase and are represented with two separate peaks (Figure D.1b). Addition of 10 mM $MgCl_2$ to the bicelle and DD sample improved the overall bicelle alignment as shown by the increase in the quadrupolar couplings (Figure D.1c). Although ^{2}H NMR spectra show alignment of the bicelles at 25 °C upon addition of $MgCl_2$, ^{31}P NMR spectra still show alignment of the bicelles at 20 °C (Figure D.1d), suggesting that this experiment might be more sensitive to diagnose bicelle alignment. Overall, these alignment studies show that DMPC/DHPC/CS offers a suitable alignment medium for DD and potentially other nucleic acids for NMR structure determination. ^{2}H and ^{31}P NMR spectra for 0.6 mM DD without lipids showed an unaligned isotropic phase throughout the temperature range (data not shown).

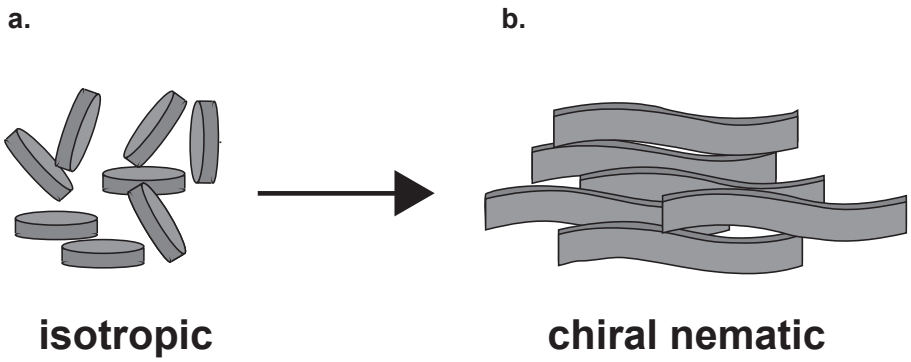

Figure 4.1: Isotropic (a) to chiral nematic (b) phase transition of DMPC/DHPC/CS.

Quantification of DD alignment at 5 °C and 25 °C in the DMPC/DHPC/CS system with 10 mM Mg^{2+} was performed via measurement of the H5 and H6 aromatic nucleotide protons of the four cytidines (C1, C3, C9, C11) in the absence and presence of the alignment medium. A change in these couplings in the presence of DMPC/DHPC/CS suggests DD alignment. This change is attributed to observable dipolar couplings during sample alignment, which either add or subtract from the J-couplings depending on the direction of the alignment tensor, giving rise to RDCs. Sample alignment is directly proportional to the observable RDC values. To measure the H5/H6 cytidine couplings, 2D ^{1}H-^{1}H double filtered quantum-COSY (DQF-COSY) data were acquired. This experiment is an improvement on a standard

COSY; it is phase sensitive and suppresses the diagonal peaks, enabling measurements of small coupling values close to the diagonal (Figure D.2). Slight alignment at 5 °C and strong alignment at 25 °C of DD was observed with a change in the H5/H6 cytidine couplings in the presence of DMPC/DHPC/CS (Figure D.3, Table D.1). The absence of H5 and H6 proton cross peaks from C9 and C11 residues was observed in the spectrum at 25 °C. The absence of these peaks could have resulted from extreme peak broadening in the gel-like sample due to the concomitant decrease in T1 and T2 relaxation times or from the residual dipolar couplings canceling out from the J-couplings causing the splittings to fall below threshold in the DQF-COSY spectrum.

After successfully aligning DD at 25 °C with DMPC/DHPC/CS in the presence of 10 mM Mg^{2+}, optimization of the bicelle system was performed for low temperature alignment studies of nucleic acids. Since Mg^{2+} improved the overall bicelle alignment, manipulation of divalent cation (Mg^{2+} and Ca^{2+}) and CS concentrations were performed in an attempt to lower the temperature of DMPC/DHPC alignment, however, varying these concentrations did not result in a lower phase transition temperature of the system (Table D.2). As a result of the high phase transition temperature of the long chain phospholipid, DMPC (24 °C), it was hypothesized that a better way of achieving bicelle alignment at low temperatures was to utilize an alignment medium consisting of a long chain phospholipid having a low phase transition temperature, such as 1,2-dilauroyl-sn-glycero-3-phosphocholine (DLPC). This phospholipid has a phase transition temperature of -2 °C. In combination with CS, this system has been shown to align at temperatures as low as -15 °C [82, 79]. As a result of the low gel-to-liquid phase transition temperature of DLPC/DHPC/CS, the consistency of the bicelle sample (15 % w/v DLPC/DHPC containing 13.4 % CS with respect to moles of DLPC) was a gel-like viscous consistency at temperatures lower than 10 °C while at temperatures above that, the sample was more liquid-like.

From ^2H NMR experiments, the phase transition temperature of the DLPC/DHPC/CS

alignment medium was found to be 6 °C and in the presence (Figure 4.2b) and absence (Figure 4.2a) of DD and 10 mM Mg^{2+}. Upon addition of DD, there was a slight decrease in the quadrupolar couplings at each temperature as a result of DD binding to Mg^{2+}, which decreased the metal ion concentration that was used by the bicelles to improve their aligned phase (Figure 4.2). The alignment of these bicelles was also tested in the presence of tunicate crystallin and 10 mM Ca^{2+} and this system was found to align at 8 °C (Figure 4.3). Since this protein is a Ca^{2+} binding protein, the addition of it to the bicelles decreased their alignment because the divalent metal ion concentration that was used by the bicelles to increase their aligned phase had decreased. These ^{2}H NMR spectra show that the addition of biomolecules (DD or tunicate crystallin) to the bicelles does not change their aligned phase significantly and these bicelles can be used to probe the alignment of these biomolecules in the presence of their relevant divalent metal ions at low temperature.

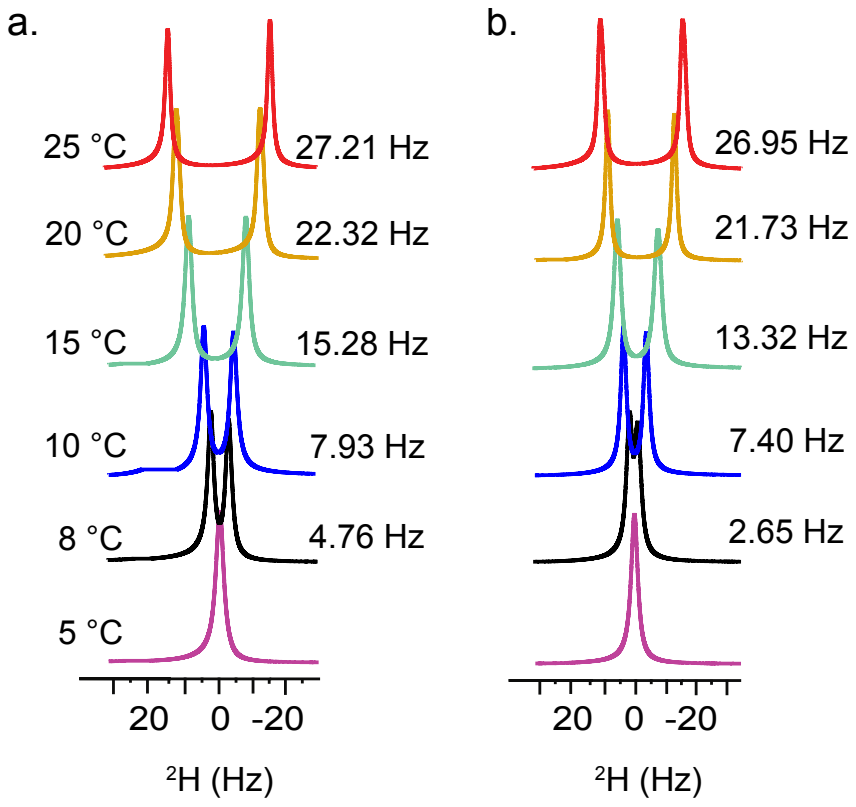

Figure 4.3: ^{2}H NMR spectra of DLPC/DHPC/CS in the presence of 10 mM Ca^{2+} and in the absence (a) and presence (b) of tunicate crystallin. Alignment of the bicelles occurs at 8 °C in both samples.

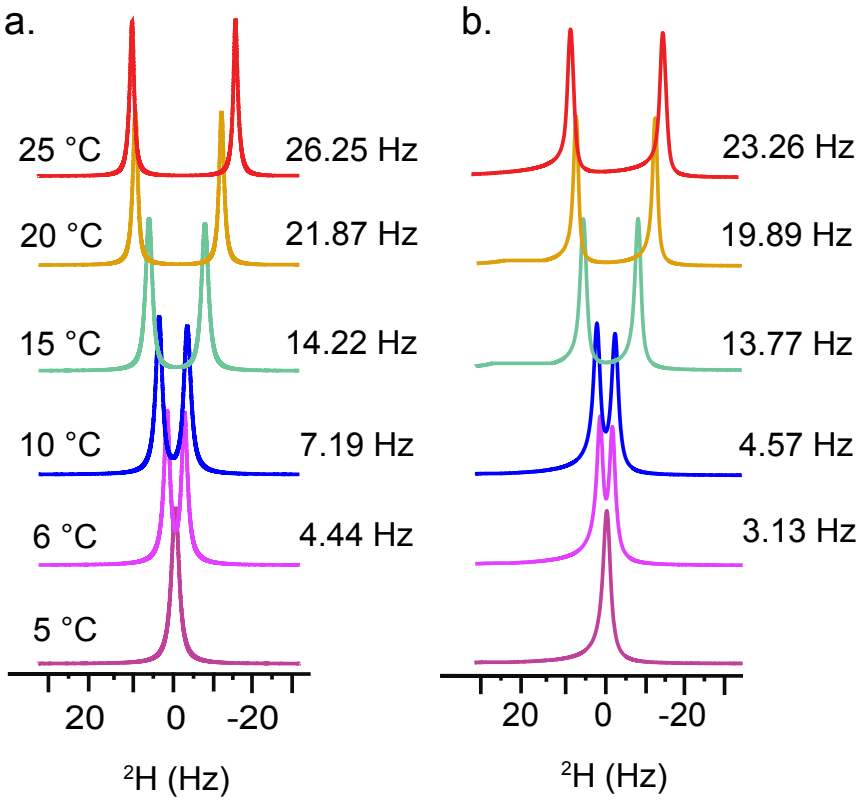

Figure 4.2: ^{2}H NMR spectra of DLPC/DHPC/CS in the presence of 10 mM Mg^{2+} and in the absence (a) and presence (b) of DD. There is a liquid crystallin phase transition from the isotropic to anisotropic phase at 6 °C. Addition of DD decreased the bicelle alignment slightly as can be seen by the decrease in the deuterium splittings.

To probe the alignment of DD by the DLPC/DHPC/CS bicelles, measurements of H5/H6 cytidine couplings of the dodecamer was performed using DQF-COSY NMR experiments. Since ^{2}H NMR experiments did not show the best sensitivity to probing bicelle alignment with the DMPC/DHPC/CS system, we checked DD alignment at temperatures lower than 6 °C. The COSY data indicated a moderate alignment at -5 °C (Figure 4.4 a,c) and a stronger alignment at 5 °C of the DNA (Figure 4.4 a,b). At 5 °C, the couplings increased from $\sim$ 11-15 Hz in the absence of the alignment medium to $\sim$ 46-57 Hz when the alignment medium was added. At - 5 °C, the couplings increased to $\sim$ 23-41 Hz when the alignment medium was added. The couplings at - 5 °C were compared to the couplings at 5 °C in the absence of DLPC/DHPC/CS because at temperatures below zero, the DNA sample would freeze without the high viscosity from the bicelles. There were several H5/H6 cytidine cross-peaks

which were missing from the DQF-COSY spectra at both 5 °C and -5 °C (Table 4.1) which could be attributed to either line broadening of those peaks due to sample viscosity or the cancelation of the residual dipolar couplings from the J-couplings during alignment.

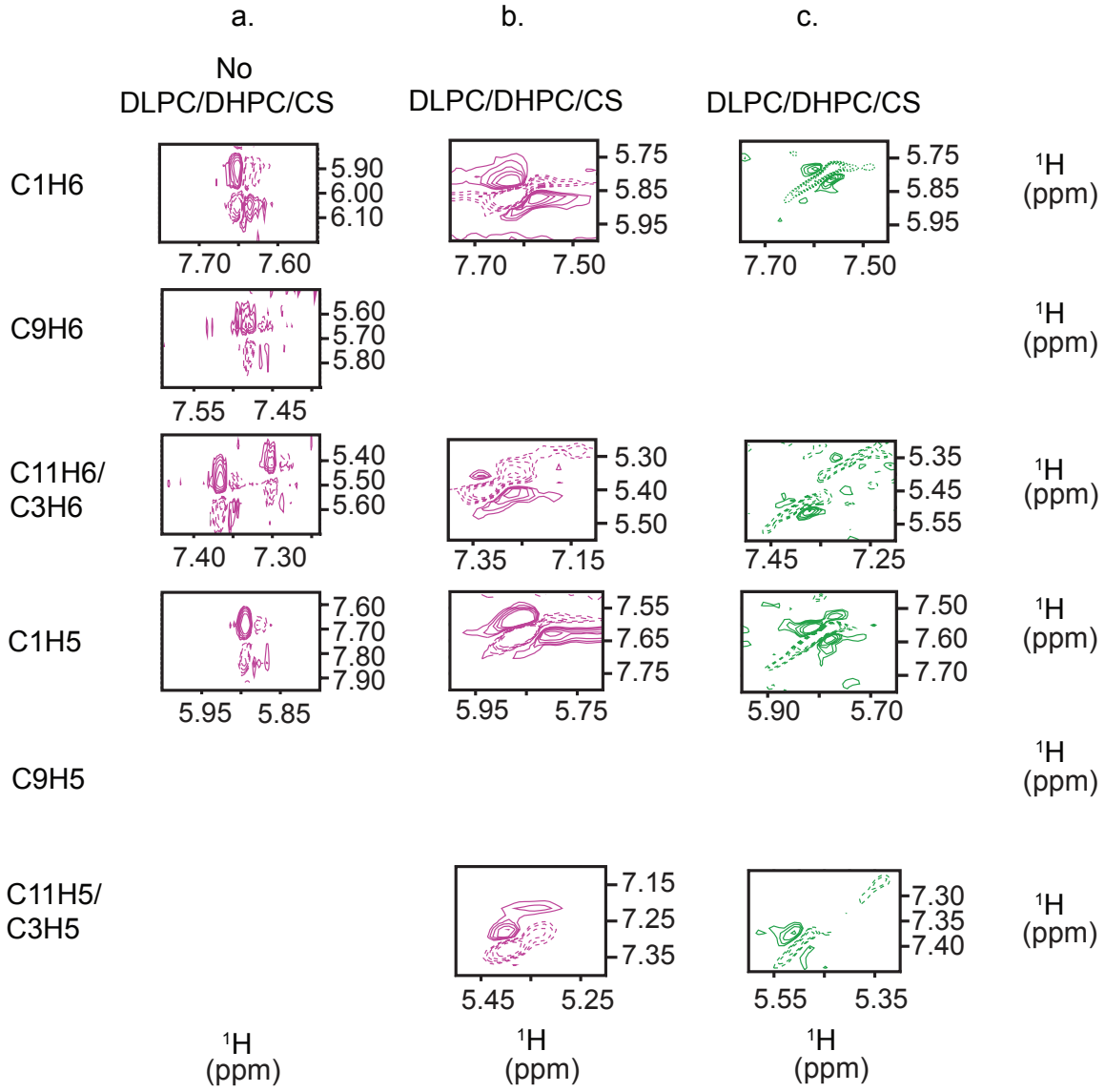

Figure 4.4: Small regions of DQF-COSY spectra comparing DD cytidine H5/H6 couplings in the absence (a) and presence (b, c) of DLPC/DHPC/CS at 5 °C (magenta) and -5 °C (green). Solid contours represent positive intensities and dashed contours represent negative intensities. Couplings were measured using only the F2 dimension from the top of a positive contour to the top of a negative contour.

Table 4.1: H5/H6 cytidine splittings in Hertz in the presence and absence of DLPC/DHPC/CS and all in the presence of 10 mM Mg^{2+} at 5 °C and - 5 °C. X represents couplings which were not resolved or were absent from the spectrum as a result of negative dipolar couplings.

	DD 5 °C (Hz)	DD + DLPC/DHPC/CS 5 °C (Hz)	DD + DLPC/DHPC/CS -5 °C (Hz)
C1H6	11.36	46.22	25.93
C9H6	15.60	X	X
C11H6	12.08	X	31.35
C3H6	14.88	57.17	41.02
C1H5	12.96	54.48	26.96
C9H5	X	X	X
C11H5	X	X	23.81
C3H5	X	54.39	X

In order to determine if the bicelles were aligning the tunicate crystallin in the presence of 10 mM Ca^{2+} at low temperatures, ^{15}N-HSQC IPAP NMR experiments were acquired to measure the N-H couplings of the backbone residues. This experiment reduces spectral crowding and separates the doublet components that are obtained due to the absence of decoupling during the t1 and t2 evolution periods, into two separate spectra. One spectrum is recorded with in-phase doublets and one with anti-phase doublets [83, 84]. The two spectra are then added and subtracted to obtain the N-H couplings. A typical $^{1}J_{N-H}$ is approximately 93 Hz and if that splitting either decreases or increases upon addition of bicelles (depending on the sign of RDCs), alignment is occurring of that residue. In the presence of the bicelles, this coupling is referred to as the J+D due to the contribution of residual dipolar couplings to the N-H splittings. Figure 4.5 shows that upon addition of bicelles, there is a change in the N-H couplings of the tunicate crystallin at 8 °C. This change in the coupling corresponds to

alignment of the tunicate crystallin in the magnetic field. Residual dipolar couplings of 37 residues of the tunicate crystallin are tabulated in Table 4.2.

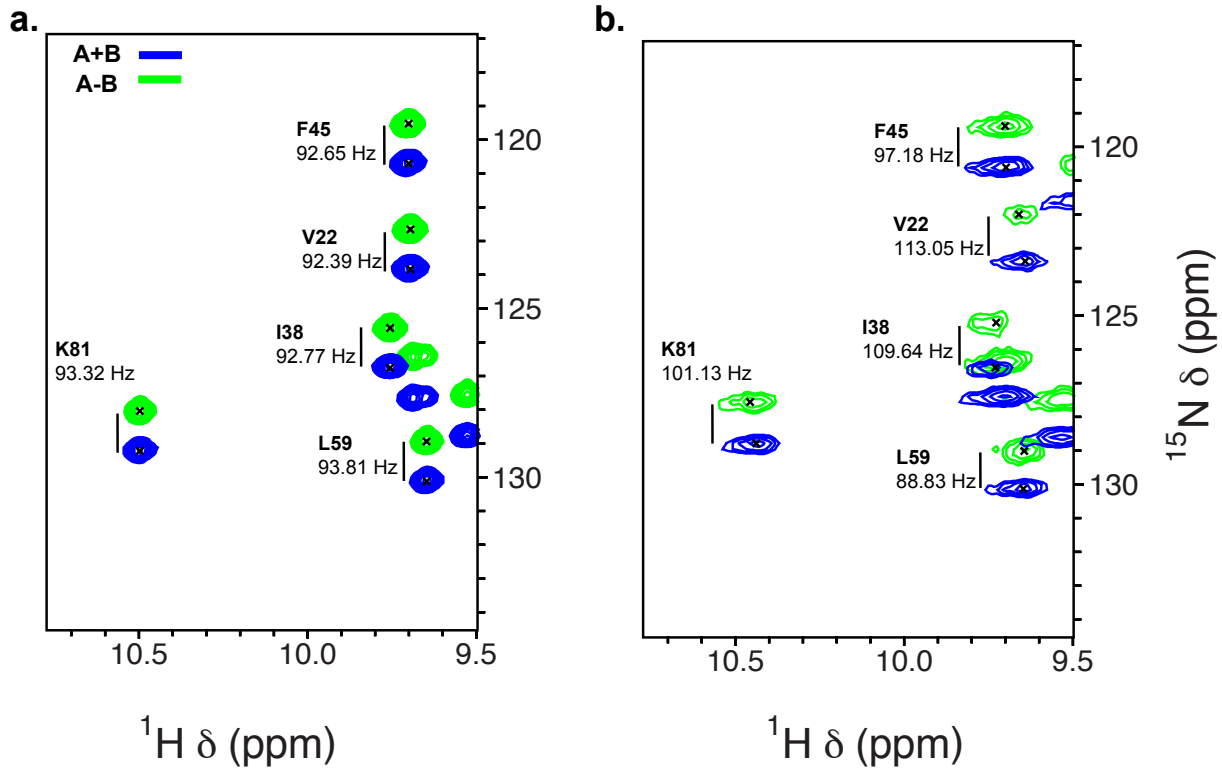

Figure 4.5: Small region of the ^{15}N-HSQC IPAP of tunicate crystallin with 10 mM Ca^{2+} taken at 8 °C in the absence (a) and presence (b) of 15 % w/v DLPC/DHPC and 13.4 % CS with respect to moles of DLPC. There are five residues that are shown in the spectra which are aligned in the presence of the bicelles as indicated by the change in the N-H couplings. This change in the couplings is used to calculate residual dipolar couplings of each residue.

Table 4.2: Residual dipolar couplings of 37 residues of the tunicate $\beta\gamma$-crystallin in the presence of 10 mM Ca^{2+} at 8 °C.

Residue	J (Hz)	J+D (Hz)	RDC (Hz)
I3	93.78	109.59	15.81
I4	92.60	127.11	34.51
E7	94.07	104.77	10.70
V9	93.97	86.20	-7.77
G12	94.48	101.47	6.99
G13	94.37	66.76	-27.61
L16	92.56	125.10	32.54
E17	93.37	142.98	49.61
S21	93.86	78.91	-14.95
V22	92.39	113.05	20.66
V27	93.27	143.95	50.68
G29	94.84	64.81	-30.03
F30	92.44	66.52	-25.92
D32	95.04	106.80	11.76
I33	91.11	68.20	-22.91
S36	93.18	108.55	15.37
I37	92.08	108.73	16.65
I38	92.77	109.64	16.87
V39	92.71	104.35	11.64
S41	93.82	105.89	12.07
G42	94.08	109.39	15.31
F45	92.65	97.18	4.53
V46	94.13	121.71	27.58
D49	94.63	117.13	22.50

G51	93.66	100.15	6.49
S53	92.73	112.56	19.83
G54	94.01	84.40	-9.61
S56	92.53	122.57	30.04
L59	93.81	88.83	-4.98
G62	93.45	131.63	38.18
G68	95.24	89.45	-5.79
S69	94.48	145.56	51.08
W70	92.55	113.69	21.14
G72	94.48	73.16	-21.32
D74	94.18	82.80	-11.38
S79	94.13	122.35	28.22
V80	92.25	106.89	14.64
K81	93.32	101.13	7.81

4.4 Conclusions and Future Directions

RDCs are critical for structure determination of biomolecules as they can provide valuable structure information that NOEs and J-couplings are not able to provide. Since nucleic acids have many exchangeable protons which are solvent exposed and they are highly dynamic, low temperature environments are better for their structure determination. DLPC/DHPC/CS offers a suitable alignment medium for aligning biomolecules at low temperatures in the presence of their respective divalent metal ions in measuring long range distance restraints. We have shown that this medium can be used to align Dickerson Dodecamer DNA in the presence of Mg^{2+} at 5 °C and a tunicate crystallin protein in the presence of Ca^{2+} at 8

°C. Besides measuring RDCs using this bicelle mimetic alignment medium, we want to also solve structures of membrane proteins using solid-state NMR. One example of such protein that we are interested in investigating are two plant specific inserts (Droserasin 1 and 2) that we found in the genome of a carnivorous plant *Drosera capensis* which are hypothesized to interact with fungi membranes and kill the fungi as a defense mechanism. Attempts of expressing and purifying Droserasin 1 are detailed in the appendix.

Chapter 5

In Situ NMR Measurement of Macromolecule-Bound Metal Ion Concentrations.

5.1 Background

Mg^{2+} and Ca^{2+} play pivotal roles in biomolecular structure and function. Mg^{2+} stabilizes nucleic acid structures and directly participates in the catalytic activity of many ribozymes and in protein enzymes such as kinases [85, 86, 87]. Ca^{2+} is involved in cell signaling pathways via its interactions with calcium-binding proteins [88]. Membrane mimetics composed of mixtures of long-chain and short-chain phosphatidylcholine lipids (bicelles) also bind Mg^{2+} and Ca^{2+}, which in turn modulate their liquid crystalline phases [89, 90] in ways that are useful for both crystallographic [91] and NMR protein structural studies. In such complex multi-component samples, the concentration of bound divalent ions can be quite different from the total amount added: several competing binders may be present and all of the rel-

evant equilibria can vary with temperature and pH. Understanding the chemical processes taking place in biomolecular NMR samples requires in situ measurement of the bound divalent ion concentrations. Whereas equilibrium dialysis and size-exclusion chromatography can be used to establish predetermined concentrations of free metal ions, some samples, e.g. the highly concentrated lipid and surfactant mixtures used for residual dipolar coupling (RDC) measurements in biomolecular structure determination, are difficult to prepare using these methods. A known amount of divalent metal ions is added to these samples upon preparation; however the fraction of the ions bound to the macromolecules is usually unknown.

Although *in vivo* concentrations of Ca^{2+} can be measured with fluorescent dyes due to low μM ranges of this divalent ion, biomolecular NMR samples are usually at mM concentrations and require higher than μM concentrations of Ca^{2+} and the use of alternative techniques to measure concentrations. For example, proteins such as phospholambans [92, 93], annexins [94, 95] and some $\beta\gamma$-crystallins [3, 13] display Ca^{2+}-dependent conformational changes where the full investigation of requires stoichiometric or higher concentrations of Ca^{2+}. ^{31}P NMR has previously been used to determine the cytosolic [Mg^{2+}] *in vivo* in mM ranges using endogenous probes such as ATP and phosphocreatine [96, 97, 98]. Free [Mg^{2+}] in skeletal and cardiac muscles was found to be 0.6-0.8 mM [99, 100, 101]. Shulman et al. have used ^{31}P NMR to measure the binding of divalent cations with AMP and RNA and discovered that the phosphate groups were involved in this interaction [102]. Changes in the ^{31}P chemical shift of the chelator binding site (e.g. the β- and γ-phosphates in ATP and the α- and β-phosphates in ADP) [103, 104] are straightforwardly related to the binding of divalent ions. This relationship enables the ^{31}P spectrum to serve as a sensitive reporter of the amount of divalent ions bound to macromolecules when the total ion concentration in the NMR sample is known.

In this chapter, a minimally invasive and generally applicable *in situ* approach is presented

for determining the concentration of macromolecule- bound Mg^{2+} or Ca^{2+} given a known amount of a single divalent species added to the sample. We chose deoxycytidine diphosphate (dCDP) as a metal ion chelator over the triphosphate form because its binding constant for divalent ions (i.e. log K of CDP for Mg^{2+} is 3.22, versus log K of 4.03 for CTP) [105] allows concentration measurements in the low millimolar range [106, 107]. Furthermore, dCDP is more stable than dCTP over the timescales and temperatures used in biomolecular NMR. Additionally, the characteristic doublet of H5-H6 in the ^{1}H spectrum of dCDP serves as an internal standard for RDC measurements in the bicelle samples used for structural studies. By monitoring the α- phosphate ^{31}P chemical shift of dCDP as a function of free metal ion concentration in solution, the concentration of Mg^{2+} or Ca^{2+} bound to the biomolecule(s) of interest may be calculated using standard curves such as these shown in (Figure 5.1) and Equations 1, 2 and 3. Because pH and temperature can affect the affinity of divalent ions for biomolecules as well as the phosphate chemical shifts, these variables are considered in constructing the standard curves. In this case, low temperatures were considered because the exchange rate of exchangeable protons in nucleic acids is slowed, facilitating NMR structure determination.

5.2 Materials and Methods

5.2.1 Sample preparation

The DLPC/DHPC/CS bicelles, DD and protein samples were prepared as described in Materials and Methods sections of chapters 1 and 4.

NMR sample preparation: NMR samples for Mg^{2+} and Ca^{2+} titration experiments were prepared in either 10 mM piperazine (pH 6.05) or 10 mM Tris buffer (pH 7.1, 8) with 0.3 mM dCDP (Sigma Aldrich) and 10 % D_2O. Increasing concentrations of $MgCl_2$ and $CaCl_2$

at the appropriate pH in either 10 mM piperazine or 10 mM Tris with 10 % D_2O were added to the dCDP NMR samples for final concentrations of 0.1 - 50 mM.

DNA, lipid and protein NMR samples (pH 7.1) were prepared to final concentration of 1.5 mM DNA, 15 % w/v lipids and 2 mM protein in 10 mM Tris buffer with 10 % D_2O, 6 mM Mg^{2+} or 10 mM Mg^{2+} or 7 mM Ca^{2+} or 10 mM Ca^{2+} and 0.3 mM dCDP.

The pH of each sample was measured using an Accumet Cole-Palmer pH probe. The pH at 8 °C was measured by cooling the sample in an ice water bath having a temperature of 8 °C.

5.2.2 NMR experiments

Mg^{2+} and Ca^{2+} titration 31P experiments and DNA ^{31}P experiments were collected on a 600 MHz Bruker Avance spectrometer equipped with a TBI probe. 1024 transients were collected for each experiment.

^{31}P experiments on bicelle and protein samples as well as ^{15}N-^{1}H HSQC experiments were performed on a Varian INOVA system operating at 800 MHz equipped with a $^{1}H/^{13}C/^{31}P$ 5 mm tri-axis PFG triple-resonance probe using a Hahn echo sequence to suppress one of the bicelle peaks which was overlapped with the α-phosphate dCDP peak. The DNA spectra were acquired with 19,000 scans at 25 °C and with 9500 scans at 8 °C. The bicelles + Mg^{2+} spectra were acquired with 23000 scans and an echo delay of 0.0003 s at 8 °C. The bicelles + Ca^{2+} spectra were acquired with with 25000 scans and an echo delay of 0.0006 s at 8 °C. The protein spectra at 25 °C and 8 °C were acquired with 20000 scans. ^{15}N-^{1}H HSQC experiments were acquired with 4 scans in the direct dimension and 64 scans in the indirect dimension. The data were processed using TopSpin, NMRDraw or Sparky. Chemical shift values were obtained by fitting a Lorenzian line shape to the α- phosphate peak in each NMR

spectrum. Best results are obtained when the sample preparation and data acquisition for the standards and samples of interest are performed under the same experimental conditions.

5.2.3 Construction of titration curves and error analysis

^{31}P chemical shifts were measured relative to an external standard of phosphoric acid. An external standard was used instead of measuring the difference between the α- and β- phosphates as is done in the presence of ATP *in vivo*, because both the α- and β- phosphates shift with the addition of metal ions. New titration curves must be generated when using our technique for calculating the bound metal ion concentrations at different NMR fields because the exchange process is field-dependent.

Titrations at pH 7.05 and 25 °C were performed in triplicate with 0.01, 10 and 50 mM Mg^{2+} in order to obtain error bars for the α-phosphate chemical shift measurements. From these titrations, this chemical shift error was found to be ± 0.03 ppm, and all other chemical shift determinations were assumed to have similar errors. The data obtained at pH 7.05 and 25 °C (including all triplicates) were fit to the sigmoidal equation describing cooperative binding, and the relative errors of $K_{1/2}$ and n parameters obtained from this fit were assumed to be representative of the errors in all data sets as tabulated in Tables 5.1 and E.14.

In order to determine the free divalent metal ion concentrations in the biomolecular samples, a Monte Carlo simulation was implemented. Using the $K_{1/2}$ and n values found from the nonlinear regression curves of each titration, as well as the relative errors associated with these values, 10000 normally distributed parameter sets ($K_{1/2}$ and n) were generated using Mathematica. The mean of these calculated concentrations was reported as the $[M^{2+}_{Free}]$ concentration, and the standard deviation was reported as the error in Table 5.2.

5.3 Results and Discussion

To construct standard titration curves for Mg^{2+} and Ca^{2+} at different pHs and temperatures, increasing concentrations of $MgCl_2$ (Figure 5.1a) and $CaCl_2$ (Figure 5.1b) (0.01-50 mM) were added to NMR samples containing 0.3 mM of dCDP in either 10 mM piperazine or Tris-HCl buffer. We chose this relatively low concentration of dCDP to minimize interference of the probe with our biological systems. If a different concentration of dCDP is desired, new titration curves must be generated, however doubling the concentrations of dCDP only minimally changes the free divalent metal concentrations and therefore the macromolecule-bound concentrations (as shown for 0.6 mM dCDP in Figure E.1). The chemical shift values for each of the data points are tabulated in Tables E.1- E.13. To verify that negligible amounts of divalent metal ions were present in the dCDP samples prior to titration of divalent cations, EDTA was added to a sample of dCDP at pH 7.05 and ^{31}P spectrum was acquired at 25 ° C as a control. The acquired α-phosphate chemical shift was within the $\pm$ 0.03 ppm error in the chemical shift determination as described in the error analysis section of the Supplemental Information. The resulting titration curves (Figure 5.1) were fit using nonlinear regression in Mathematica to a sigmoidal function shown below in Equation 1, which relates to the Hill equation [108] and describes cooperative binding:

$$\delta_c = \delta_\infty + Span(1 - \frac{[M^{2+}_{Free}]^n}{K_{1/2}+[M^{2+}_{Free}]^n}) \quad (1)$$

where $[M^{2+}_{Free}]^n$ is the free metal ion concentration assuming that dCDP is in a 1:1 stoichiometric ratio with the metal ion, δ_∞ represents the chemical shift at binding saturation, δ_c represents the chemical shift corresponding to the $[M^{2+}_{Free}]^n$ on the titration curve, Span is the range encompassing the initial (δ_∞) and final (δ_c) chemical shifts measured during the titrations, n is the polynomial exponent that determines if the binding of metal ions to the dCDP ligand is cooperative and $K_{1/2}$ is the midpoint concentration when the bound dCDP is in equilibrium with the free dCDP. Values acquired via the nonlinear regression for ^{31}P

δ_∞, $K_{1/2}$ and n at several pHs and temperatures are tabulated in Tables 5.1 and E.14.

Our data in Tables 5.1 and E.14 show that the $K_{1/2}$ values of Ca^{2+} for dCDP were higher than those of Mg^{2+}, representing a tighter binding of dCDP to Mg^{2+} than to Ca^{2+}. The stronger affinity is due to the smaller ionic radius and larger intermolecular interaction energy of Mg^{2+} [109]. Because the pKa of the terminal phosphate is 6.38 [105], it is partially protonated throughout the range of pH values studied, affecting the chemical shift of both phosphates. Binding of divalent ions results in displacement of the protons on the phosphate groups causing the ^{31}P chemical shift to change [96]. We found that the $K_{1/2}$ values for the binding of divalent ions to the α-phosphate were highly sensitive to pH, which is an important consideration in measuring the bound concentrations in situ because presumably binding for other biomolecules is also pH sensitive. The polynomial exponent (n) values were ~ 1 for Ca^{2+} implying the formation of a 1:1 dCDP: metal ion complex, whereas for Mg^{2+} they became > 1 upon an increase in pH, indicating a cooperative binding process where binding of dCDP to the metal ions was facilitated by previously bound dCDP (2:1 dCDP: metal ion complex) as observed by Frey and Stuehr [105].

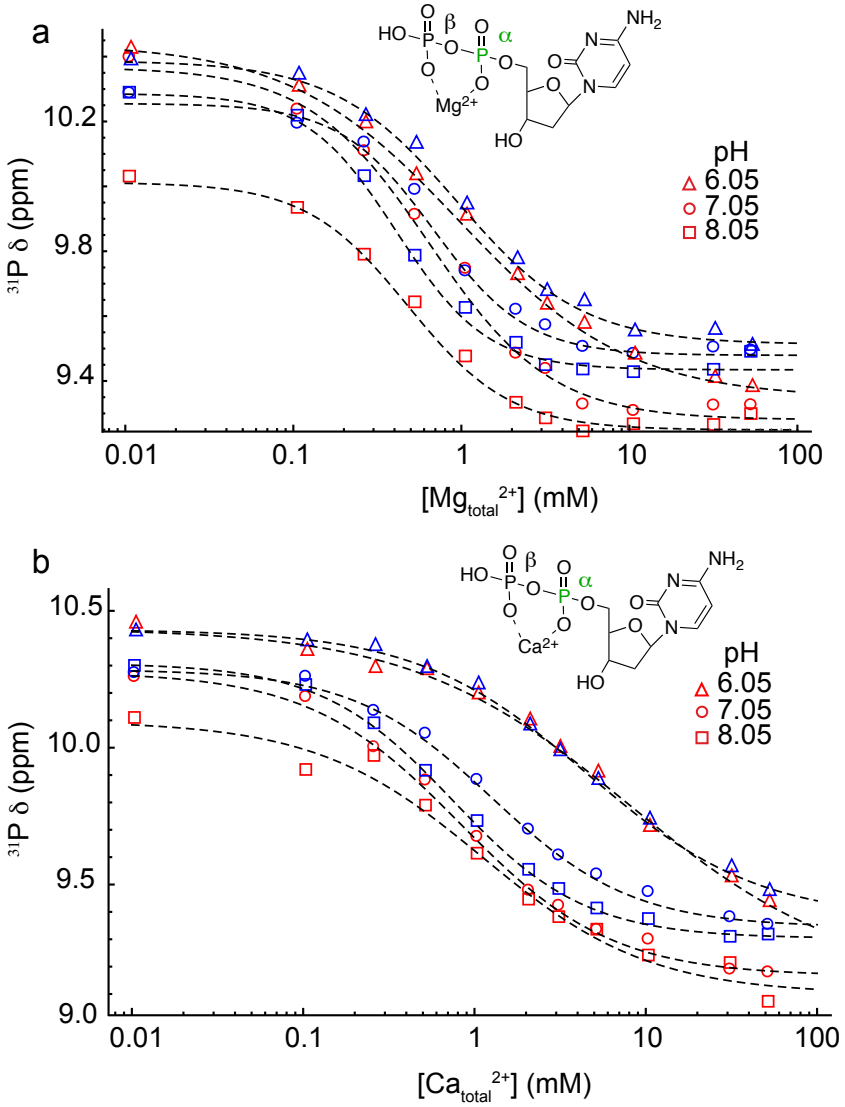

Figure 5.1: Titration curves of the α-phosphate ^{31}P chemical shift as a function of increasing (a) $[Mg^{2+}_{Free}]$ and (b) $[Ca^{2+}_{Free}]$ at different pH values and temperatures relative to 85 % phosphoric acid (external reference). Blue represents titrations at 8 °C and red represents titrations at 25 °C. At 8 °C, the pH increases by about 0.2 units from the pH values given.

Table 5.1: Interaction of the dCDP α-phosphate with $[Mg^{2+}_{Free}]$.

pH/Temp (°C)	δ_∞*(ppm)	$K_{1/2}$*(mM)	n*
6.05/25.0	9.33±0.03	0.84±0.12	0.77±0.08
6.25/8.0	9.51±0.03	0.79±0.11	1.10±0.12
7.05/25.0	9.28±0.03	0.47±0.07	1.06±0.11
7.25/8.0	9.48±0.03	0.43±0.06	1.51±0.16
8.05/25.0	9.25±0.03	0.25±0.03	1.23±0.13
8.25/8.0	9.44±0.03	0.13±0.02	1.47±0.16

*^{31}P δ_∞, midpoint ($K^{1/2}$) and polynomial exponent (n) values with their relative uncertainties at different pH and temperature values.

The line shapes observed in the ^{31}P spectra of dCDP are dominated by the exchange process between the bound and unbound forms. At concentrations well below saturation, the phosphate peak is broad, with substantial narrowing observed near the titration extremes. Even at low temperatures, broad peaks were observed for the bound versus the unbound state of the alpha phosphate of dCDP similar to Sontheimer et al. [110] did for ATP.

After acquiring ^{31}P data on a dCDP sample in the presence of a biomolecule and a known concentration of [Mg^{2+}] or [Ca^{2+}], the α-phosphate chemical shift is first used (Figure 5.2a, E.3-E.6) in determining the $[M^{2+}_{Free}]$ by following the appropriate pH and temperature titration curve (Figure 5.2b). This concentration along with the $[Mg^{2+}_{total}]$ and [dCDP] is then used in Equations 2 and 3 to determine the F_b and the $[Mg^{2+}_{bound}]$ by the biomolecule of interest:

$$F_b = 1 - \frac{1}{[M^{2+}_{total}]}[[M^{2+}_{Free}] + \frac{\delta_0 - \delta_c}{\delta_0 - \delta_\infty} * [dCDP]] \quad (2)$$

$$[M^{2+}_{bound}] = [M^{2+}_{total}] * F_b \quad (3)$$

where F_b is fraction of metal bound by the biomolecule.

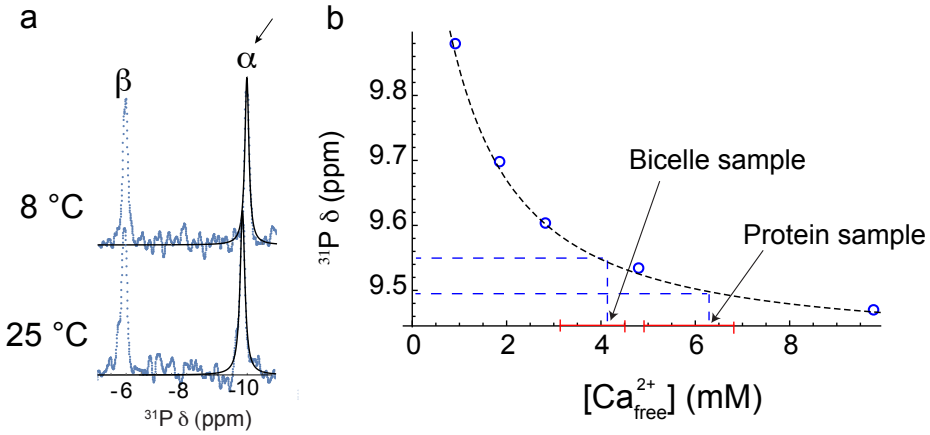

Figure 5.2: (a) ^{31}P spectra of dCDP in the presence of $\beta\gamma$-crystallin and 7 mM Ca^{2+} showing differences in the α- phosphate chemical shifts at two different temperatures and neutral pH. The differences in the chemical shifts correspond to differences in the free divalent ion concentration in solution as interpolated using the method shown in (b) for 8 ° C: e.g. 5.7 ± 1.0 mM of free plus bound Ca^{2+} to dCDP out of 7 mM added in the protein sample (shown by the arrow) implying that 1.1 ± 1.0 mM was bound by the protein. Using this method, the DNA bound 2.3 ± 0.7 mM Mg^{2+}, bicelles bound 7.7 ± 0.3 mM Mg^{2+}, and the bicelles bound 6.0 ± 0.7 mM Ca^{2+} at 8 ° C.

Using the titration curves from (Figure 5.1) and Equations 1, 2 and 3, we determined the bound concentration of divalent metal ions in a set of model systems. To account for divalent metals initially present in the biomolecular samples, EDTA was added to each sample prior to addition of divalent metals and ^{31}P spectra were acquired to compare with spectra in the absence EDTA. As was the case for the dCDP sample, the change in the ^{31}P chemical shift was within experimental error, indicating negligible initial concentrations of divalent cations. EDTA was also added to a protein sample to test for residual divalent metal ions and ^{15}N-^{1}H HSQC spectra show that there were no peak shifts in the presence and absence of EDTA (Figure E.2). Additionally, the amount of divalent metal ions initially present in the sample can be minimized by adding EDTA before protein purification or using EDTA-containing denaturing conditions for nucleic acid purification and followed by dialysis to ensure that no

divalent metal ions or EDTA are left in the sample. The Dickerson dodecamer DNA [111], [d(CGCGAATTCGCG)]2, at a concentration of 1.5 mM bound Mg^{2+} at slightly more than a 1:2 stoichiometric ratio (2.3 ± 0.6 mM) at 25 °C, and 2.4 ± 0.6 mM Mg^{2+} at 8 °C. The 1.5 Mg^{2+} ions bound to the dodecamer in solution at 25 °C are likely to bind to the major grooves in agreement with a crystal structure solved at low [Mg^{2+}] [112]. As expected, these solution measurements at low salt concentration differ from a crystal structure solved in the presence of higher salt, where 13 Mg^{2+} ions were bound [113]. A DLPC/DHPC/cholesterol sulfate bicelle mixture (DLPC/DHPC/CS, q=3.5, 15 % w/v) bound at 8 °C a large fraction (7.7 ± 0.3 mM) of the 10 mM Mg^{2+} added to the sample. When 10 mM Ca^{2+} was added to a bicelle sample, the sample bound 6.0 ± 0.7 mM Ca^{2+} at 8 °C, slightly less than the amount of Mg^{2+} bound by the same mixture. The differences in binding of DLPC/DHPC/CS to Mg^{2+} and Ca^{2+} at low temperatures are consistent with Mg^{2+} having a tighter binding to phosphates as observed from its lower $K_{1/2}$ value than that of Ca^{2+} in dCDP. A calcium-binding $\beta\gamma$-crystallin protein from *Ciona intestinalis* (2 mM) bound 2.8 ± 0.8 mM Ca^{2+} in the presence of 7 mM total Ca^{2+} at 25 °C, corresponding to 1.4 divalent metal ions per protein, and at 8 °C 0.6 Ca^{2+} ions bound each protein. The X-ray crystal structure of this tunicate $\beta\gamma$-crystallin revealed two Ca^{2+} binding sites per protein [3]. Our results indicate that these two binding sites are not fully occupied in solution even at 25 °C at this lower salt concentration. These results are tabulated in Table 5.2 for Mg^{2+} and Ca^{2+}.

Table 5.2: Macromolecule- bound [Mg^{2+}] and [Ca^{2+}] at 25 °C and 8 °C calculated from the ^{31}P chemical shifts of dCDP.

	Temp (°C)	$\delta^{31}P$(ppm)	$[M^{2+}_{Free}]$ from $\delta^{31}P$ of dCDP (mM)	Bound $[M^{2+}]$ (mM)
12 bp DNA and 6 mM Mg^{2+}	25.0	9.41	3.3±0.07	2.4±0.7
	8.0	9.54	3.4±0.6	2.3±0.7
Bicelles and 10 mM Mg^{2+}	25.0	9.58	2.0±0.3	7.7±0.3
$\beta\gamma$-crystallin and 7 mM Ca^{2+}	25.0	9.34	4.0±0.7	2.8±0.8
	8.0	9.49	5.7±1.0	1.1±1.0
Bicelles and 10 mM Ca^{2+}	8.0	9.55	3.8±0.7	6.0±0.7

Some of the plots in (Figure 5.1) plateau at divalent metal ion concentrations > 10 mM, indicating saturation. In this regime, the error in the concentration measurements is substantially high, making it difficult to extrapolate the exact concentrations of the bound metal ions, under these conditions. Similarly, large errors are obtained below 1 mM. Given that most in situ NMR studies of biological macromolecules focus on metal ion concentrations in the range of 1 - 10 mM, this is not problematic for typical applications, however, it is useful to place upper and lower bounds on the utility of dCDP for this application. Errors for metal concentrations that are the focus of this study are also shown in Table 5.2. In order to obtain divalent metal ion concentrations below 1 mM, a stronger metal ion chelator must be used such a fluorescent dye. Similarly a weaker chelating agent could be used above 10 mM if such measurements are desired.

In conclusion, we have demonstrated a method for determining the bound [Mg^{2+}] and [Ca^{2+}] in situ within a 1-10 mM concentration range for complex biomolecular NMR samples, including highly concentrated lipids, using ^{31}P NMR of an internal dCDP standard. This method is suitable under conditions where the type, and total amount of the metal ion added to the sample is known. We determined the bound [Mg^{2+}] and [Ca^{2+}] in a DNA dodecamer, a DLPC/DHPC/CS bicelle mixture and a *Ci*-$\beta\gamma$-crystallin protein sample, each containing a known total concentration of their respective divalent ion. From these findings, we conclude that the DNA dodecamer binds at least a single Mg^{2+} per duplex in solution and that the DLPC/DHPC/CS bicelles bind divalent ions at cold temperatures, consistent with the observation that ion binding is temperature-dependent [89]. We further show that at least one of the Ca^{2+} binding sites in the tunicate $\beta\gamma$-crystallin protein appears to be fully occupied in solution at room temperature. Because this method is minimally invasive and uses standard NMR instrumentation, it is applicable to a wide range of macromolecular samples used for NMR structural studies that require divalent metal ions.

Bibliography

[1] R. P. Barnwal, M. K. Jobby, Y. Sharma, and K. V. R. Chary. NMR assignment of M-crystallin: a novel Ca^{2+} binding protein of the $\beta\gamma$-crystallin superfamily from *Methanosarcina acetivorans*. *J. Biomol. NMR*, 36:32–32, 2006.

[2] G. Wistow, L. Summers, and T. Blundell. *Myxococcus xanthus* spore coat protein S may have a similar structure to vertebrate lens $\beta\gamma$-crystallins. *Nature*, 315:771–773, 1985.

[3] S. M. Shimeld, A. G. Purkiss, R. P. Dirks, O. A. Bateman, C. Slingsby, and N. H. Lubsen. Urochordate $\beta\gamma$-crystallin and the evolutionary origin of the vertebrate eye lens. *Curr. Biol.*, 15:1684–1689, 2005.

[4] A. Krasko, I. M Müller, and W. E. G. Müller. Evolutionary relationships of the metazoan $\beta\gamma$-crystallins, including that from the marine sponge *Geodia cydonium*. *Proc. Royal Soc. B*, 264:1077–1084, 1997.

[5] S. K. Suman, A. Mishra, L. Yeramala, I. Das Rastogi, and Y. Sharma. Disability for function: loss of Ca^{2+}-binding is obligatory for fitness of mammalian $\beta\gamma$-crystallins. *Biochemistry*, 52:9047–9058, 2013.

[6] B. Rosinke, C. Renner, E. M. Mayr, R. Jaenicke, and T. A. Holak. Ca^{2+}-loaded spherulin 3a from *Physarum polycephalum* adopts the prototype gamma-crystallin fold in aqueous solution. *J. Mol. Biol.*, 271(4):645–655, 1997.

[7] A. Vergara, M. Grassi, F. Sica, E. Pizzo, G. D'Alessio, L. Mazzarella, and A. Merlino. A novel interdomain interface in crystallins: structural characterization of the $\beta\gamma$-crystallin from *Geodia cydonium* at 0.99 Å resolution. *Acta Crystallogr D: Biological Crystallography*, D69:960–967, 2013.

[8] N. J. Clout, M. Kretschmar, R. Jaenicke, and C. Slingsby. Crystal structure of the calcium-loaded spherulin 3a dimer sheds light on the evolution of the eye lens $\beta\gamma$-crystallin domain fold. *Structure*, 9(2):115–124, 2001.

[9] J. H. Hamill, E. Cota, C. Chothia, and J. Clarke. Conservation of folding and stability within a protein family: the tyrosine corner as an evolutionary cul-de-sac. *J. Mol. Biol.*, 295:641–649, 2000.

[10] M. K. Jobby and Y. Sharma. Calcium-binding crystallins from *Yersinia pestis* - characterization of two single $\beta\gamma$-crystallin domains of a putative exported protein. *J. of Biol. Chem.*, 280(2):1209–1216, 2005.

[11] M. Kretschmar, E-N. Mayr, and R. Jaenicke. Kinetic and thermodynamic stabilization of the $\beta\gamma$-crystallin homolog spherulin 3a from *Physarum polycephalum* by calcium binding. *J. Mol. Biol.*, 289:701–705, 1999.

[12] M. Wenk and R. Jaenicke. Calorimetric analysis of the Ca^{2+}-binding $\beta\gamma$-crystallin homolog protein s from *Myxococcus xanthus*: intrinsic stability and mutual stabilization of domains. *J. Mol. Biol.*, 293:117–124, 1999.

[13] R.P. Barnwal, M. K. Jobby, K. M. Devi, Y Sharma, and K. V. Chary. Solution structure and calcium-binding properties of M-crystallin, a primordial $\beta\gamma$-crystallin from archaea. *J. Mol. Biol.*, 386:675–689, 2009.

[14] M. K. Jobby and Y. Sharma. Caulollins from *Caulobacter crescentus*, a pair of partially unstructured proteins of $\beta\gamma$-crystallin superfamily, gain structure upon binding calcium. *Biochemistry*, 46,:12298–12307, 2007.

[15] A. K. Srivastava and K. V. R. Chary. Conformational heterogeneity and dynamics in a $\beta\gamma$-crystallin from *Hahella chejuensis*. *Biophys. Chem.*, 157(1-3):7–15, 2011.

[16] C. Slingsby, G. J. Winstow, and A. R. Clark. Evolution of crystallins for a role in the vertebrate eye lens. *Protein Sci.*, 22:367–380, 2013.

[17] G. Wistow. Lens crystallins: gene recruitment and evolutionary dynamism. *Trends Biochem. Sci.*, 18(8):301–306, 1993.

[18] C. N. Kingsley, J. Bierma, V. Pham, and R.W. Martin. The γS-crystallin proteins from the antarctic nototheniid toothfish: a model system for investigating differential resistance to chemical and thermal denaturation. *J. Phys. Chem. B*, 118(47):13544—13553, 2014.

[19] B. Rajini, P. Shridas, C. S. Sundari, D. Muralidhar, S. Chandani, F. Thomas, and Y. Sharma. Calcium binding properties of gamma crystallin: Calcium ion binds at the greek key $\beta\gamma$-crystallin fold. *J. Biol. Chem.*, 276:38464–38471, 2001.

[20] F. W. Studier. Protein production by auto-induction in high-density shaking cultures. *Protein Expres. Purif.*, 41:207–234, 2005.

[21] W. D. Brubaker and R. W. Martin. ^{1}H, ^{13}C, and ^{15}N assignments of wild-type human γS-crystallin and its cataract-related variant γS-G18V. *Biomolec. NMR Assign.*, 6:63–67, 2011.

[22] N. A. Morjana, B. J. McKeone, and Gilbert H. F. Guanidine hydrochloride stabilization of a partially unfolded intermediate during the reversible denaturation of protein disulfide isomerase. *Proc. Natl. Acad. Sci. USA*, 90:2107–2111, 1993.

[23] P. Aravind, A. Mishra, S. K. Suman, M. K. Jobby, R. Sankaranarayanan, and Y. Sharma. The $\beta\gamma$-crystallin superfamily contains a universal motif for binding calcium. *Biochemistry*, 48(51):12180–12190, 2009.

[24] G. Duncan and T.J. Jacob. Calcium and the physiology of cataract. *Ciba Foundation Symposium*, 106:132–152, 1984.

[25] S. S. Srivastava, A. Mishra, B. Krishnan, and Y. Sharma. Ca^{2+}-binding motif of $\beta\gamma$-crystallins. *J. Biol. Chem.*, 289:10958–10966, 2014.

[26] S. K. Suman, A. Mishra, D. Ravindra, L. Yeramala, and Y Sharma. Evolutionary remodeling of $\beta\gamma$-crystallins for domain stability at cost of Ca^{2+} binding. *J. Biol. Chem.*, 286:43891–43901, 2011.

[27] C. Giancola, E. Pizzo, A. Di Maro, M. V. Cubellis, and G. D'Alessio. Preparation and characterization of geodin. *FEBS Journal*, 272:1023–1035, 2005.

[28] B.J. Bennion and V. Daggett. The molecular basis for the chemical denaturation of proteins by urea. *Proc. Natl. Acad. Sci. USA*, 100:5142–5147, 2003.

[29] N. Kozlyuk, S. Sengupta, J. Bierma, and R. W. Martin. Calcium binding dramatically stabilizes an ancestral crystallin fold in tunicate $\beta\gamma$-crystallin. *Biochemistry*, 55:6961–6968, 2016.

[30] S. G. Dove and M. J. Kingsford. Use of otoliths and eye lenses for measuring trace-metal incorporation in fishes: a biogeographic study. *Marine Biol.*, 130:377–387, 1998.

[31] T. L. Blundell and J. A. Jenkins. The binding of heavy metals to proteins. *Chem. Soc. Rev.*, 6:139–171, 1977.

[32] L. Quintanar, J. A. Domínguez-Calva, E. Serebryany, L. Rivillas-Acevedo, Haase-Pettingell. C., C. Amero, and J. A. King. Copper and zinc ions specifically promote nonamyloid aggregation of the highly stable human γ-D crystallin. *ACS Chem. Biol.*, 11:263–272, 2016.

[33] K. S. Ghosh, A. Pande, and J. Pande. Binding of gamma crystallin substrate prevents the binding of copper and zinc ions to the molecular chaperone alpha crystallin. *Biochemistry*, 50:3279–3281, 2011.

[34] S. Liemann and R. Glockshuber. Influence of amino acid substituions related to inherited human prion diseases on the thermodynamic stability of the cellular prion protein. *Biochemistry*, 38:3258–3267, 1999.

[35] W. D. Brubaker, J. A. Freites, K. J. Golchert, R. A. Shapiro, V. Morikis, D. J. Tobias, and R. W. Martin. Separating instability from aggregation propensity in γS-crystallin variants. *Biophys. J.*, 100(2):498–506, 2011.

[36] E. Y. Chi, S. Krishnan, T. W. Randolph, and J. F. Carpenter. Physical stability of proteins in aqueous solution: Mechanism and driving forces in nonnative protein aggregation. *Pharm. Res.*, 20:1325–1336, 2003.

[37] B. S. Kendrick, J. L. Cleland, X. Lam, T. Nguyen, T. W. Randolph, M. C. Manning, and J. F. Carpenter. Aggregation of recombinant human interferon gamma: Kinetics and structural transitions. *J. Pharm. Sci.*, 87:1069–1076, 1998.

[38] J. N. Webb, S. D. Webb, J. L. Cleland, J. F. Carpenter, and T. W. Randolph. Partial molar volume, surface area, hydration changes for equilibrium unfolding and formation of aggregation transition state: High-pressure and cosolute studies on recombinant human ifn-γ. *Proc. Natl. Acad. Sci. USA*, 98:7259–7264, 2001.

[39] B. S. Kendrick, J. F. Carpenter, J. L. Cleland, and T. W. Randolph. A transient expansion of the native state precedes aggregation of recombinant human interferon-γ. *Proc. Natl. Acad. Sci. USA*, 95:14142–14146, 1998.

[40] S. Krishnan, E. Y. Chi, J. N. Webb, B. S. Chang, D. Shan, M. Goldenberg, M. C. Manning, T. W. Randolph, and J. F. Carpenter. Aggregation of granulocyte colony stimulating factor under physiological conditions: Characterization and thermodynamic inhibition. *Biochemistry*, 41:6422–6431, 2002.

[41] M. Nara, M. Tanokura, T. Yamamoto, and M. Tasumi. A comparative study of the binding effects of Mg^{2+}, Ca^{2+}, Sr^{2+}, and Cd^{2+} on calmodulin by fourier-transform infrared spectroscopy. *Biospectroscopy*, 1:47–54, 1995.

[42] Y. Cheng, S. M. Sequeira, L. Malinina, V. Tereshko, T. H. Sollner, and D. J. Patel. Crystallographic identification of Ca^{2+} and Sr^{2+} coordination sites in synaptotagmin i c_2b domain. *Protein Sci.*, 13:2665–2672, 2004.

[43] P. M. Colman, J. N. Jansonius, and B. W. Matthews. The structure of thermolysin: an electron density map at 2-3 Å resolution. *J. Mol. Biol.*, 70:701–724, 1972.

[44] J. P. Glusker, A. K. Katz, and C. W. Bock. Metal ions in biological systems. *Rigaku J.*, 16:8–17, 1999.

[45] A. K. Katz, J. P. Glusker, S. A. Beebe, and C. W. Bock. Calcium ion coordination: a comparison with that of beryllium, magnesium, and zinc. *J. Am. Chem. Soc.*, 118:5752–5763, 1996.

[46] L. Rulisek and J. Vondrasek. Coordination geometries of selected transition metal ions (Co^{2+}, Ni^{2+}, Cu^{2+}, Zn^{2+}, Cd^{2+}, and Hg^{2+}) in metalloproteins. *J. Inorg. Biochem.*, 71:115–127, 1998.

[47] T. A. Khrustaleva. Secondary structure preferences of Mn^{2+} binding sites in bacterial proteins. *Adv. Bioinformatics*, pages 1–14, 2014.

[48] C. W. Bock, A. Kaufman, and J. P. Glusker. *Inorg. Chem.*, 33:419–427, 1994.

[49] J. H. Prestegard, H. M. Al-Hashimi, and J. R. Tolman. Nmr structures of biomolecules using field oriented media and residual dipolar couplings. *Q. Rev. Biophys.*, 33:371–424, 2000.

[50] D. D. Boehr, R. Nussinov, and P. E. Wright. The role of dynamic conformational ensembles in biomolecular recognition. *Nat. Chem. Biol.*, pages 1–8, 2009.

[51] A. G. Palmer III. Nmr probes of molecular dynamics: overview and comparison with other techniques. *Annu. Rev. Biophys. Biomol. Struct.*, 30:129–155, 2001.

[52] K. Wuthrich and G. Wagner. *FEBS Lett.*, 50:265–268, 1975.

[53] R. Hetzel, K. Wuthrich, J. Deisenhofer, and R. Huber. *Biophys. Struct. Mech.*, 2:159–180, 1976.

[54] B. R. Gelin and M. Karplus. *Proc. Natl. Acad. Sci. USA*, 72:2002–2006, 1975.

[55] K. Wuthrich. Nmr-this other method for protein and nucleic acid structure determination. *Acta Cryst.*, D51:249–270, 1995.

[56] M. Sattler, J. Schleucher, and C. Griesinger. Heteronuclear multidimensional nmr experiments for the structure determination of proteins in solution employing pulsed field gradients. *Prog. Nucl. Magn. Reson. Spectrosc.*, 34:93–158, 1999.

[57] L. E. Kay, M. Ikura, R. Tschudin, and A. Bax. Three-dimensional triple-resonance nmr spectroscopy of isotopically enriched proteins. *J. Magn. Reson.*, 89:496–514, 1990.

[58] V. A. Higman. Protein nmr spectrum descriptions, 2012.

[59] A. Bax and M. Ikura. An efficient 3D nmr technique for correlating the proton and ^{15}N backbone amide resonances with the α-carbon of the preceding residue in uniformly $^{15}N/^{13}$C enriched proteins. *J. Biomol. NMR*, 1:99–104, 1991.

[60] R. T. Clubb, V. Thanabal, and G. Wagner. A constant-time three dimensional triple-resonance pulse scheme to correlate intraresidue $^{1}H^{N}$, ^{15}N, and ^{13}C' chemical shifts in ^{15}N-^{13}C-labeled proteins. *J. Magn. Reson.*, 97:213–217, 1992.

[61] S. Grzesiek and A. Bax. Correlating backbone amide and side chain resonances in larger proteins by multiple relayed triple resonance nmr. *J. Am. Chem. Soc.*, 114:6291–6293, 1992.

[62] S. Grzesiek and A. Bax. An efficient experiment for sequential backbone assignment of medium-sized isotopically enriched proteins. *J. Magn. Reson.*, 99:201–207, 1992.

[63] S. Grzesiek, J. Anglister, and A. Bax. Correlation of backbone amide and aliphatic side-chain resonances $^{13}C/^{15}N$-enriched proteins by isotropic mixing of ^{13}C magnetization. *J. Magn. Reson.*, 101:114–119, 1993.

[64] A. Bax, G. M. Clore, P. C. Driscoll, A. M. Gronenborn, M. Ikura, and L. E. Kay. Practical aspects of proton-cabron-carbon-proton three-dimensional correlation spectroscopy of ^{13}C-labeled proteins. *J. Magn. Reson.*, 87:620–627, 1990.

[65] L. E. Kay, M. Ikura, and A. Bax. Proton-proton correlation via carbon-carbon couplings: a three-dimensional nmr approach for the assignment of aliphatic resonances in proteins labeled with carbon-13. *J. Am. Chem. Soc.*, 112:888–889, 1990.

[66] A. Bax, G. M. Clore, and A. M. Gronenborn. ^{1}H-^{1}H correlation via isotropic mixing of the ^{13}C magnetization, a new three-dimensional approach for assigning ^{1}H and ^{13}C spectra of ^{13}C-enriched proteins. *J. Magn. Reson.*, 88:425–431, 1990.

[67] E. R. P. Zuiderweg and S. W. Fesik. Heteronuclear three-dimensional nmr spectroscopy of the inflammatory protein c5a. *Biochemistry*, 28:2387–2391, 1989.

[68] J. Otlewski and T. Cierpicki. Amide proton temperature coefficients as hydrogen bond indicators in proteins. *J. Biomol. NMR*, 21:249–261, 2001.

[69] Z. Wu, F. Delaglio, N. Tjandra, V. B. Zhurkin, and A. Bax. Overall structure and sugar dynamics of a dna dodecamer from homo- and heteronuclear dipolar couplings and ^{31}P chemical shift anisotropy. *J. Biomol. NMR*, 26:297–315, 2003.

[70] H. Wang, M. Eberstadt, E. T. Olejniczak, R. P. Meadows, and S. W. Fesik. A liquid crystalline medium for measuring residual dipolar couplings over a tide tange of temperatures. *J. Biomol. NMR*, 12:443–446, 1998.

[71] A. Bax. Weak alignment offers new nmr opportunities to study protein structure and dynamics. *Protein Sci.*, 12:1–16, 2003.

[72] M. W. F. Fischer, J. A. Losonczi, J. L. Weaver, and J. H. Prestegard. Domain orientation and dynamics in multidomain proteins from residual dipolar couplings. *Biochemistry*, 38:9013–9022, 1999.

[73] J. A. Losonczi and J. H. Prestegard. Improved dilute bicelle solutions for high-resolution nmr of biological macromolecules. *J. Biomol. NMR*, 12:447–451, 1998.

[74] E. Brunner. Residual dipolar couplings in protein nmr. *Concepts Magn. Reson.*, 13:238–259, 2001.

[75] N. Tjandra, J. G. Omichinski, A. M. Gronenborn, G. M. Clore, and A. Bax. Use of dipolar H-1-N-15 and H-1-C-13 couplings in the structure determination of magnetically oriented macromolecules in solution. *Nat. Struct. Biol.*, 4:732–738, 1997.

[76] M. Ruckert and G. Otting. Alignment of biological macromolecules in novel nonionic liquid crystalline media for nmr experiments. *J. Am. Chem. Soc.*, 122:7793–7797, 2000.

[77] C. R. Sanders and J. P. Schwonek. Characterization of magnetically orientable bilayers in mixtures of dihexanoylphosphatidylcholine and dimyristoylphosphatidylcholine by solid-state nmr. *Biochemistry*, 31:8898–8905, 1992.

[78] R. A. Shapiro, A. J. Brindley, and R. W. Martin. Thermal stabilization of DMPC/DHPC bicelles by addition of cholesterol sulfate. *J. Am. Chem. Soc.*, 132:11406–11407, 2010.

[79] K. Yamamoto, P. Pearcy, and A. Ramamoorthy. Bicelles exhibiting magnetic alignment for a broader range of temperatures: a solid-state nmr study. *Langmuir*, 30:1622–1629, 2014.

[80] M.-P. Nieh, V. A. Raghunathan, C. J. Glinka, T. A. Harroun, G. Pabst, and J. Katsaras. Magnetically alignable phase of phospholipid "bicelle" mixtures is a chiral nematic made up of wormlike micelles. *Langmuir*, 20:7893–7897, 2004.

[81] T. A. Harroun, M. Koslowsky, M.-P. Nieh, C.-F. de Lannoy, and V. A. Raghunathan. Comprehensive examination of mesophases formed by DMPC and DHPC mixtures. *Langmuir*, 21:5356–5361, 2005.

[82] K. Yamamoto, M. Gildenberg, S. Ahuja, S.-C. Im, P. Pearcy, L. Waskell, and A. Ramamoorthy. Probing the transmembrane structure and topology of microsomal cytochrome-p450 by solid-state nmr on temperature-resistant bicelles. *Sci. Rep.*, 3:1–6, 2013.

[83] M. Ottiger, F. Delaglio, and A. Bax. Measurement of J and dipolar couplings from simplified two-dimensional nmr spectra. *J. Magn. Reson.*, 131:373–378, 1998.

[84] J. Cavanagh, W. J. Fairbrother, A. G. Palmer III, M. Rance, and N. J. Skelton. *Principles and practice of protein NMR spectroscopy.* Elsevier, 2nd edition, 2007.

[85] A. Sreedhara and J. A. Cowan. Structural and catalytic roles for divalent magnesium in nucleic acid biochemistry. *BioMetals*, 15:211–223, 2002.

[86] C. B. Black, H.-W. Huang, and J. A. Cowan. Biological coordination chemistry of magnesium, sodium, and potassium ions. Protein and nucleotide binding domains. *Coord. Rev.*, 135/136:165–202, 1994.

[87] N. J. Riccitelli, E. Delwart, and A. Luptàk. Identification of minimal HDV-like ribozymes with unique divalent metal ion dependence in the human microbiome. *Biochemistry*, 53:1616–1626, 2014.

[88] D. E. Clapham. Calcium signaling. *Cell*, 80:259–268, 1995.

[89] A. J. Brindley and R. W. Martin. Effect of divalent cations on DMPC/DHPC bicelle formation and alignment. *Langmuir*, 28:7788–7796, 2012.

[90] T. Arnold, A. abd Labrot, R. Oda, and E. J. Dufourc. Cation modulation of bicelle size and magnetic alignment as revealed by solid-state nmr and electron microscopy. *Biophys. J.*, 83:2667–2680, 2002.

[91] S. Faham and J. U. Bowie. Bicelle crystallization: a new method for crystallizing memebrane proteins yields a monomeric bacteriorhodopsin structure. *J. Mol. Biol.*, 316:1–6, 2002.

[92] K. Oxenoid and J. J. Chou. The structure of phospholamban pentamer reveals a channel-like architecture in membranes. *Proc. Natl. Acad. Sci. USA*, 102:10870–10875, 2005.

[93] N. J. Traaseth, L. Shi, R. Verardi, D. G. Mullen, G. Barany, and G. Veglia. Structure and topology of monomeric phospholamban in lipid membranes determined by a hybrid solution and solid-state nmr approach. *Proc. Natl. Acad. Sci. USA*, 106:10165–10170, 2009.

[94] J. Turnay, N. Olmo, M. Gasset, I. Iloro, J. L. R. Arrondo, and M. A. Lizarbe. Calcium-dependent conformational rearrangements and protein stability in chicken annexin a5. *Biophys. J.*, 83:2280–2291, 2002.

[95] P. Pathuri, L. Vogeley, and H. Luecke. Crystal strcuture of metastasis-associated protein S100A4 in the active calcium-bound form. *J. Mol. Biol.*, 383:62–77, 2008.

[96] R. E. London. Methods of measurement of intracellular magnesium: Nmr and fluorescence. *Annu. Rev. Physiol.*, 53:241–258, 1991.

[97] R. K. Gupta, J. L. Benovic, and Z. B. Rose. The determination of the free magnesium level in the human red blood cell by ^{31}P nmr. *J. Biol. Chem.*, 253:6172–6176, 1978.

[98] R. K. Gupta and W. D. Yushok. The determination of the magnesium level in the human red blood cell by ^{31}P nmr. *Proc. Natl. Acad. Sci. USA*, 77:2487–2491, 1980.

[99] R. K. Gupta and R. D. Moore. ^{31}P nmr studies of intracellular free Mg^{2+} in intact frog skeletal muscle. *J. Biol. Chem.*, 255:3987–3993, 1980.

[100] L. Garfinkel and D. Garfinkel. Calculation of free-Mg^{2+} concentration in adenosine 5'-triphosphate containing solutions *in vitro* and*in vivo*. *Biochemistry*, 23:3547–3552, 1984.

[101] F. J. Alvarez-Leefmans, F. Giraldez, and S. M. Gamino. Intracellular free magnesium in excitable cells: its measurement and its biologic significance. *Can. J. Physiol. Pharmacol.*, 65:915–925, 1987.

[102] R. G. Shulman, H. Sternlicht, and B. J. Wyluda. Study of metal-ion binding to nucleic acids by ^{31}P nuclear magnetic resonance. *J. Chem. Phys.*, 43:3116–3122, 1965.

[103] T.-D. Son, M. Roux, and M. Ellenberger. Interaction of Mg^{2+} ions with nucleoside triphosphates by phosphorus magnetic resonance spectroscopy. *Nucleic Acids Res.*, 2:1101–1110, 1975.

[104] M. Cohn and T. R. Hughes Jr. Nuclear magnetic resonance spectra of adenosine di- and triphosphate. II. Effect of complexing with divalent metal ions. *J. Biol. Chem.*, 237:176–181, 1962.

[105] C. M. Frey and J. E. Stuehr. Interactions of divalent metal ions with inorganic and nucleotide phosphates. I. Thermodynamics. *J. Am. Chem. Soc.*, 94:8898–8904, 1972.

[106] M. M. T. Khan and A. E. Martell. Thermodynamic quantities associated with the interactions of adenosine triphoshate with metal ions. *J. Am. Chem. Soc.*, 88:668–671, 1966.

[107] M. M. T. Khan and A. E. Martell. Thermodynamic quantities associated with the interaction of adenosinediphosphoric and adeno-sinemonophosphoric acids with metal ions. *J. Am. Chem. Soc.*, 89:5585–5590, 1967.

[108] A. V. Hill. The possible effects of the aggregation of the molecules of haemoglobin on its dissociation curves. *J. Physiol.*, 40, 1910.

[109] N. Gresh. Intermolecular chelation of two serine phosphates by Ca^{2+} and Mg^{2+}. a theoretical structural investigation. *Biochimica et biophysica acta*, 597:345–357, 1980.

[110] G. M. Sontheimer, W. Kuhn, and H. R. Kalbitzer. Observation of Mg^{2+}. ATP and uncomplexed ATP in slow exchange by ^{31}P-NMR at high magnetic fields. *Biochem. Biophys. Res. Comm.*, 134:1379–1386, 1986.

[111] H. R. Drew, R. M. Wing, T. Takano, C. Broka, S. Tanaka, K. Itakura, and R. E. Dickerson. Structure of a B-DNA dodecamer: conformation and dynamics. *Proc. Natl. Acad. Sci. USA*, 78:2179–2183, 1981.

[112] X. Shui, L. MacFail-Isom, G. G. Hu, and L. D. Williams. The B-DNA dodecamer at high resolution reveals a spine of water on sodium. *Biochemistry*, 37:8341–8355, 1998.

[113] G. Minason, V. Tereshko, and M. Egli. Atomic-resolution crystal structures of B-DNA reveal specific influences of divalent metal ions on conformation and packing. *J. Mol. Biol.*, 291:83–99, 1999.

Appendix A

1: Supplementary material for calcium binding dramatically stabilizes an ancestral crystallin fold in tunicate $\beta\gamma$-crystallin.

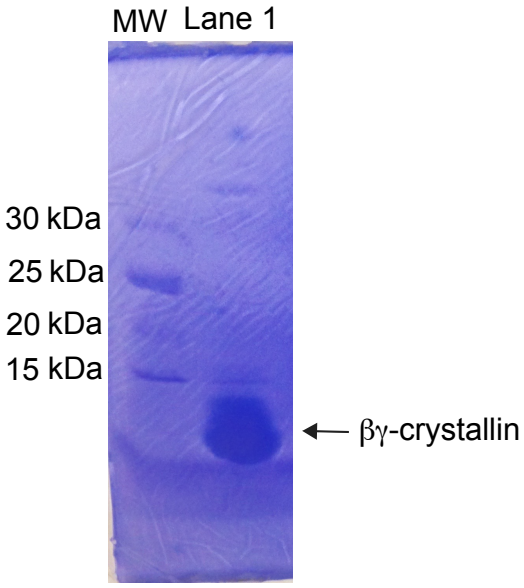

Figure A.1: SDS PAGE of *Ci*-$\beta\gamma$-crystallin protein showing the molecular weight marker and the purified protein in lane 1 of 9.057 kDa.

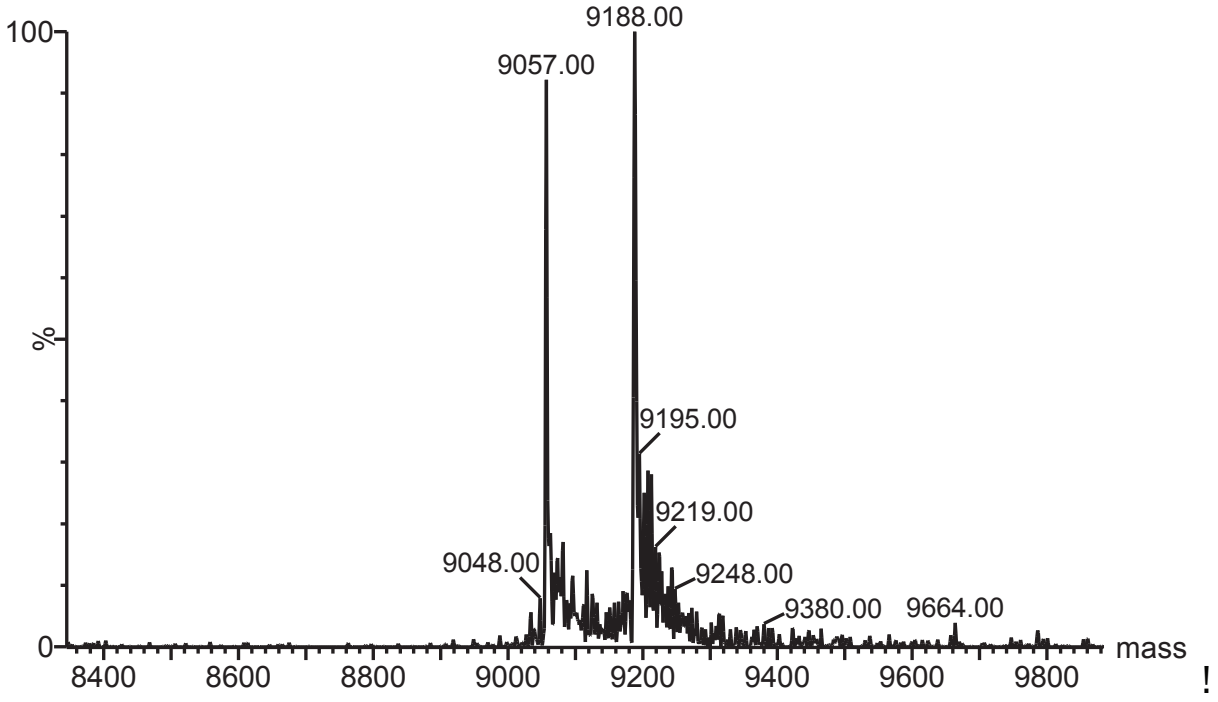

Figure A.2: ES MS of *Ci*-$\beta\gamma$-crystallin protein (9.057 kDa) shows that there is a mixture of the protein with and without the N-terminal initiator methionine, which is a common proteolytic post-translational modification

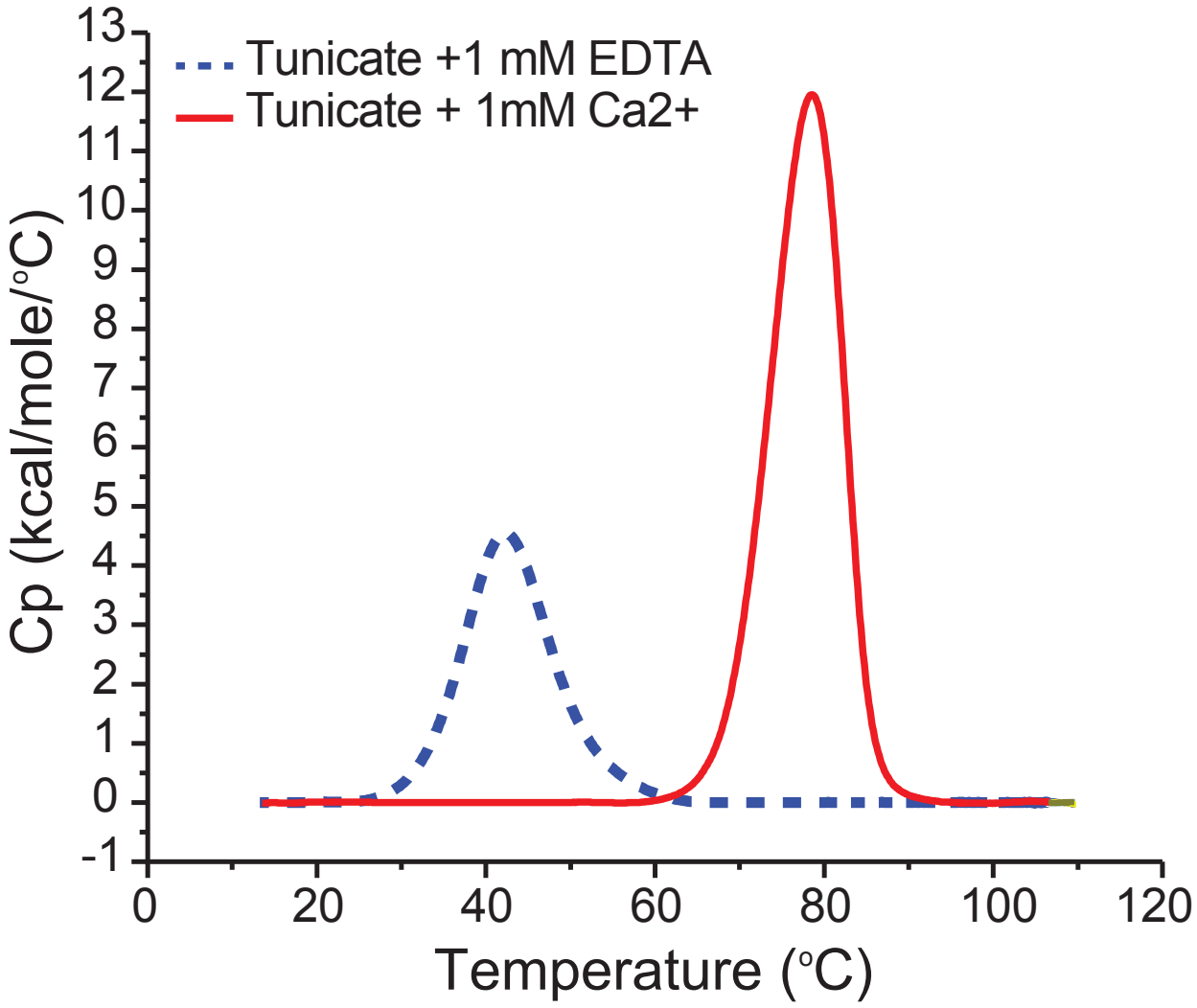

Figure A.3: DSC data for $\beta\gamma$-crystallin with 1 mM EDTA (blue) or 1 mM Ca^{2+} (red) in 10 mM MES (pH 7.1) showing transition temperatures of 42.3 and 77 °C respectively.

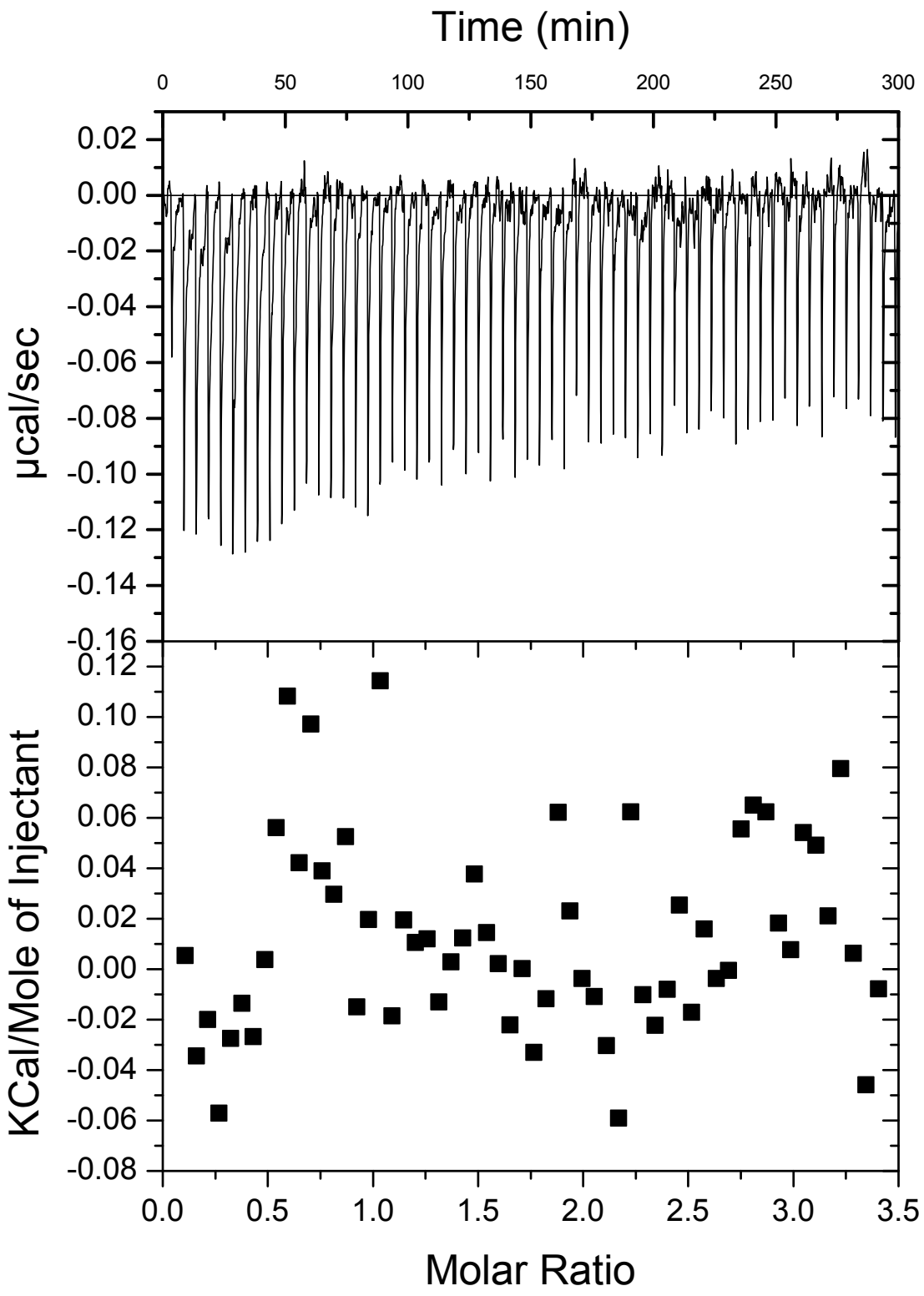

Figure A.4: Isotherm of human $\beta\gamma$-crystallin with 5 mM Ca^{2+} does not show any binding occurring.

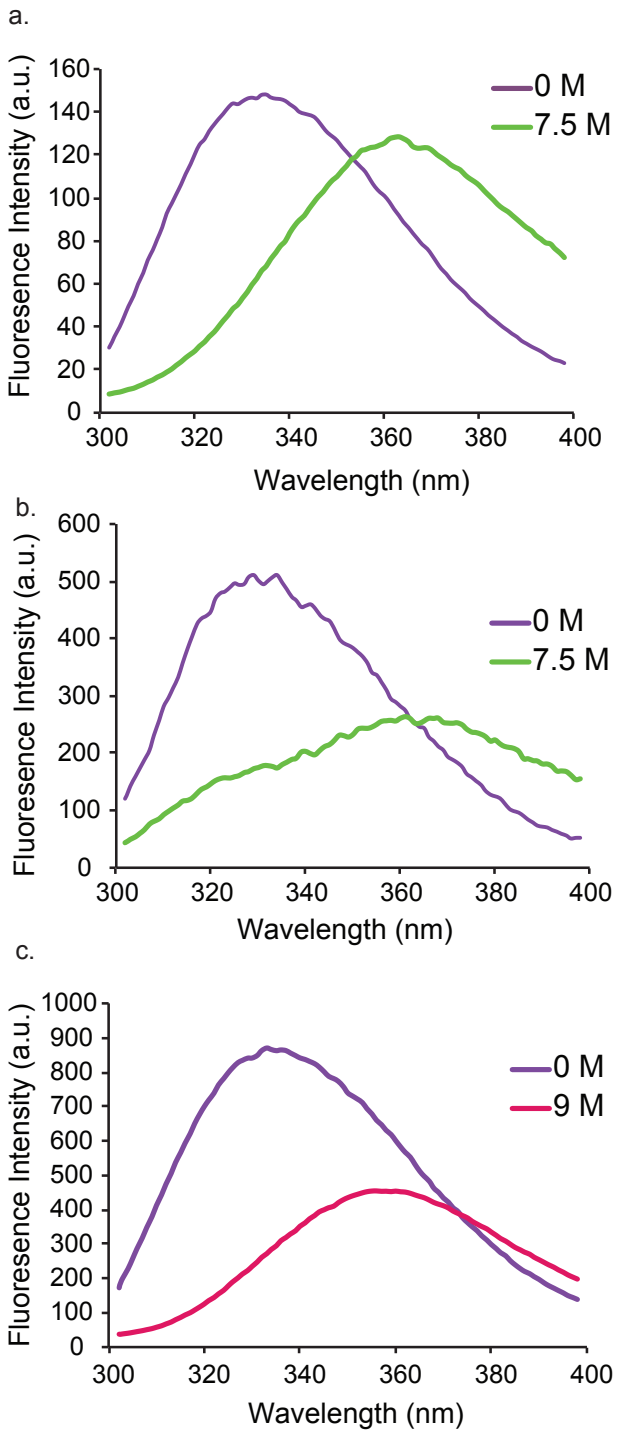

Figure A.5: Intrinsic tryptophan fluorescence spectra in the presence of 1 mM EDTA and GndHCl (a), 1 mM Ca^{2+} and GndHCl (b) and 1 mM EDTA and urea (c) show substantial peak shifts as the maximum concentration of denaturant is added to the protein. This peak shift of around 30 nm indicates protein unfolding in the presence of these chemical denaturants.

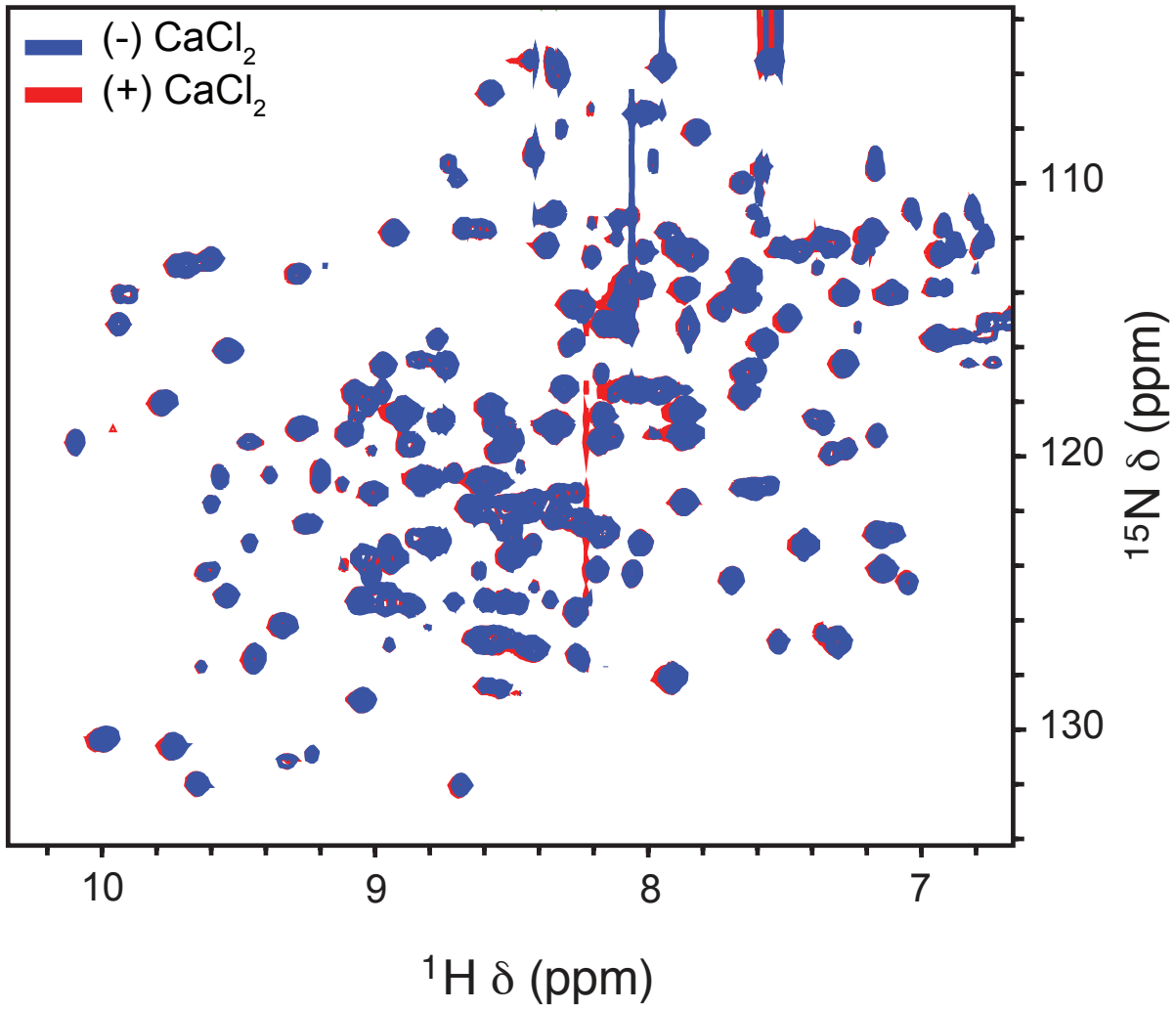

Figure A.6: ^{15}N-^{1}H HSQC spectrum of WT human $\beta\gamma$-crystallin in the absence (blue) and presence (red) of Ca^{2+} shows the absence of a conformational change occurring in the protein upon addition of Ca^{2+}.

A.1 ITC data analysis for sequential binding

A Mathematica® 9.0 program was written to fit the ITC data for sequential Ca^{2+} binding with floating stoichiometric parameters to the tunicate $\beta\gamma$-crystallin. The discussion that follows is adapted from Appendix IV of *ITC Data Analysis in Origin® Tutorial Guide, Version 5.0, October 1998* provided by MicroCal™, with necessary modifications.

For two-site sequential binding of ligand X to macromolecule M, the equilibria governing the binding are given by:

$$M + X \overset{K_1}{\rightleftharpoons} MX \quad ; \quad \Delta H_1 \tag{A.1}$$

$$MX + X \overset{K_2}{\rightleftharpoons} MX_2 \quad ; \quad \Delta H_2 \tag{A.2}$$

where, K_1 and K_2 are the two equilibrium constants, and ΔH_1 and ΔH_2 are the molar enthalpies of the binding events. The two equilibrium constants are expressed as:

$$K_1 = \frac{[MX]}{[M][X]} \; ; \quad K_2 = \frac{[MX_2]}{[MX][X]} \tag{A.3}$$

where, $[M]$, $[X]$, $[MX]$, and $[MX_2]$ are the concentrations of the free macromolecule, free ligand, macromolecule bound at one site, and macromolecule bound at two sites respectively.

The fraction of macromolecules that are unbound (F_0), bound only at one site (F_1), and bound at both sites (F_2) after completion of any injection of ligand can be expressed as:

$$F_0(i) = \frac{1}{P_i}, \quad F_1(i) = \frac{K_1[X]_i}{P_i}, \quad F_2(i) = \frac{K_1 K_2 [X]_i^2}{P_i} \tag{A.4}$$

where, $P_i = 1 + K_1[X]_i + K_1K_2[X]_i^2$. Here, the index i has been introduced to signify that the quantities are being calculated after completion of the i^{th} injection.

If $X_t(i)$ and $M_t(i)$ are the bulk concentrations of ligand and macromolecule respectively (calculated by Origin®, see Appendix I of *Tutorial Guide*) in the active volume (V_0) of the ITC cell after the i^{th} injection, then the concentration of free ligand $[X]_i$, is given by:

$$X_t(i) = [X]_i + M_t(i)(n_1 F_1(i) + n_2 F_2(i)) \tag{A.5}$$

where, n_1 and $(n_2 - n_1)$ are the number of binding sites of each kind available to the ligand per macromolecule. Using equation (4), equation (5) may be rearranged to a cubic equation in $[X]_i$ of the form:

$$[X]_i^3 + p_i[X]_i^2 + q_i[X]_i + r_i = 0 \tag{A.6}$$

where,

$$\begin{aligned} p_i &= \frac{1}{K_2} - X_t(i) + n_2 M_t(i) \\ q_i &= \frac{n_1 M_t(i) - X_t(i)}{K_2} + \frac{1}{K_1 K_2} \\ r_i &= -\frac{X_t(i)}{K_1 K_2} \end{aligned} \tag{A.7}$$

The normalized heat content of the solution in the active volume (V_0) after the completion of the i^{th} injection is given by:

$$Q(i) = \frac{M_t(i) V_0}{X_0 \Delta V} \left[n_1 F_1(i) \Delta H_1 + F_2(i) \left(n_1 \Delta H_1 + (n_2 - n_1) \Delta H_2 \right) \right] \tag{A.8}$$

where, X_0 is the concentration of the ligand in the syringe, and ΔV is the injection volume. The quantity that is of interest in the ITC fitting however is the *change* in normalized heat content from the completion of the $(i-1)^{th}$ injection to the completion of the i^{th} injection. A correction is necessary to account for the displaced volume upon injection of the ligand solution. The liquid in the displaced volume (ΔV) contributes about 50% as much heat as

an equivalent amount remaining in V_0. Thus the change in normalized heat content is given by:

$$\Delta Q(i) = Q(i) + \frac{\Delta V}{V_0}\left[\frac{Q(i) + Q(i-1)}{2}\right] - Q(i-1) \tag{A.9}$$

The Mathematica® fitting procedure involves making initial guesses for K_1, K_2, n_1, and n_2. Using these initial guesses, equation (6) is solved numerically for $[X]_i$ using the built-in Mathematica® function `NSolve` with the option `Reals` for returning only real valued roots. The $[X]_i$, K_1, K_2, n_1, and n_2, along with initial guesses for ΔH_1 and ΔH_2, are used in equations (4), (8), and (9) to evaluate the $\Delta Q(i)$. Thereafter, non-linear least squares fitting to the experimental data is performed using the built-in `NonlinearModelFit` routine to optimize the parameters K_1, K_2, n_1, n_2, ΔH_1, and ΔH_2. The optimized parameters are used to re-evaluate $[X]_i$ and the non-linear least squares fitting is performed again. This procedure is carried out iteratively until the fit parameters converge. The final $\Delta Q(i)$ obtained from equation (9) using optimized parameters are plotted against $X_t(i)/M_t(i)$ as is convention.

Appendix B

2:Supplementary material for effects of divalent cations on the structure of tunicate $\beta\gamma$-crystallin.

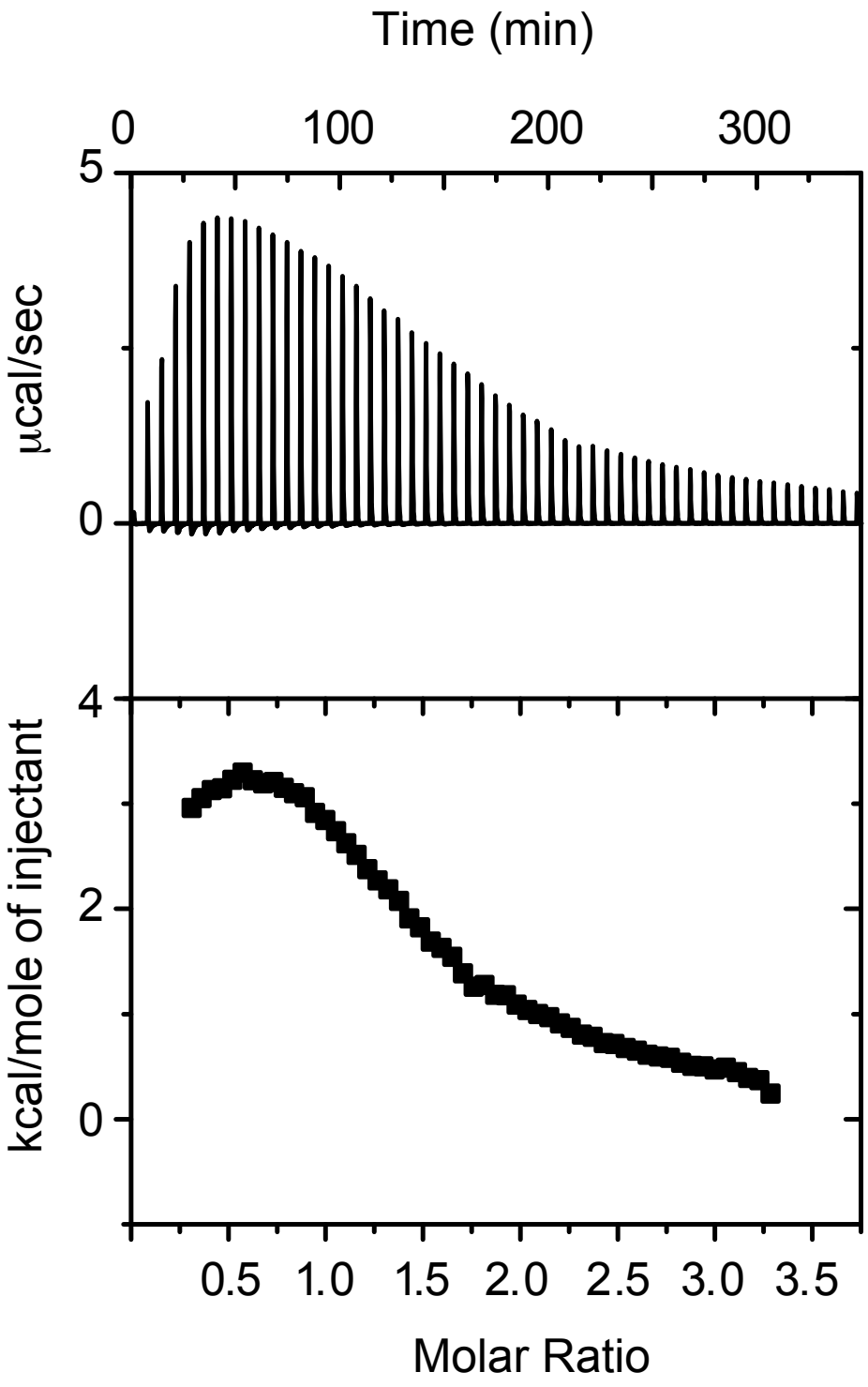

Figure B.1: Isotherm of tunicate crystallin with 10 mM $MgCl_2$.

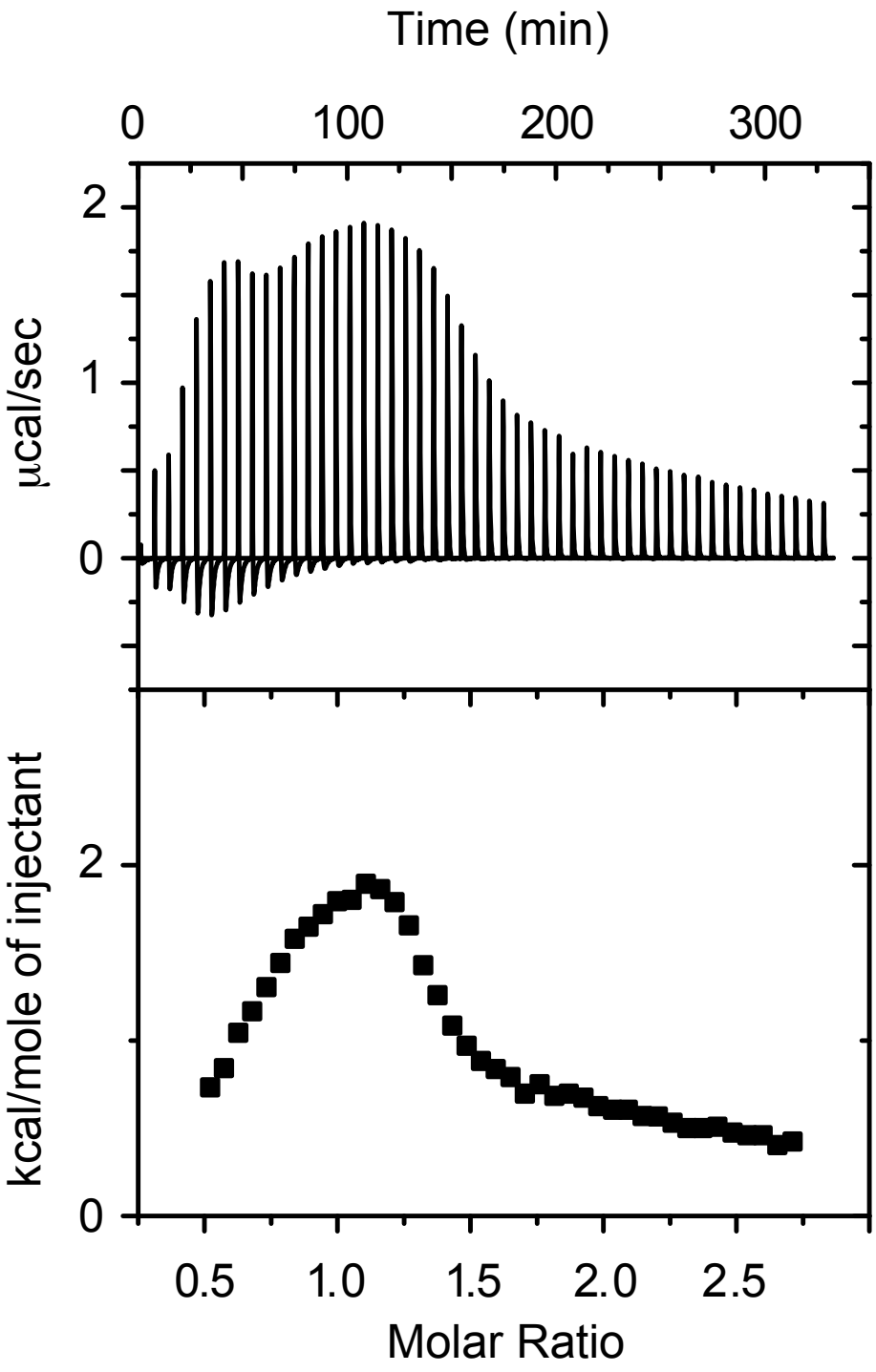

Figure B.2: Isotherm of tunicate crystallin with 10 mM $MnCl_2$.

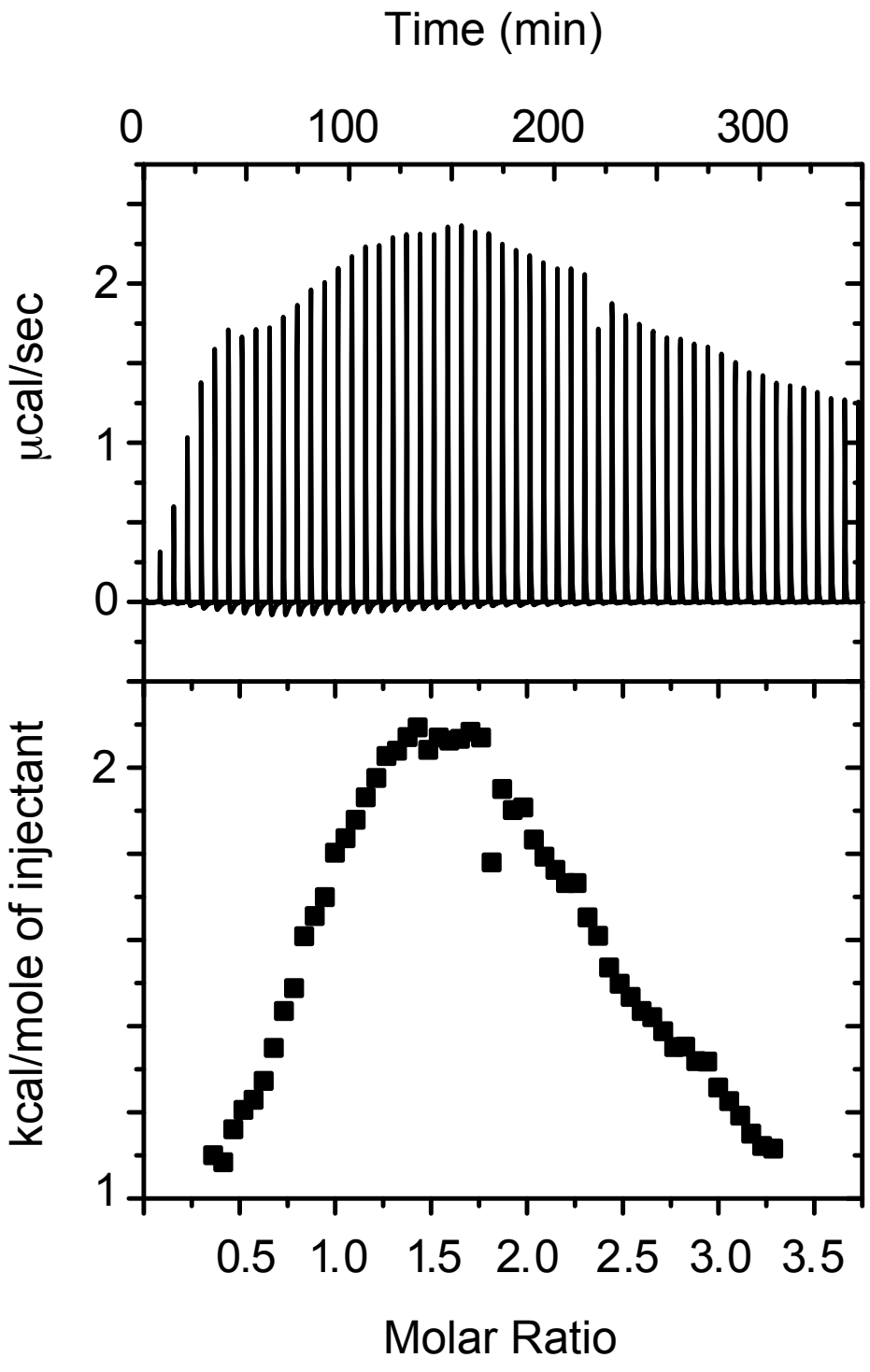

Figure B.3: Isotherm of tunicate crystallin with 10 mM $NiCl_2$.

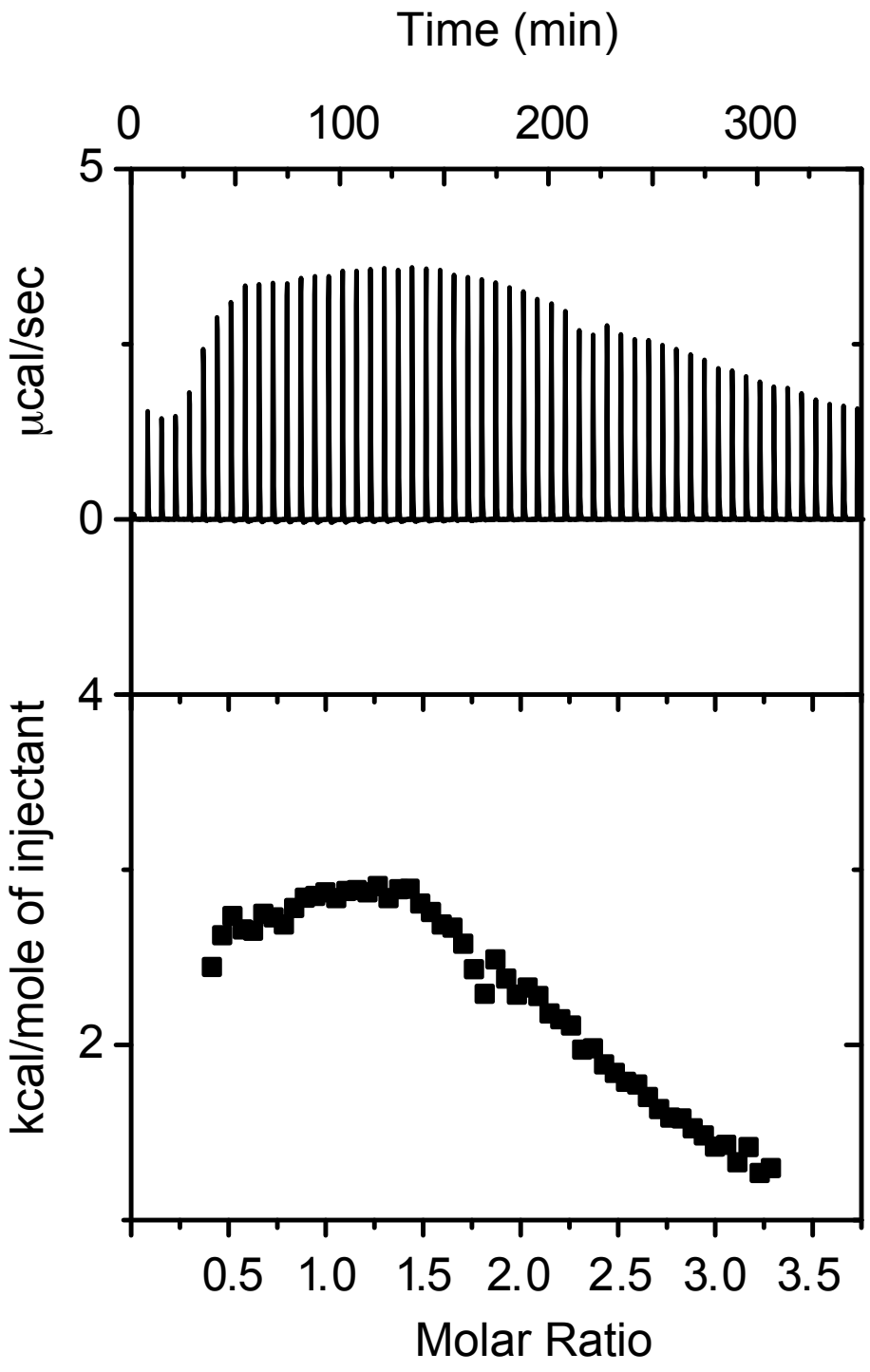

Figure B.4: Isotherm of tunicate crystallin with 10 mM $ZnCl_2$.

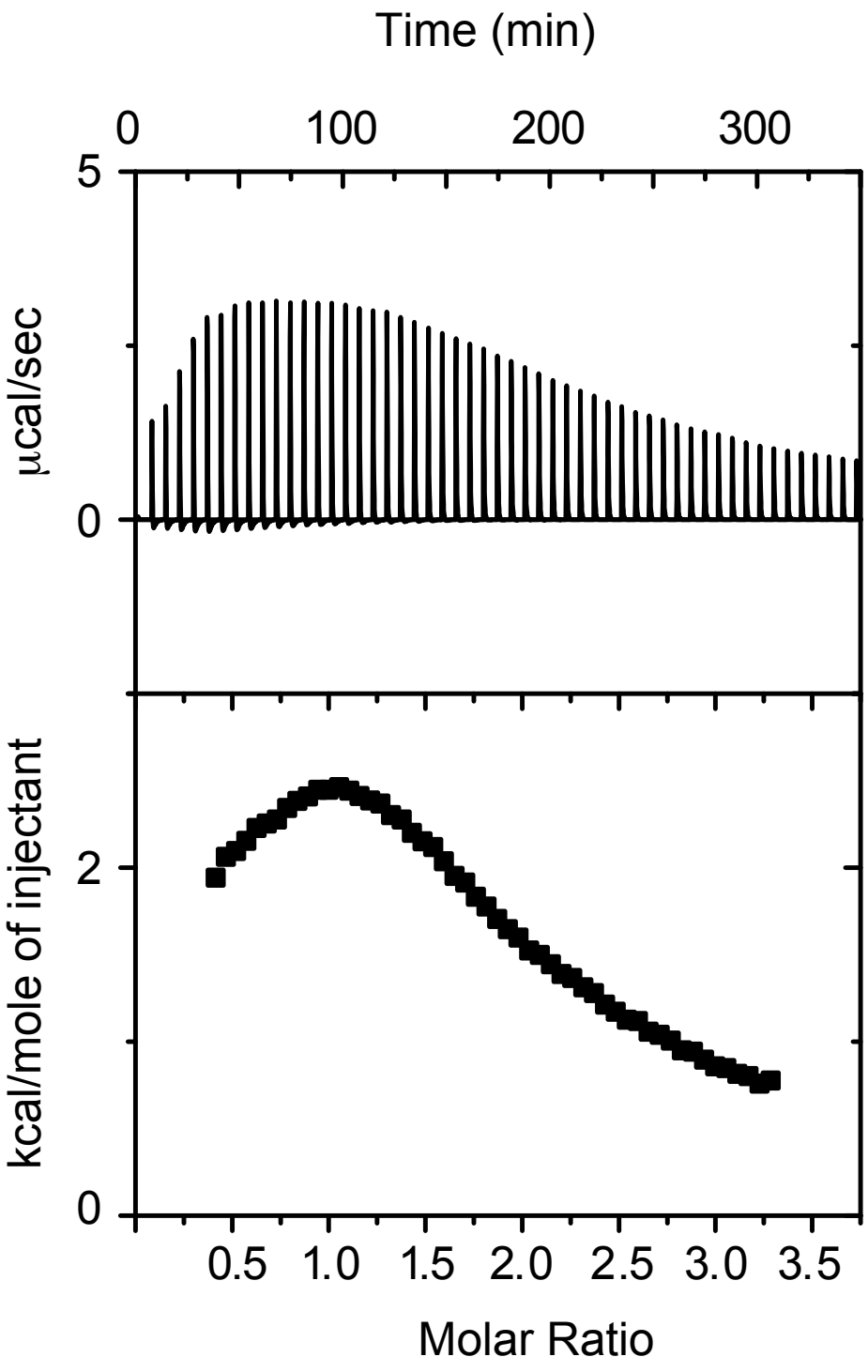

Figure B.5: Isotherm of tunicate crystallin with 10 mM $CoCl_2$.

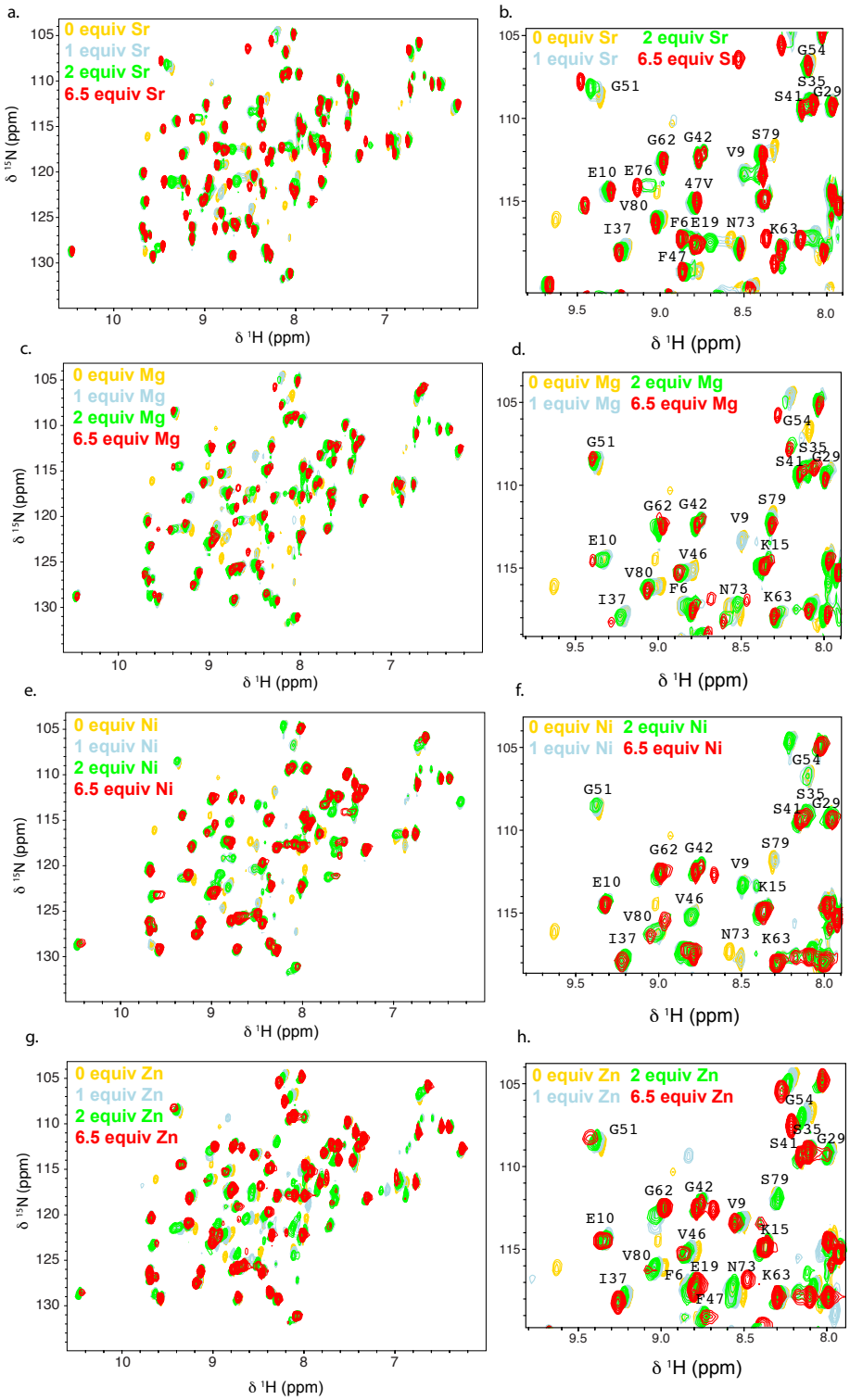

Figure B.6: ^{15}N-^{1}H HSQC spectra of tunicate crystallin with various equivalents of Sr^{2+} (a, b), Mg^{2+} (c, d), Ni^{2+} (e, f), and Zn^{2+} (g, h).

Appendix C

3:Supplementary material for solution-state NMR structure determination of tunicate $\beta\gamma$-crystallin in the apo and holo form.

Table C.1: Amide proton temperature coefficients for tunicate crystallin in the apo and holo form.

Residue	$\Delta\delta/\Delta$T (ppb/K) Apo	$\Delta\delta/\Delta$T (ppb/K) Holo
K2	-2.54 ± 0.21	
I3	-3.20 ± 0.23	-3.03 ± 0.04
I4	-2.30 ± 0.21	-2.31 ± 0.07
L5	-2.20 ± 0.27	-3.06 ± 0.27
F6	-2.30 ± 0.20	-2.59 ± 0.07
E7	-2.60 ± 0.25	-3.84 ± 0.05
D8		-0.69 ± 0.06
V9	-1.02 ± 0.13	-2.68 ± 0.08
E10	-3.96 ± 0.29	-3.72 ± 0.05
F11	-3.96 ± 0.25	-3.6 ± 0.04
G12	-1.96 ± 0.25	-1.78 ± 0.06
G13	-6.16 ± 0.28	-6.15 ± 0.11
K14	-2.84 ± 0.21	-3.43 ± 0.04
K15	-5.18 ± 0.33	-5.21 ± 0.46
L16	-2.23 ± 0.12	-4.12 ± 0.24
E17	-7.07 ± 0.23	-7.23 ± 0.06
L18	-3.86 ± 0.25	-4.11 ± 0.04
E19	-6.02 ± 0.25	-6.05 ± 0.07
T20	-1.40 ± 0.19	-4.24 ± 0.34
S21		-4.07 ± 0.07
V22	-5.10 ± 0.29	-4.44 ± 0.06
S23		-4.36 ± 0.31
D24	-8.56 ± 0.25	-7.82 ± 0.14

L25	-3.80 ± 0.27	
N26	0.50 ± 0.29	1.17 ± 0.04
V27	-1.52 ± 0.20	-1.47 ± 0.05
H28	-1.14 ± 0.18	-1.96 ± 0.07
G29	-1.30 ± 0.25	-1.52 ± 0.05
F30	-0.76 ± 0.21	-1.54 ± 0.05
N31	-5.24 ± 0.32	-7.63 ± 0.34
D32	-0.88 ± 0.36	-0.85 ± 0.04
I33	-7.84 ± 0.61	-2.38 ± 0.06
V34	-4.86 ± 0.37	-3.07 ± 0.05
S35		-1.21 ± 0.05
S36		-2.36 ± 0.17
I37	-3.20 ± 0.22	-3.37 ± 0.05
I38	-3.78 ± 0.29	-3.27 ± 0.04
V39	-2.76 ± 0.20	-2.95 ± 0.05
S41		-2.50 ± 0.20
G42	-5.44 ± 0.21	-5.90 ± 0.08
T43	-5.04 ± 0.13	-3.68 ± 0.32
W44	-3.80 ± 0.27	-3.78 ± 0.11
F45	-2.44 ± 0.25	-2.35 ± 0.06
V46	-2.94 ± 0.27	-2.27 ± 0.06
F47	-2.50 ± 0.24	-3.21 ± 0.05
D48		-4.23 ± 0.05
D49	0.74 ± 0.26	-0.08 ± 0.11
E50	0.14 ± 0.11	0.42 ± 0.07
G51	-5.10 ± 0.25	-4.90 ± 0.04
F52	-3.58 ± 0.23	-3.41 ± 0.05

S53	-0.82 ± 0.21	-7.89 ± 0.05
G54	-6.52 ± 0.16	-6.06 ± 0.21
S56	-4.94 ± 0.21	-4.73 ± 0.09
Y57	-1.98 ± 0.14	
K58	-6.62 ± 0.28	-6.44 ± 0.27
L59	-4.30 ± 0.25	-2.15 ± 0.28
T60	-3.98 ± 0.16	-3.27 ± 0.09
G62	-3.10 ± 0.21	-2.94 ± 0.05
K63	-7.40 ± 0.28	-7.00 ± 0.06
Y64	-3.42 ± 0.25	-3.20 ± 0.05
G68	-4.26 ± 0.23	-4.09 ± 0.07
S69	-4.30 ± 1.08	-4.38 ± 0.42
W70	-2.96 ± 0.22	-2.72 ± 0.06
G71	-2.40 ± 0.20	-2.49 ± 0.06
G72	-1.94 ± 0.10	-2.84 ± 0.05
N73	-7.32 ± 0.31	-6.42 ± 0.08
D74		-9.73 ± 0.17
D75	-0.76 ± 0.11	-1.06 ± 0.05
E76	-7.32 ± 0.53	-4.80 ± 0.06
L77	-3.38 ± 0.17	
S78	-6.02 ± 0.50	-2.79 ± 0.04
S79	-2.10 ± 0.25	-1.68 ± 0.04
V80	-3.60 ± 0.28	-3.50 ± 0.06
K81	-4.30 ± 0.33	-3.46 ± 0.07
Q83	-5.80 ± 0.20	-5.77 ± 0.09

Appendix D

4:Supplementary material for low temperature alignment media for measuring residual dipolar couplings during biomolecular NMR structure determination.

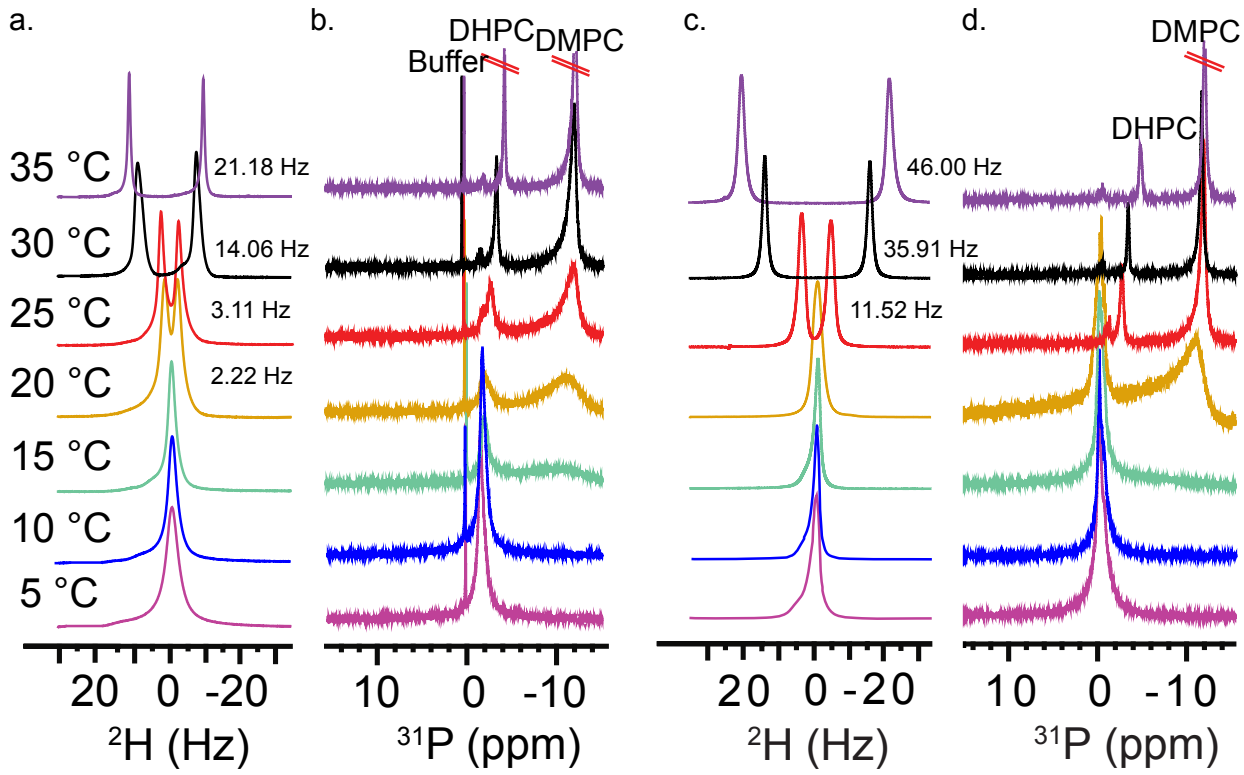

Figure D.1: ^{2}H and ^{31}P NMR spectra of DMPC/DHPC/CS at 5-35 °C in the absence (a, b) and presence (c, d) of 10 mM $MgCl_2$. Addition of $MgCl_2$ improved the overall bicelle alignment with the increase in deuterium splittings. Hash marks represent cut off peaks for space reasons.

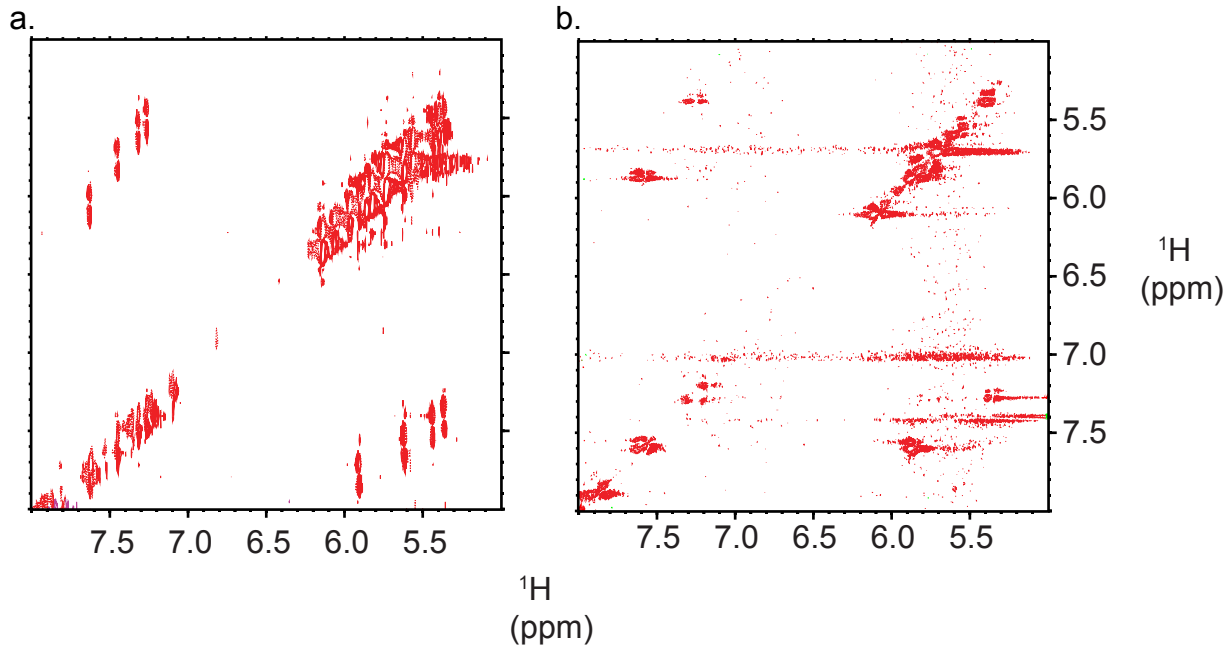

Figure D.2: DQF-COSY regions of four DD cytidines in the absence (a) and presence (b) of DMPC/DHPC/CS at 25 °C.

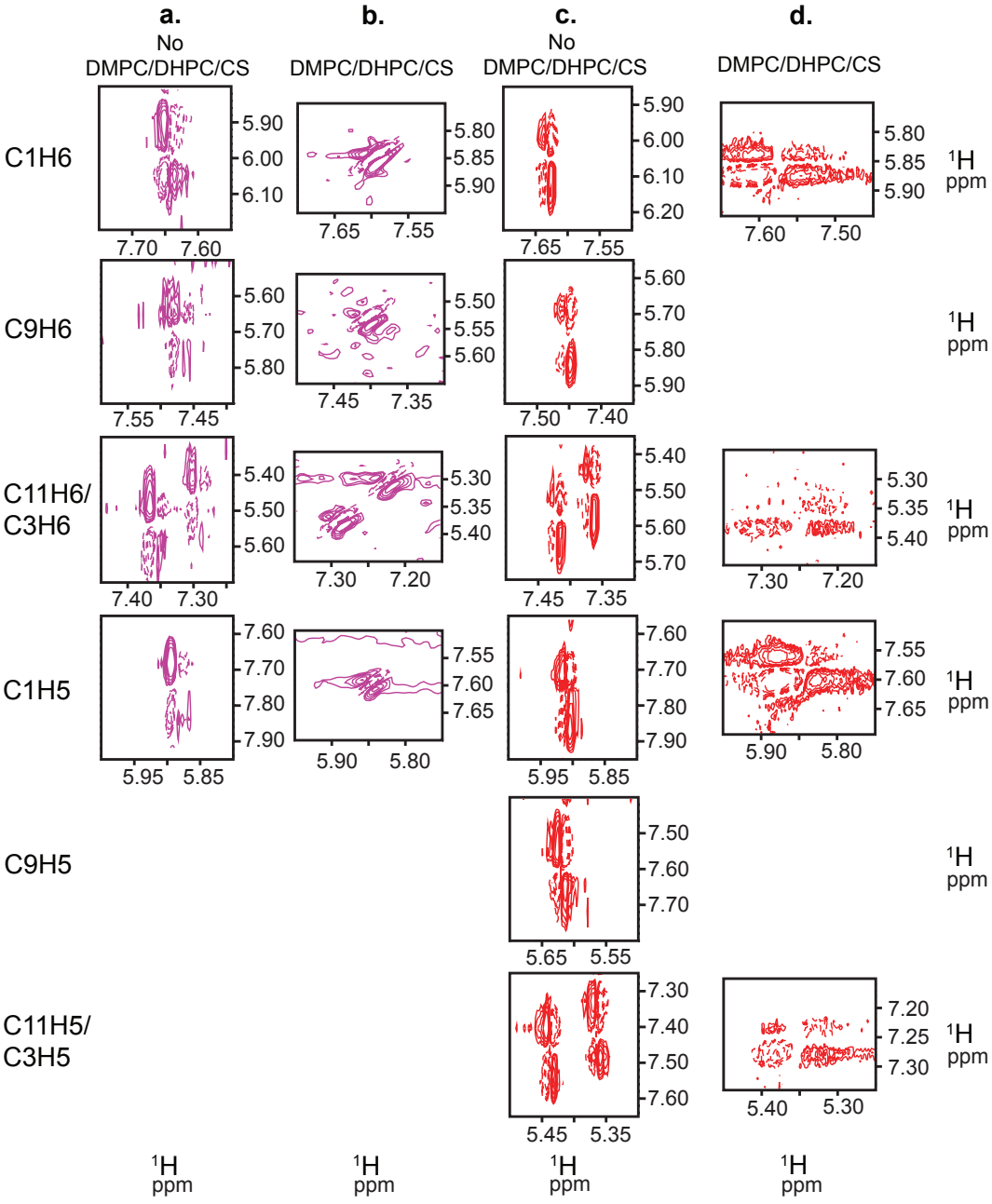

Figure D.3: Small regions of DQF-COSY spectra comparing DD cytidine H5/H6 couplings in the absence (a, c) and presence (b, d) of DMPC/DHPC/CS at 5 °C (magenta) and 25 °C (red). Solid contours represent positive intensities and dashed contours represent negative intensities. Couplings were measured using only the F2 dimension from the top of a positive contour to the top of a negative contour.

Table D.1: H5/H6 cytidine couplings in Hertz in the presence and absence of DMPC/DHPC/CS and in the presence of 10 mM Mg^{2+} at 5 °C and 25 °C. Stronger alignment of DD was observed at 25 °C compared with at 5 °C as shown by the greater change in the cytidine splittings upon addition of the alignment medium to DD. X represents couplings, which were not resolved or were absent from the spectra as a result of negative dipolar couplings.

	DD 5 °C (Hz)	DD + DMPC/DHPC/CS 5 °C (Hz)	DD 25 °C (Hz)	DD + DMPC/DHPC/CS 25 °C (Hz)
C1H6	11.36	19.20	9.36	47.20
C9H6	15.60	17.60	10.00	X
C11H6	12.08	15.20	12.72	X
C3H6	14.88	17.60	10.00	64.00
C1H5	12.96	12.80	8.72	38.40
C9H5	X	X	9.12	X
C11H5	X	X	8.16	X
C3H5	X	X	8.08	51.20

Table D.2: ^2H splitting data of DMPC/DHPC/CS samples with varying divalent cation (Mg^{2+}, Ca^{2+}) and CS concentrations at a temperature range of 5-30 °C. All of the divalent cation samples were prepared from the same batch of stock lipids.

	5 °C (Hz)	10 °C (Hz)	15 °C (Hz)	20 °C (Hz)	25 °C (Hz)	30 °C (Hz)
No cation	X	X	X	X	X	8.94
10 mM Mg^{2+}	X	X	X	X	3.71	15.76
100 mM Mg^{2+}	X	X	X	X	X	16.46
10 mM Ca^{2+}	X	X	X	X	X	13.58
50 mM Ca^{2+}	X	X	X	X	X	11.04
100 mM Ca^{2+}	X	X	X	X	X	9.72
6.7 % CS	X	X	X	X	X	11.37
13.4 % CS	X	X	X	X	6.81	16.21
20.1 % CS	X	X	X	X	4.20	14.08
26.8 % CS	X	X	X	X	5.89	14.01

D.1 Expression and purification of Droserasin 1, plant specific insert

Droserasin 1 (D1) is an antifungal peptide found in the carnivorous plant *Drosera capensis*, which has been hypothesized to inhibit fungal growth via interactions with their lipid membranes. Discovery of novel antifungal agents is important in preventing mycoses such as ringworm and athlete?s foot. Attempts of expression and purification of D1 are described below.

D1 gene: VLSVECKTVVSQYGKTILDMLVAEAQPQKICSQIGLCTFDGERGVSMGIERVVEKED-GRSSGRLHDATCTACEMAVVWIQNQLRQNETEERILNYANQLCERLPSP (3 disulfide bonds!)

D1 gene was first cloned into a Pet28(a)+ vector with a 6x His tag and NCO1 and XHO1 restriction cut sites on both sides. Expression of D1 with His tag did not work with Studier auto induction method but worked with induction with IPTG (25 °C for 24 h). The protein was soluble and did not go into the inclusion bodies. Affinity chromatography seemed to purify the protein well (buffers used were 50 mM phosphate, 10 mM imidazole (pH 7) for wash and 50 mM phosphate, 500 mM imidazole (pH 7) for elution). Addition of TEV protease to remove the His tag was not successful even after 72 h (there was about 25 % . Various conditions were tried to improve the catalytic reaction of TEV such as the addition of 1.5 M urea, 50 mM Tris buffer (pH 8) and 50 mM NaCl, addition of more TEV (2 mg of TEV for 100 mg of protein), addition of 3 mM GSH/0.3 mM GSSG and using SEC chromatography following affinity chromatography prior to addition of TEV in order to separate the monomers from the multimers. None of these conditions seemed to help. SDS page gel pictures for these purifications can be found in notebook 2 for Kozlyuk.

In case TEV protease cut site was not accessible to the enzyme due to the interaction of the His tag with the protein, a longer linker was designed (His tag fused with a thioredoxin

solubility tag fused with a linker then a TEV cut site then D1 construct). This construct was transformed into a Shuffle cell line which is better for expression of proteins with disulfide bonds. Same expression and purification protocols were used as in the absence of thioredoxin. With the thioredoxin protein, expression was also achieved with the Studier auto induction protocol. The same problem was encounter with the thioredoxin protein where TEV was not fully cleaving the His + thioredoxin tag. Mass spec showed that D1 was expressed but other impurities were present as well as the full thio + D1 construct.

Expression and purification of D1 was repeated with His tag but without the thioredoxin in Shuffle cells. Incomplete cleavage was achieved once again.

The His tag was removed from the D1 construct and expression and purification of D1 was attempted in the Shuffle cells. Auto induction was working for the expression of D1. After a lot of trial and error, the pI of D1 was found around 10.5. With that, the best method for purifying D1 was running a pH gradient anion exchange column using 10 mM imidazole pH 7 and 10 mM Hepes pH 10.5 buffers. D1 came out at the end of the run. Running SEC afterward the anion exchange purification showed that D1 was sticking to three other proteins which were identified with mass spec to be maltose transporter subunit, arginine ABC transporter substrate-binding protein, and Dsba.

DO NOT ADD DTT BECAUSE PROTEIN WILL CRASH OUT.

Appendix E

5:Supplementary material for *In Situ* NMR Measurement of Macromolecule-Bound Metal Ion Concentrations.

Table E.1: Titration curve values of dCDP with Mg^{2+} pH 6.05 25°C.

Concentration (mM)	α-phosphate chemical shift (ppm)
0.01	10.42
0.07	10.30
0.18	10.19
0.39	10.03
0.85	9.91
1.8	9.72
2.8	9.63
4.8	9.57
9.7	9.48
29.7	9.41
49.7	9.38

Table E.2: Titration curve values of dCDP with Mg^{2+} pH 6.25 8°C.

Concentration (mM)	α-phosphate chemical shift (ppm)
0.01	10.38
0.09	10.34
0.19	10.21
0.41	10.13
0.85	9.94
1.8	9.77
2.8	9.67
4.7	9.64
9.7	9.55
29.7	9.55
49.7	9.50

Table E.3: Titration curve values of dCDP with Mg^{2+} pH 7.05 25°C.

Concentration (mM)	α-phosphate chemical shift (ppm)
0.01	10.38
0.06	10.23
0.17	10.10
0.36	9.90
0.82	9.74
1.7	9.48
2.7	9.43
4.7	9.32
9.7	9.28
29.7	9.32
49.7	9.29

Table E.4: Titration curve values of dCDP with Mg^{2+} pH 7.25 8°C.

Concentration (mM)	α-phosphate chemical shift (ppm)
0.01	10.28
0.07	10.18
0.21	10.13
0.42	9.98
0.85	9.73
1.8	9.61
2.8	9.56
4.8	9.50
9.8	9.47
29.8	9.49
49.8	9.49

Table E.5: Titration curve values of dCDP with Mg^{2+} pH 8.05 25°C.

Concentration (mM)	α-phosphate chemical shift (ppm)
0.01	10.02
0.06	9.93
0.15	9.78
0.34	9.64
0.77	9.47
1.7	9.33
2.7	9.28
4.7	9.24
9.7	9.26
29.7	9.26
49.7	9.29

Table E.6: Titration curve values of dCDP with Mg^{2+} pH 8.25 8°C.

Concentration (mM)	α-phosphate chemical shift (ppm)
0.01	10.28
0.07	10.21
0.15	10.02
0.31	9.78
0.75	9.62
1.7	9.51
2.7	9.44
4.7	9.43
9.7	9.42
29.7	9.43
49.7	9.48

Table E.7: Titration curve values of 0.6 mM dCDP with Mg^{2+} pH 7.05 25°C.

Concentration (mM)	α-phosphate chemical shift (ppm)
0.01	10.35
0.03	10.22
0.15	10.18
0.26	9.94
0.64	9.71
1.5	9.50
2.5	9.41
4.4	9.33
9.4	9.31
29.4	9.27
49.7	9.30

Table E.8: Titration curve values of dCDP with Ca^{2+} pH 6.05 25°C.

Concentration (mM)	α-phosphate chemical shift (ppm)
0.01	10.45
0.07	10.35
0.20	10.29
0.45	10.28
0.92	10.19
1.9	10.10
2.9	10.00
4.8	9.91
9.8	9.71
29.7	9.53
49.7	9.43

Table E.9: Titration curve values of dCDP with Ca^{2+} pH 6.25 8°C.

Concentration (mM)	α-phosphate chemical shift (ppm)
0.01	10.42
0.09	10.39
0.23	10.37
0.46	10.29
0.98	10.23
1.9	10.08
2.9	9.99
4.8	9.88
9.8	9.74
29.7	9.56
49.7	9.48

Table E.10: Titration curve values of dCDP with Ca^{2+} pH 7.05 25°C.

Concentration (mM)	α-phosphate chemical shift (ppm)
0.01	10.25
0.08	10.18
0.18	9.99
0.40	9.87
0.84	9.67
1.8	9.47
2.8	9.42
4.7	9.33
9.7	9.29
29.7	9.18
49.7	9.17

Table E.11: Titration curve values of dCDP with Ca^{2+} pH 7.25 8°C.

Concentration (mM)	α-phosphate chemical shift (ppm)
0.01	10.27
0.10	10.25
0.21	10.13
0.43	10.04
0.87	9.88
1.8	9.69
2.8	9.60
4.7	9.53
9.7	9.46
29.7	9.37
49.7	9.35

Table E.12: Titration curve values of dCDP with Ca^{2+} pH 8.05 25°C.

Concentration (mM)	α-phosphate chemical shift (ppm)
0.01	10.10
0.05	9.91
0.21	9.93
0.41	9.78
0.86	9.61
1.8	9.44
2.8	9.38
4.8	9.33
9.8	9.24
29.7	9.21
49.7	9.07

Table E.13: Titration curve values of dCDP with Ca^{2+} pH 8.25 8°C.

Concentration (mM)	α-phosphate chemical shift (ppm)
0.01	10.29
0.08	10.23
0.19	10.09
0.38	9.91
0.83	9.73
1.8	9.55
2.8	9.48
4.7	9.41
9.7	9.37
29.7	9.30
49.7	9.31

Table E.14: Interaction of the dCDP α-phosphate with $[Ca^{2+}_{Free}]$.

pH/Temp (°C)	δ_∞*(ppm)	$K_{1/2}$*(mM)	n*
6.05/25.0	9.13±0.03	4.08±0.54	0.67±0.07
6.25/8.0	9.37±0.03	3.62±0.48	0.87±0.10
7.05/25.0	9.16±0.03	0.70±0.09	0.89±0.10
7.25/8.0	9.34±0.03	1.12±0.15	1.02±0.11
8.05/25.0	9.10±0.03	1.04±0.14	0.90±0.10
8.25/8.0	9.30±0.03	0.58±0.08	1.03±0.12

*^{31}P δ_∞, midpoint ($K^{1/2}$) and polynomial exponent (n) values with their relative uncertainties at different pH and temperature values.

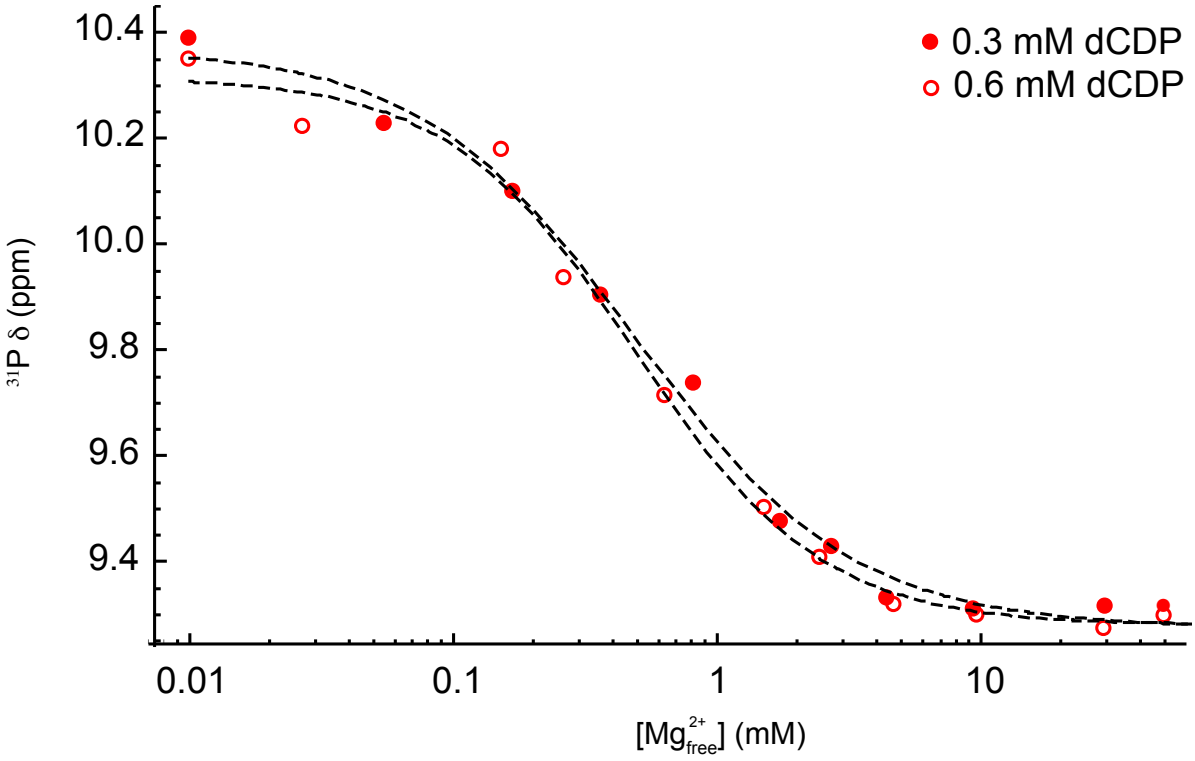

Figure E.1: Titration curves of the α-phosphate ^{31}P chemical shift as a function of increasing [Mg^{2+}] (0.01-10 mM) at pH 7.05 and 25 °C containing 0.6 mM dCDP versus 0.3 mM dCDP.

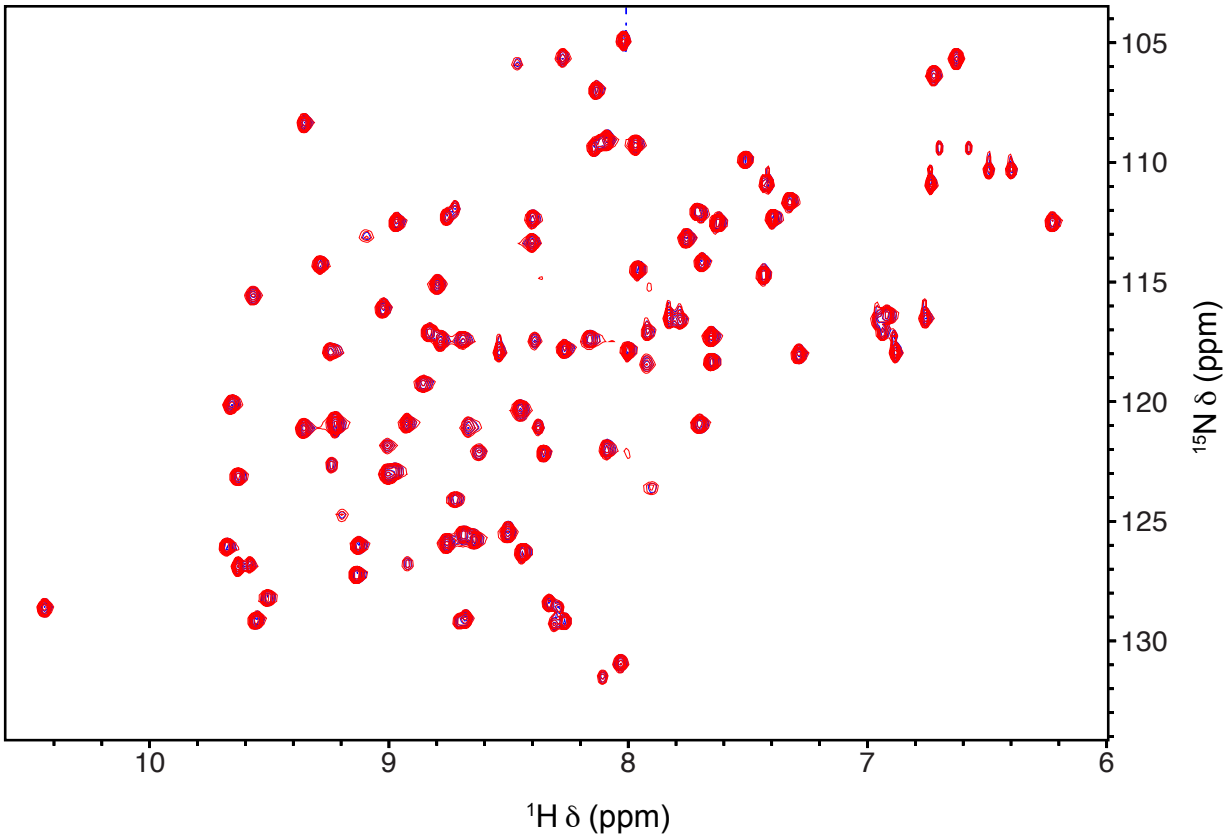

Figure E.2: Overlay of ^{15}N-^{1}H HSQC of tunicate $\beta\gamma$-crystallin protein with 7 mM Ca^{2+} in the presence (red) and absence (purple) of 0.6 mM dCDP at 25 °C showing the absence of interaction between the protein and the small molecular probe.

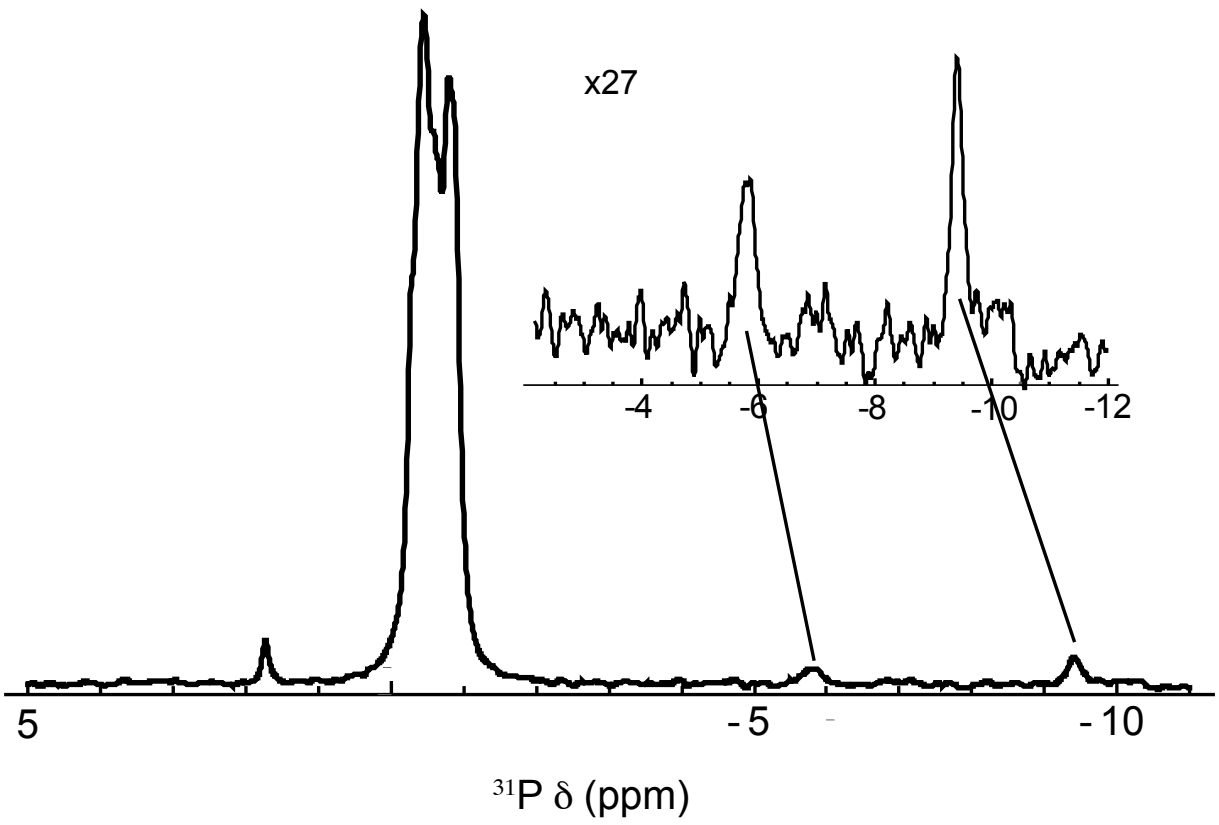

Figure E.3: DNA ^{31}P spectrum in the presence of dCDP and 6 mM Mg^{2+} at 25 °C.

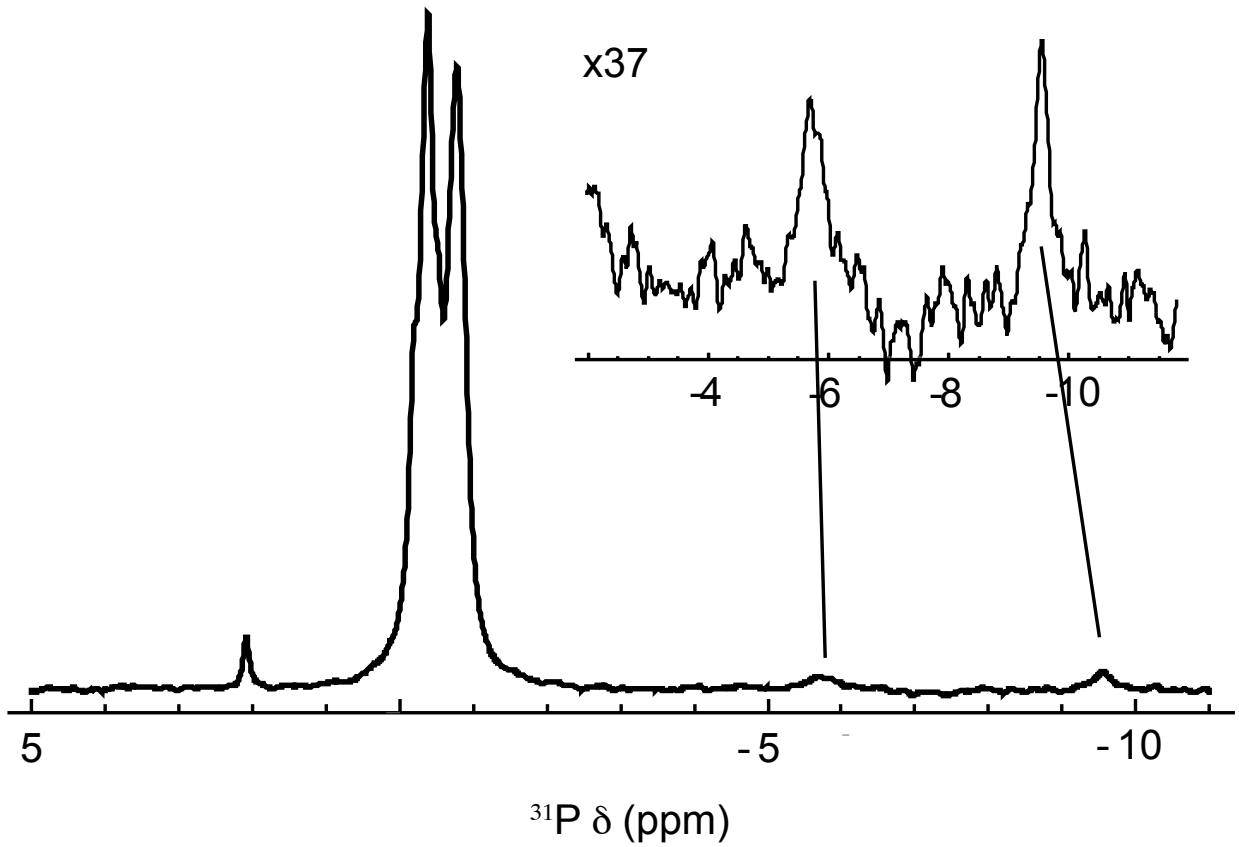

Figure E.4: DNA ^{31}P spectrum in the presence of dCDP and 6 mM Mg^{2+} at 8 °C.

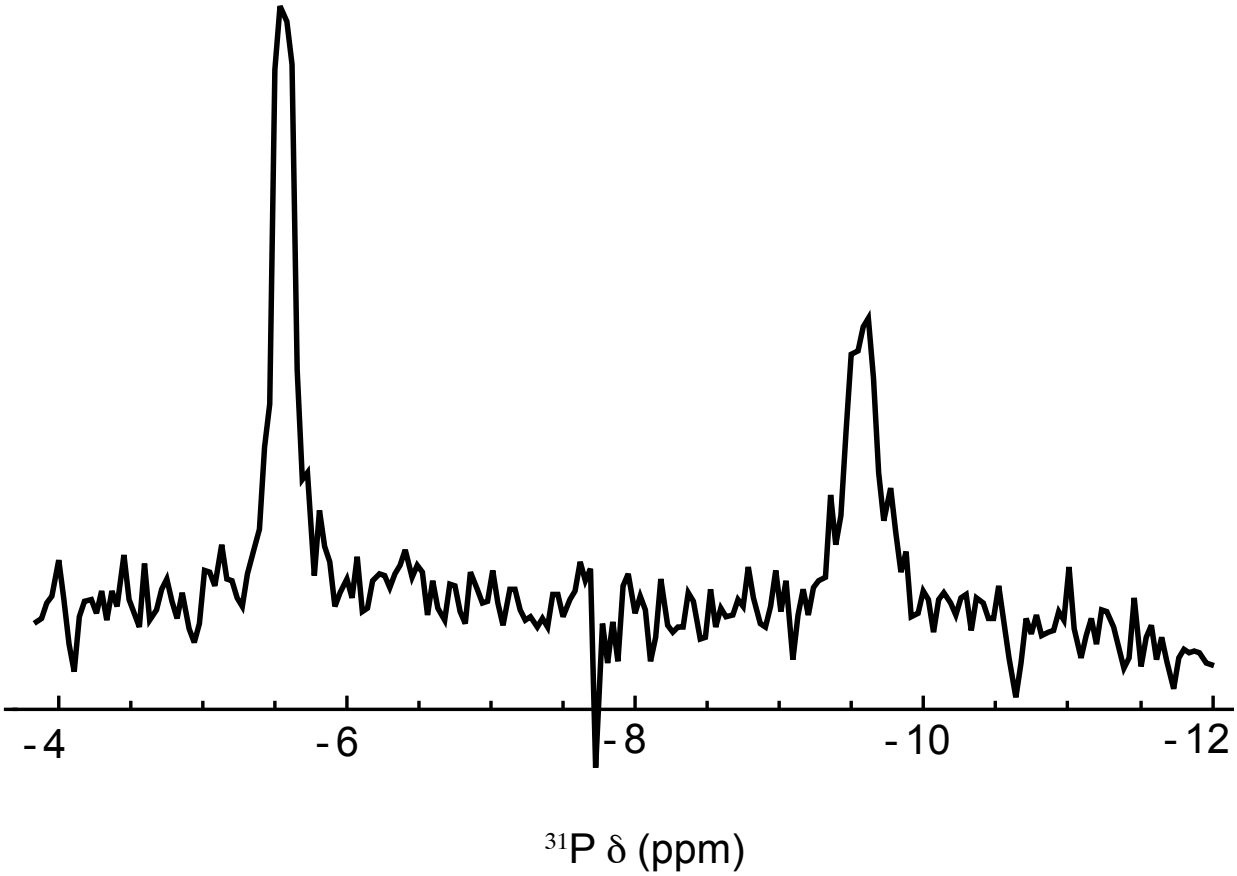

Figure E.5: Bicelles ^{31}P spectrum in the presence of dCDP and 10 mM Mg^{2+} at 8 °C.

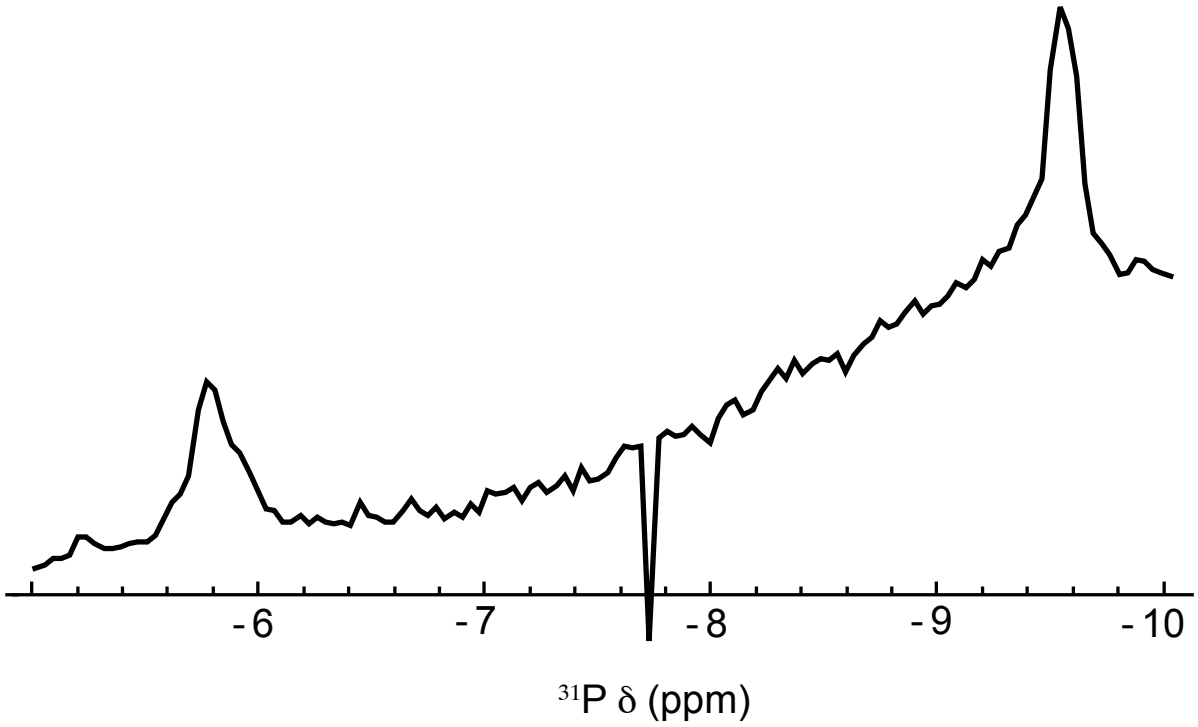

Figure E.6: Bicelles ^{31}P spectrum in the presence of dCDP and 10 mM Ca^{2+} at 8 °C.